

國立交通大學

電子物理學系

博士論文

以時間解析飛秒光譜研究六方晶系結構
欽錳氧單晶之載子動力學



Study of the Carrier Dynamics in Hexagonal
HoMnO₃ Single Crystals Using Time-Resolved
Femtosecond Spectroscopy

研究生：石訓全

指導教授：吳光雄 教授
羅志偉 教授

中華民國九十九年七月

以時間解析飛秒光譜研究六方晶系結構欽錳氧
單晶之載子動力學

Study of the Carrier Dynamics in Hexagonal HoMnO₃ Single
Crystals Using Time-Resolved Femtosecond Spectroscopy

研 究 生：石訓全

Student：Hsun-Chuan Shih

指導教授：吳光雄 教授
羅志偉 教授

Advisor：Prof. Kaung-Hsiung Wu
Advisor：Prof. Chih-Wei Luo



A Dissertation
Submitted to Department of Electrophysics
College of Science
National Chiao Tung University
in Partial Fulfillment of the Requirements
for the Degree of
Doctor of Philosophy
in
Electrophysics
July 2010
Hsinchu, Taiwan

中華民國九十九年七月

以時間解析飛秒光譜研究六方晶系結構欽錳氧 單晶之載子動力學

研究生：石訓全

指導教授：吳光雄 教授
羅志偉 教授

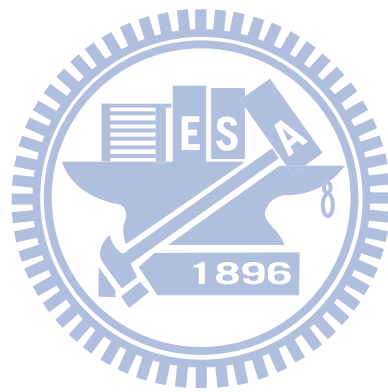
國立交通大學 電子物理學系

中文摘要

在本論文中，我們利用具有時間解析的激發探測實驗去研究多鐵性六方晶系欽錳氧單晶的超快載子動力學。首先，我們量測六方晶系欽錳氧單晶的基本特性，例如用 X 光 θ - 2θ 繞射確認晶體結構及用超導量子干涉儀進一步確定磁矩隨溫度的排列情形。在此材料系統中，所謂”多鐵”是指具有電性(鐵電)與磁性(反鐵磁)以及彈性等多個有序特性的共存，且在該材料中磁電、磁彈間存在著強的耦合(Coupling)作用，即施加電場可影響磁性，反之加磁場又可影響其電的特性。這些有序參數間的交互作用引發許多的有趣現象，近年來引發科學家的研究熱潮。

從激發探測實驗結果中，透過波長可調的飛秒光譜實驗在欽錳氧單晶中觀察到反鐵磁有序與電子結構會有強烈的耦合情形，該材料中存在的磁長程有序會造成錳離子 $3d$ 軌域在尼爾溫度有異常的藍移現象，同時在尼爾溫度之上因短程有序的出現造成反射率變化($\Delta R/R$)的振幅對溫度變化之斜率有顯著的改變。接著，我們在欽錳氧單晶中透過激發光所造成的光致熱

彈效應(thermoelastic effect)在尼爾溫度觀察到異向性的磁彈耦合行為，進而揭示了電性、彈性與磁性不同自由度間的耦合情形。其中光致熱彈效應在 ab 平面上造成反射率變化被我們定義的”負”分量所主宰，而沿著 c 方向傳遞的應力形變波則造成反射率變化中的”振盪”分量，兩個分量皆在尼爾溫度出現異常的變化。最後，從反射率變化中的振盪分量隨溫度的變化，我們認為週期的變化來自於鐵電的極化率隨溫度的改變。



Study of the Carrier Dynamics in Hexagonal HoMnO₃ Single Crystals Using Time-Resolved Femtosecond Spectroscopy

Student : Hsun-Chuan Shih

Advisor : Prof. Kaung-Hsiung Wu
Prof. Chih-Wei Luo

Department of Electrophysics
National Chiao Tung University

Abstract

In this dissertation, we study the characteristics of ultrafast carrier dynamics in hexagonal HoMnO₃ single crystals via time-resolved pump-probe experiments. First of all, we measured the fundamental properties of hexagonal HoMnO₃, such as crystal structure by the X-ray diffraction (XRD) θ - 2θ pattern, the arrangement of magnetic moment by the superconducting quantum interference device (SQUID). Multiferroic materials with coexistence of several ferroic orders (ferroelectric, ferromagnetic, or ferroelastic) have attracted great attention of scientists recently. The magnetoelectric response is the appearance of an electric polarization upon applying a magnetic field and/or the appearance of a magnetization upon applying an electric field.

In pump-probe results, we demonstrate that the strong coupling between the electronic structure and antiferromagnetic (AFM) ordering in hexagonal HoMnO₃ single crystals can be simultaneously delineated by wavelength-dependent femtosecond spectroscopy. The emergence of long-range and short-range magnetic ordering are unambiguously revealed in association

with an abnormal blue-shift of Mn^{3+} $3d$ level around the Néel temperature and the slope change of the temperature-dependent $\Delta R/R$ near transition, respectively. Furthermore, the coupling among the magnetization, polarization, and strain degree of freedoms has been simultaneously disclosed in the hexagonal HoMnO_3 single crystals through the photo-induced anisotropic ultrafast thermoelastic dynamics. The thermoelastic effect in the ab -plane associated with the giant magnetoelastic coupling around the Néel temperature (T_N) is intimately correlated to the evolvement of a negative component in the transient reflectivity changes ($\Delta R/R$) obtained from temperature-dependent pump-probe experiments. Moreover, the variation of the period of the oscillation component in $\Delta R/R$ caused by a strain pulse propagating along c -axis exhibits an abrupt drop around T_N , presumably due to the antiferromagnetic ordering-induced ferroelectricity.



Acknowledgments

回想起四年多前，決定參與研究中心實驗室的成立與建置，現在回頭想想這還真是個正確的決定，因為這個經驗讓我學到太多的東西了。這條漫長研究的道路上有責任有壓力，有成就有收穫，其中的難過與開心則是點滴在心頭。最後用”值得”來替自己的博士生涯做最佳的註解，這也會是一段最讓我難忘的人生旅程。

博士四年的經歷與些許的成就建立在辛勤的耕耘，但是過程中因為有太多人的協助與關心才有這一點點成績讓我以後可以驕傲的拿出來說嘴。有很多感謝的話，首先，我的指導老師與共同指導老師：吳光雄教授與羅志偉教授，謝謝你們對我的信任與對我的包容，在三更半夜還陪我討論實驗與論文，對於研究的態度與堅持著研究的熱忱更是讓我大開眼界；固態實驗室的老師群：溫增明教授、莊振益教授、林俊源教授、郭義雄教授，雖然每次 Meeting 都遭受無情的炮火襲擊，但不可諱言這是讓我成長最直接的方法，並且讓我釐清我的思緒與方向，特別是能得到溫老師的些許肯定更讓我備感榮幸；莊院長謝謝你常常在百忙之中幫我修改論文，讓我的論文更加完備；超快研究中心的小林孝嘉教授、藪下篤史教授，沒有你們提供如此完善的研究設備難以成就這本論文。

再來就是感謝實驗室的夥伴了！謝志昌學長與宗漢，要不是有你們在我低潮遭遇困難的時候拉我一把，給我協助與幫忙，我想今天也就不會在這邊寫誌謝了。另外要感謝信斌、龍羿、育賢，實驗室建立之初就是我們胼手胝足，一起努力才有現在實驗室的規模。還有這個大家庭裡許許多多的學弟妹：新安、以恆、純芝、享穎、昱庭、宣懿、維聰、劭軒、潤東、裕廉、志翔、佳璟、易修、韋臻、志賢、文彥等，平常陪我吵吵鬧鬧、裝瘋賣傻、互相幫忙，好不開心！除此之外，也有許多曾經在我博士生涯中出現的好朋友對我的鼓勵與支持更是我完成博士學位的最大動力，令人難忘。

當然拿到博士學位，最感謝的是我的父母與哥哥，沒有你們全力的支持與栽培，沒有今天的我，家裡大大小小的事情都不需要我來分擔，讓我無後顧之憂完成我的學位。

現在要離開實驗室了，心情自然是百感交集。如今的我帶著滿滿的成就與回憶，就像當初空蕩蕩的實驗室現在則是填滿了許許多多的儀器，希望帶著一身練就的武功到外面的世界闖一闖，能讓實驗室以我為榮！



Table of Contents

Abstract (in Chinese)	i
Abstract (in English)	iii
Acknowledgements	v
Table of Contents	vii
Chapter 1 Introduction	1
1.1 Survey the researches of hexagonal $ReMnO_3$ materials	7
1.2 Motivation	12
1.3 The organization of this dissertation	14
Chapter 2 Experimental tools and procedures	19
2.1 Characterization and preparation of h - $HoMnO$ single crystals	19
2.1.1 Orientation and structure of $HoMnO_3$ single crystals	20
2.1.2 Temperature-dependent susceptibility measurements	22
2.1.3 Transmittance spectrum	24
2.2 Femtosecond time-resolved systems	26
2.2.1 The polarized femtosecond pump-probe system	27
2.2.2 The terahertz time-domain spectroscopy	29
2.2.3 The optical pump terahertz probe system setup	32
Chapter 3 The femtosecond pump-probe spectroscopy	39
3.1 The characteristics of femtosecond pulse laser	39
3.1.1 The light pulses	40
3.1.2 Method for the generation of ultrafast laser pulses	42

3.1.3	Measurement of the pulse temporal profile	44
3.2	The fundamental principle of pump-probe experiments	47
3.3	The coherent spike in reflection-type pump-probe	49
Chapter 4	The ultrafast dynamics on <i>h</i>-HMO single crystals	56
4.1	The results of $\Delta R/R$ at various wavelengths and temperatures	57
4.1.1	The transient reflectivity changes $\Delta R/R$	57
4.1.2	Classify the ultrafast behaviors in $\Delta R/R$ curves	60
4.1.3	The mathematical fittings in $\Delta R/R$ curves	62
4.2	The temperature-dependent amplitude of $\Delta R/R$	65
4.2.1	The amplitude of $\Delta R/R$ between 20-300 K	65
4.2.2	The amplitude of $\Delta R/R$ in high temperature range	70
4.3	The anisotropic magnetoelastic coupling in <i>h</i> -HMO	72
4.3.1	Laser-induced thermoelastic generation	72
4.3.2	Laser-induced lattice dynamics on <i>a-b</i> plane	74
4.3.3	Laser-induced strain pulse propagation along <i>c</i> -axis	81
Chapter 5	Summary	92
	Biographical Notes	95

Chapter 1

Introduction

Multiferroic materials [1-5] with coexistence of various ferroic orders (ferromagnetic, ferroelectric, or ferroelastic) have attracted great attention in condensed-matter researches due to their great potential for applications in the field of oxide electronics, spintronics, and even the green energy devices for reducing the power consumption. In multiferroic oxides (in single phase), the coupling interaction among various order parameters causes the magnetoelectric (ME) effect [6-11]. Namely, a polarization (magnetization) can be induced by application of a magnetic (electric) field. Although the properties of electricity and magnetism were combined into one common discipline by Maxwell equations in the 19th century, the electric and magnetic orderings in solid-state materials is always considered separately. This is because that the electric charges of electrons and ions are responsible for the charge effects, whereas the electron spins govern the magnetic properties.

The presaging of a strong coupling between magnetic and electric degrees of freedom in one substance can be traced back to very long time ago which was provided by Pierre Curie (the latter stage of the 19th century [12]), but the actual beginning of this field started in 1959

with a short comment in Landau and Lifshitz's course of theoretical physics [13]:

“Let us point out two more phenomena, which, in principle, could exist. One is piezomagnetism, which consists of linear coupling between a magnetic field in a solid and a deformation (analogous to piezoelectricity). The other is a linear coupling between magnetic and electric fields in a media, which would cause, for example, a magnetization proportional to electric field. Both these phenomena could exist for certain classes of magnetocrystalline symmetry. We will not however discuss these phenomena in more detail because it seems that till present, presumably, they have not been observed in any substance.”

Thereafter, this short remark about the linear magnetoelectric coupling effect was changed soon due to the prediction of Dzyaloshinskii [14] and the observation of Astrov [15]. Dzyaloshinskii, a condensed-matter physicist in Russia, predicted that the Cr_2O_3 crystals satisfy the conditions of magnetoelectric effect in 1959. In next year 1960, Astrov successfully observed the magnetoelectric effect in the Cr_2O_3 single crystals. From that time, the magnetoelectric materials attracted great attention and caused strong studies. During several years, then, many kinds of magnetoelectric materials had been discovered, such as Ti_2O_3 [16], $\text{Ni}_3\text{B}_7\text{O}_{13}$ [17], BiFeO_3 [18], GaFeO_3 [19], $\text{Y}_3\text{Fe}_5\text{O}_{12}$ [20], and etc.. Unfortunately, these upsurged studies declined gradually due to that the magnetoelectric coupling coefficient is too small to the applications which were highly praised by scientists at that time.

Until 2000, the studies of the perovskite-based multiferroic materials, such as rare-earth manganates TbMn_2O_5 , YMnO_3 , BiMnO_3 , etc., renewed the scientists' attention and began all over again. There are two main reasons: the first one is the breakthrough of the theoretical works which are due to the combination between the developments of density functional

theory and the technology of computer [21]. On the other hand, it is due to the improvement in thin film deposition. Thus, the artificial thin films can be produced to match the requirements of theoretical works.

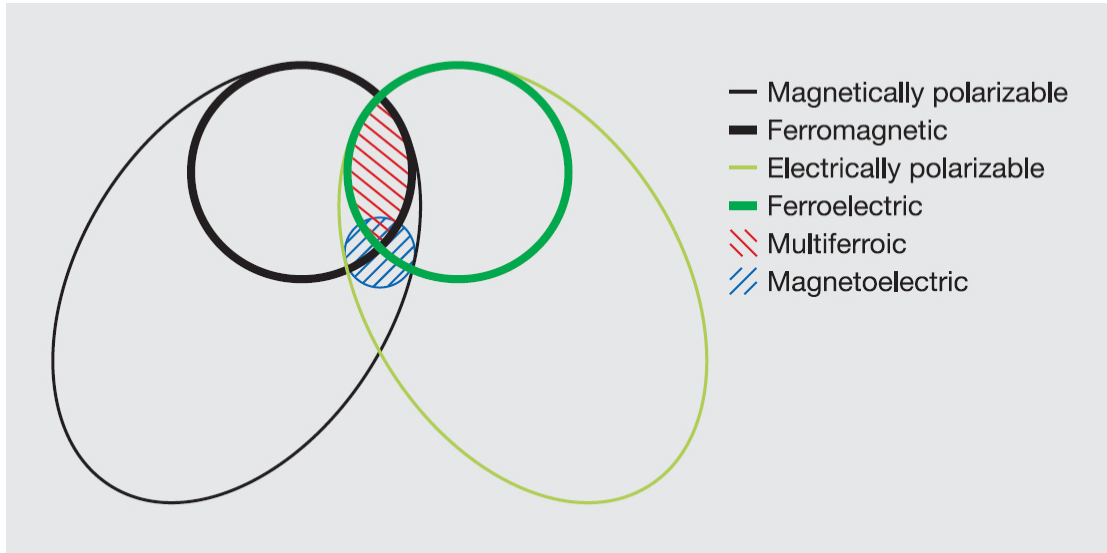


Figure 1-1: *The relationship between multiferroic and magnetoelectric materials [5].*

Figure 1-1 shows the relationship between multiferroic and magnetoelectric which tells us the fact that there are few materials belongs to multiferroic materials. Although it is not easy to find new multiferroic materials, there are still a lot of multiferroic materials that had been discovered and investigated recently. In order to understand the physical mechanism of multiferroic materials, W. Priller *et al.* [22] classified the characteristics of multiferroic materials into three categories. The first one is Bi-based compounds, such as BiMnO_3 , BiFeO_3 , and PbVO_3 , etc.. The second one is other perovskites and related materials: ReMnO_3 compounds ($\text{Re} = \text{Y, Ho, Er, Tm, Yb, and Lu}$). The third one is ReMn_2O_5 ($\text{Re} = \text{rare-earth}$). The aim of his paper is to introduce the current materials which are under study. Additionally, S.-W. Cheong *et al.* [23] further summarized the classification of “proper” and “improper” ferroelectrics shown in Table 1.1 by the mechanism of ferroelectricity. In the category of the

proper ferroelectrics, the main driving force toward the polar state was associated with the electronic pairing. In contrast, the induced polarization of ferroelectricity involves a more complex lattice distortion or other accidental by-product of some other ordering is called “improper” [24], such as the hexagonal manganites $ReMnO_3$ which show a lattice distortion to enlarge their unit cell (geometric ferroelectricity) [25-27]. Moreover, another group of improper ferroelectrics are those induced by magnetic ordering.

	Mechanism of inversion symmetry breaking	Materials
Proper	Covalent bonding between $3d^0$ transition metal (Ti) and oxygen	$BaTiO_3$
	Polarization of $6s^2$ lone pair of Bi or Pb	$BiMnO_3$, $BiFeO_3$, $Pb(Fe_{2/3}W_{1/3})O_3$
Improper	Structural transition 'Geometric ferroelectrics'	K_2SeO_4 , Cs_2CdI_4 hexagonal $RMnO_3$
	Charge ordering 'Electronic ferroelectrics'	$LuFe_2O_4$
	Magnetic ordering 'Magnetic ferroelectrics'	Orthorhombic $RMnO_3$, RMn_2O_5 , $CoCr_2O_4$

Table 1-1: *The classification of ferroelectrics: proper and improper ferroelectricity [23]*

In this dissertation, we will focus on the “improper” ferroelectric materials which are geometric ferroelectrics $ReMnO_3$. The multiferroic rare-earth manganites ($ReMnO_3$) have attracted great scientific attention since the manifestations of the intriguing and significant coupling between the magnetic and electric order parameters. The coexistence of ferroic orders in $ReMnO_3$ with hexagonal (smaller ionic radius of rare-earth $Re = Sc, Y,$ and $Ho-Lu$) or orthorhombic (larger ionic radius of rare-earth $Re = La-Dy$) (shown in Fig. 1-2) structure not only gives the rich physics in the intimate interactions among charge, orbital, lattice, and spin degrees of freedom but also possesses some fascinating physical properties which might lead to the potential applications. As indicated in Table 1.1, $ReMnO_3$ has two kinds of ferroelectric behaviors (hexagonal or orthorhombic) induced via different originations. The

rare-earth (Re^{3+}) ionic size decreases from 1.11 Å to 0.94 Å with decreasing the atomic number and reducing the electrons residing in the 4f orbit which formed the so-called lanthanum contraction effect [28]. The Re^{3+} ions of the rare-earth elements have closely chemical properties because the outermost electrons with the same $5s^25p^6$ electronic configurations, like neutral xenon. The orthorhombic structure with $Pnma$ space group is the stable crystal structure of $ReMnO_3$ perovskite oxides with $Re = La$ to Dy , which belongs to the magnetic ferroelectrics induced by magnetic ordering [29-36]. On the other hand, another group of compounds with small ionic size (for $Re = Y, Ho, Er, Yb, Lu,$ and etc.) forms the stable hexagonal structure with $P6_3cm$ space group. The critical point of the structure transition locates near $YMnO_3$ ($Y^{3+} = 1.06\text{Å}$) and $HoMnO_3$ ($Ho^{3+} = 1.05\text{Å}$). Consequently, the crystal structures of those two compounds have been transformed from hexagonal to orthorhombic (or vice versa) by a lot of experimental techniques, e.g. high temperature and high pressure processes [37-38], chemical solution deposition (CSD) [39], the metal-organic chemical vapor deposition (MOCVD) [40], molecular beam epitaxy (MBE) [41], sputtering [42], and pulsed laser deposition (PLD) [43].

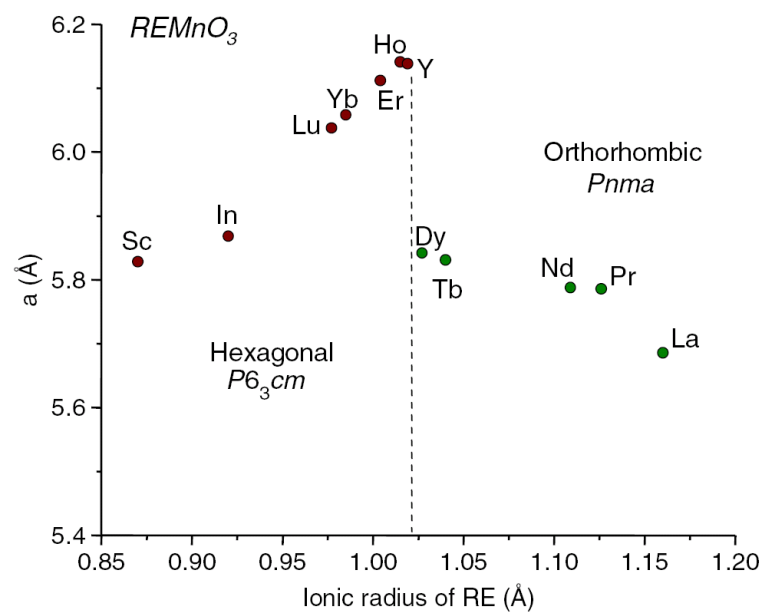


Figure 1-2: The evolution of the lattice structure in $ReMnO_3$ as a function of the size of the rare earth (Re) [22].

In the following sections, we are going to change the point of view which is from the development of history to the recent researches of the multiferroic hexagonal manganites ($ReMnO_3$). Due to the effect of geometric structure, the magnetic frustration appears in the improper ferroelectricity in $ReMnO_3$. Thus, we are interested in the interactions among the charge, lattice, and spin degrees of freedom in this kind of strong correlated system. Furthermore, we will present the motivation of our study in the hexagonal manganites.



1.1 Survey the researches of hexagonal $ReMnO_3$ materials

The hexagonal $ReMnO_3$ (Re = rare-earth) materials show the similar properties among various rare-earth elements, whether the properties of electric transportation or magnetic behaviors. Following, our discussions will focus on the properties of the hexagonal $HoMnO_3$ (h -HMO), because h -HMO is an intriguing multiferroic. The hexagonal $HoMnO_3$ is with the ferroelectric ordering at Curie temperature $T_C = 875$ K, the antiferromagnetic (AFM) Mn^{3+} ordering at Néel temperature $T_N = 76$ K, and the magnetic Ho^{3+} ordering at $T_{HO} = 4.6$ K, in which the magnetically active ions are the high spin Mn^{3+} ($3d^4$, $S = 2$) and Ho^{3+} ($4f^{10}$) (ground-state multiple 5I_8) [6, 26, 44-50]. Fig. 1-3 (a) and (b) show the crystal structure of hexagonal $ReMnO_3$ at paraelectric ($P6_3/mmc$) and ferroelectric ($P6_3cm$) phase, respectively [51].

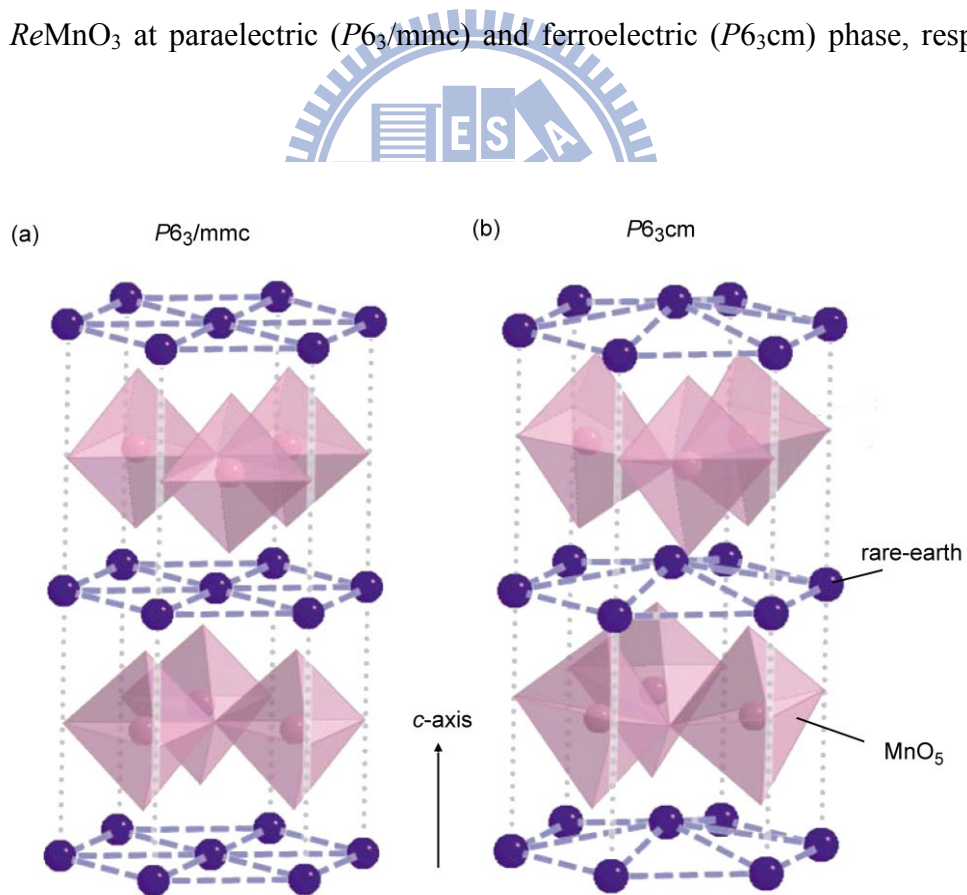


Figure 1-3: Schematic crystal structures of $ReMnO_3$ in hexagonal structure. (a) High symmetry phase ($P6_3/mmc$). (b) Low symmetry phase ($P6_3cm$) [51].

What is the origin of the ferroelectricity in magnetoelectric $ReMnO_3$? B. B. van Aken *et al.* [26] reported the ferroelectric phase transition in the hexagonal manganite $YMnO_3$ through the detailed structure analysis from x-ray diffraction and the first principle density functional calculations. The ferroelectric phase is characterized by a buckling of the layered MnO_5 polyhedra and accompanied by the displacements of the Y ions, which lead to a net electric polarization. Similar results had been shown by Th. Lonkai *et al.* [52]. Fig. 1-4 shows the “geometric” generation of polarization in $YMnO_3$ and describes the tilting of a rigid MnO_5 block with a magnetic Mn atom at the center.

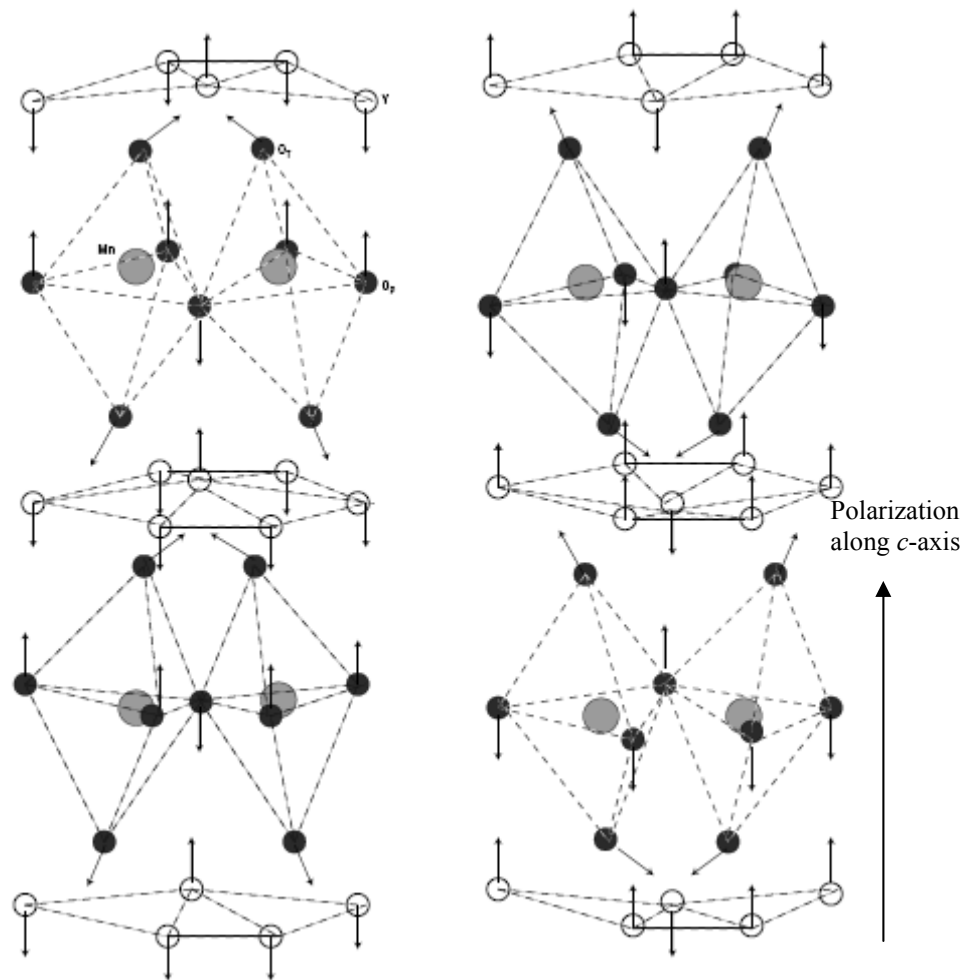


Figure 1-4: Schematic crystal structure of $YMnO_3$. Arrows indicate the directions of the atomic displacements moving from the centrosymmetric to the ferroelectric structure [26].

The magnetic structures of *h*-HMO have been studied by various experimental methods, such as neutron diffraction [50, 53] or second harmonic generation (S.H.G.) [45, 54]. In the $P6_3cm$ hexagonal phase, each Mn^{3+} ion is surrounded by five O^{2-} ions and formed triangular planar sublattices in the basal plane (*a-b* plane). The magnetic order of Mn^{3+} is mainly dominated by AFM in-plane Mn-O-Mn superexchange interaction. Therefore, the triangular lattice of the Mn atoms exhibits strong geometrical frustration effect [55]. Furthermore, when temperature cool to near T_N , the strong superexchange leads to a 120° arrangement between neighboring Mn^{3+} spins in the basal plane which breaks the triangular frustration. In addition, the spins of Mn rotate with an angle of 90° at T_{SR} (e.g. for *h*- $HoMnO_3$, $T_{SR} \sim 33$ K) due to the onset of the AFM order of the Ho moments indicating that the interaction between Ho^{3+} and Mn^{3+} spins. Another magnetic transition at $T_{Ho} \sim 5$ K involves with the complete magnetic order of the Ho^{3+} ions. These spin arrangements at different temperatures are shown in Fig. 1-5.

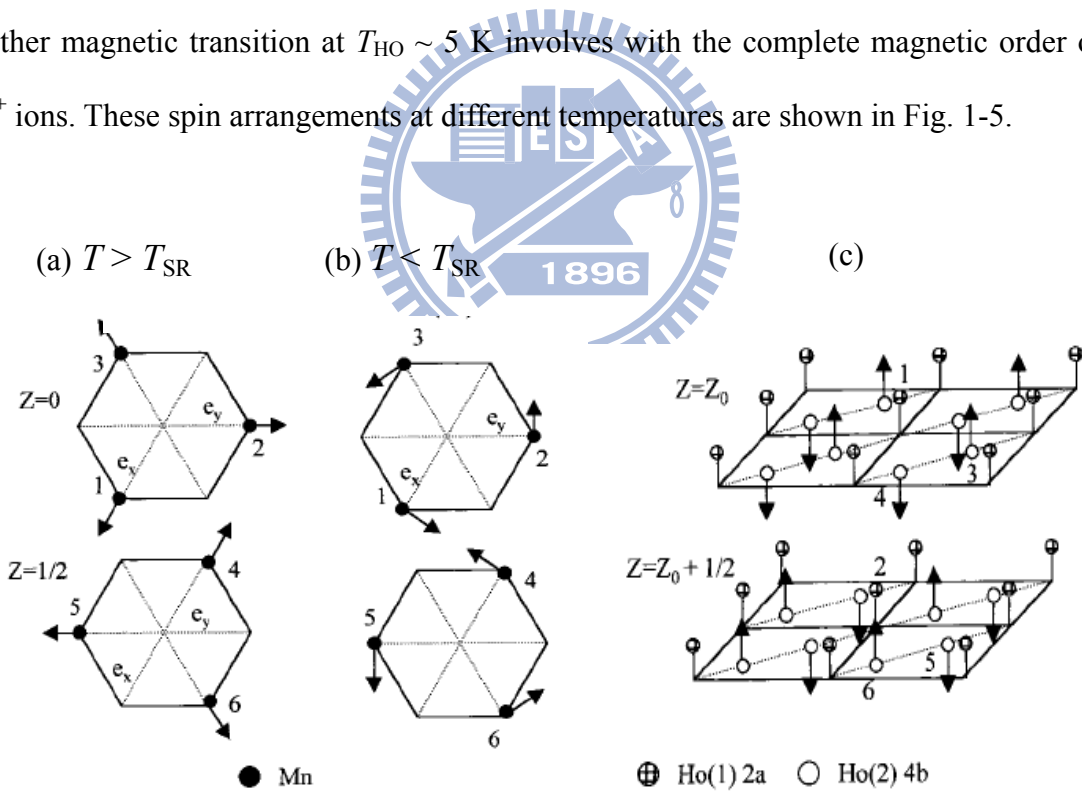


Figure 1-5: Scheme of the magnetic structure of $HoMnO_3$: (a) $T_{SR} < T < T_N$, (b) $T < T_{SR}$, (c) $T < T_{Ho}$ [53].

In addition to the basic properties of ferroelectricity and magnetization, in 1997,

Huang *et al.* [56] have reported that the anomaly of the dielectric constant at Néel temperature (T_N) which is due to the coupling between the ferroelectric and antiferromagnetic order parameters (the arrow in Fig. 1-6 (a)). Moreover, during 2004-2005, B. Lorenz *et al.* observed a reentrant phase in the hexagonal ferroelectric HoMnO_3 below the temperature of so-called spin rotation (T_{SR}) shown in Fig. 1-6 (b). Under applied magnetic fields, HoMnO_3 exhibits complex T - H phase diagram with several field-induced reentrant phases and transitions at low temperatures shown in Fig 1-6 (c) [57-59].

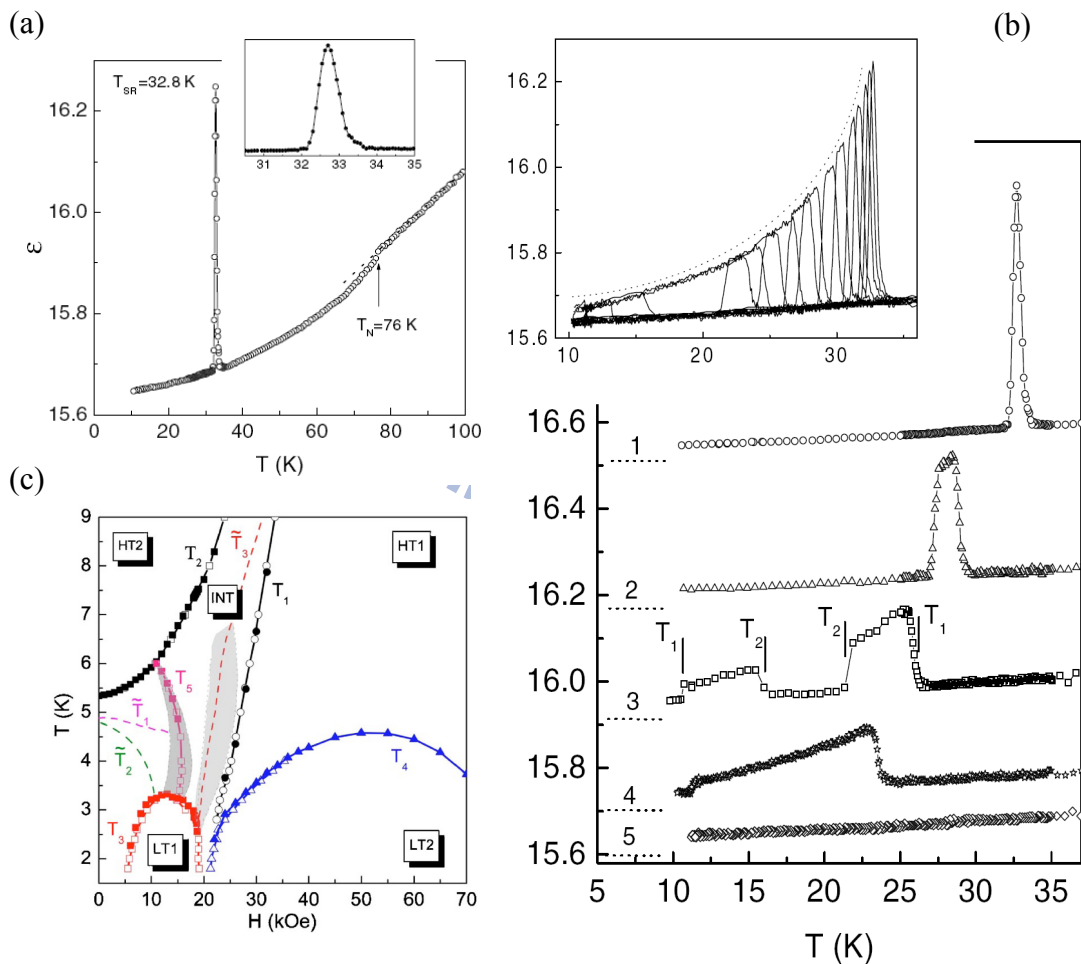


Figure 1-6: (a) There are two anomalies behaviors shown in the low temperature dielectric constant. (b) The dielectric constant plotted as a function of temperature with several external magnetic fields. (c) The low temperature T - H phase diagram of HoMnO_3 [57-59].

The magnetoelectric coupling in HoMnO_3 will be discussed in chapter 4 of this dissertation. Briefly, the anomalous dielectric constant at T_N along c -axis in hexagonal ReMnO_3 has been assigned to the indirect coupling via lattice strain (spin-lattice coupling). Moreover, there are many researches show that the abnormal behavior at T_N , such as the heat capacity measurements, the lattice constant measurements, and etc., which are shown in Fig. 1-7(a) and (b) [58, 60-61].

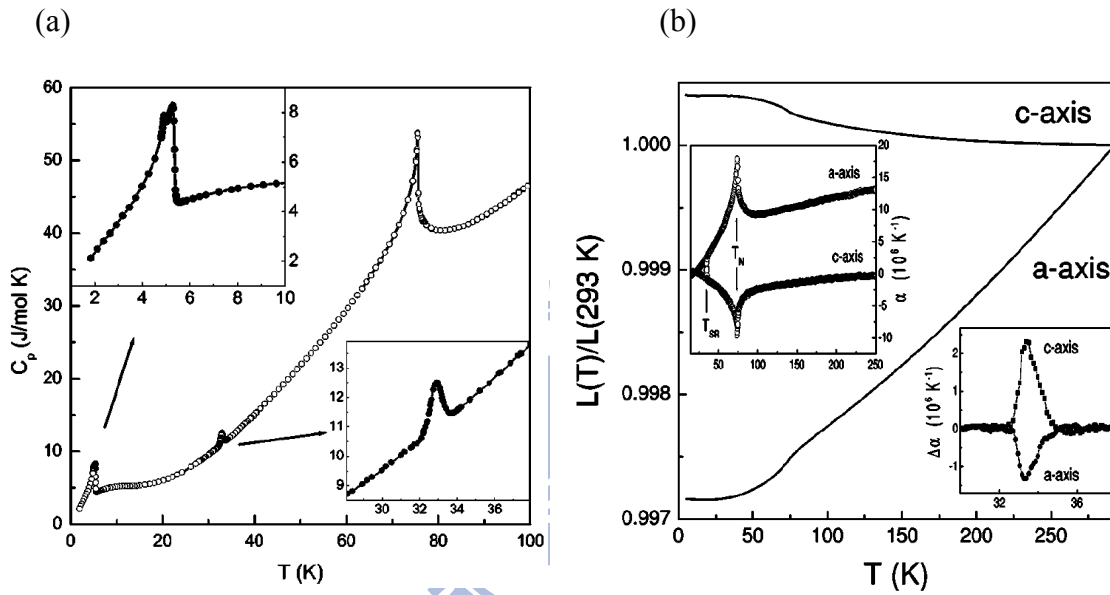


Figure 1-7: (a) The λ -type anomaly around T_N in the specific heat of HoMnO_3 . (b) The temperature-dependent lattice constant along a - and c -axis [60-61].

Very recently, Lee *et al.* [62] observed the giant magnetoelastic effect in hexagonal YMnO_3 and LuMnO_3 by using the high-resolution neutron and synchrotron powder diffraction experiments (shown in Fig. 1-8). They further claimed that the magnetoelectric (ME) coupling can be interpreted by the giant magnetoelastic effect very well in ReMnO_3 , i.e. the magnetic long-range ordering induced the very large displacements of all atoms at Néel temperature. In other words, the magnetoelastic coupling let the atoms undergo an isostructural transition, which has been regarded as the primary source of the ME phenomena. In hexagonal ReMnO_3 , this magnetoelastic effect is two orders of magnitude larger than those

appeared in other magnetic materials. Therefore, the gigantic magnetoelastic coupling plays a crucial role to dominate a lot of physical properties in hexagonal $ReMnO_3$.

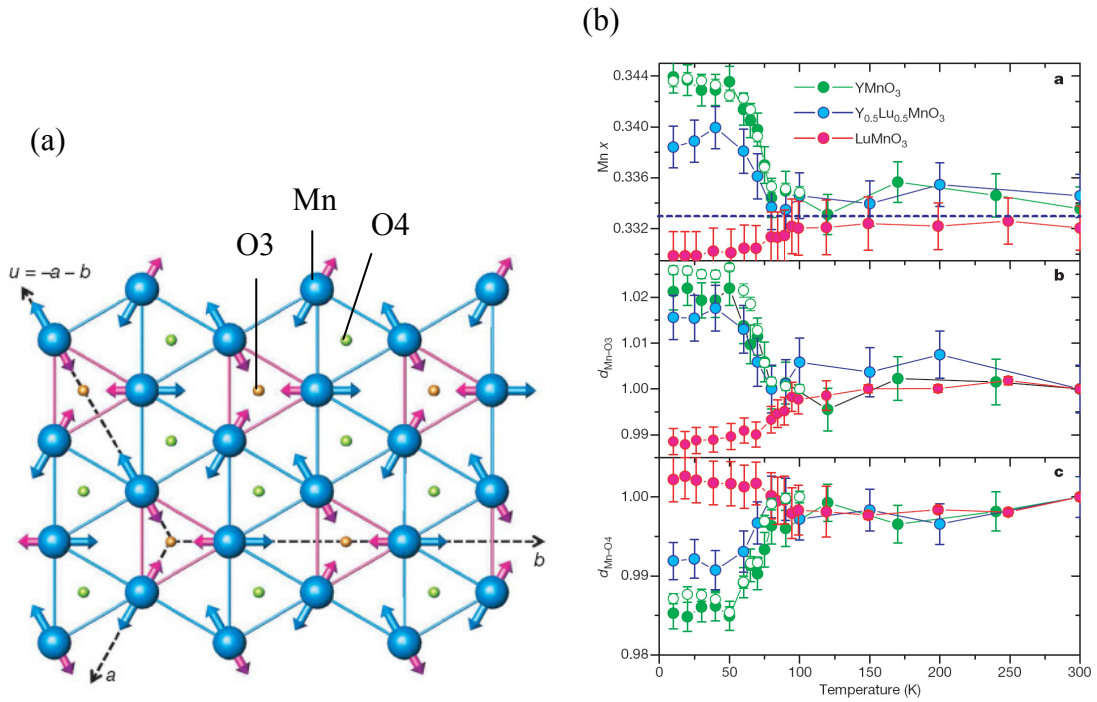


Figure 1-8: (a) The model shows how Mn atoms (large blue circles) move below T_N with respect to O3 atoms (small orange circles). (b) Temperature dependent of the Mn x position and the Mn-O bond distances [62].

1.2 Motivation

The previous research results as mentioned above show the rich physical phenomena in hexagonal $ReMnO_3$ multiferroic materials caused by the strong interaction among charge, lattice, and spin degrees of freedom. N. A. Spaldin and M. Fiebig further proposed the strong coupling among the electric polarization (P), magnetization (M), and strain (ϵ). Also, one of them can be changed by driving the other physical parameters [63] as shown in Fig. 1-9. Thus, to understand the strong interaction among different order parameters in hexagonal $ReMnO_3$ multiferroic materials must be a key issue.

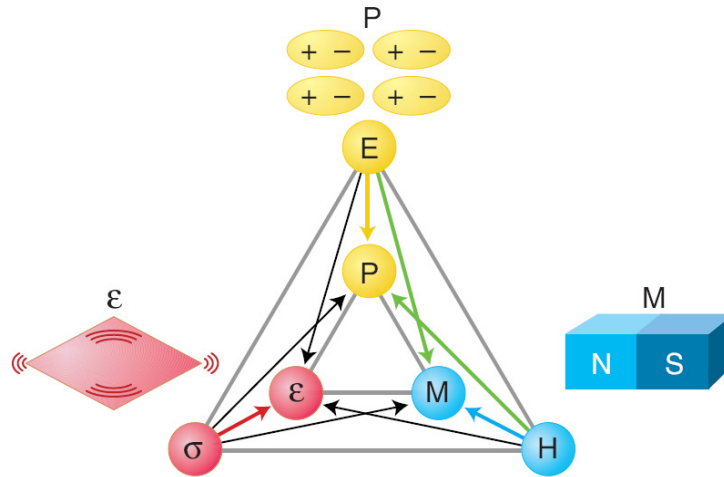


Figure 1-9: *The electric field E , magnetic field H , and stress σ control the electric polarization P , magnetization M , and strain ε , respectively [63].*

Our motivation is to understand the correlation among different degrees of freedom by pump-probe spectroscopy with femtosecond time-resolution. Through the pump-probe spectroscopy, we can observe the rapid responses in materials, such as the relaxation time of the excited electrons from excited state to ground state in several picosecond. Thus, the

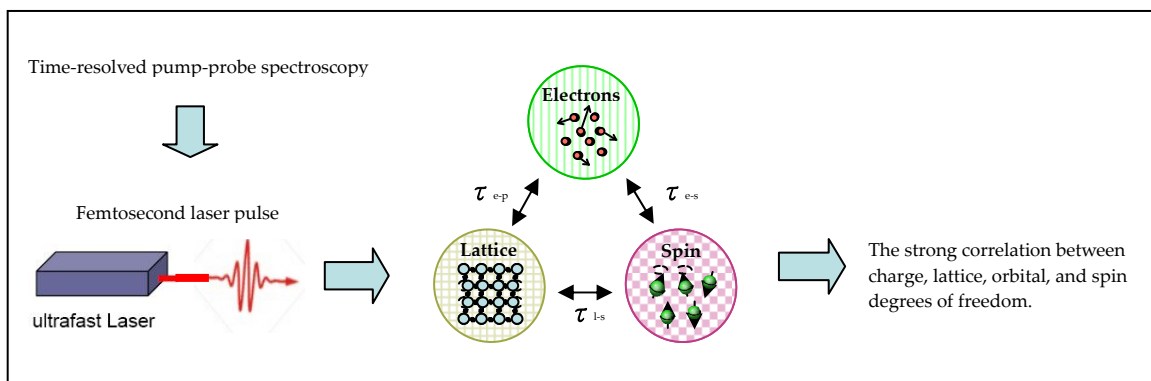


Figure 1-10: *The flow chart of our motivation. Utilize the ultrashort pulse laser as a tool to investigate the strong correlation between different kinds of degrees of freedom.*

intricate correlation processes among the charge, lattice, and spin degrees of freedom can be

explicitly recognized in different characteristic time scales by measuring the transient reflectivity or transmittance. From the ultrafast dynamical spectroscopy, the microscopic mechanism of the magnetoelectric coupling or magnetoelastic behavior can be revealed.

1.3 The organization of this dissertation

This dissertation consists of five chapters. In chapter 1, we simply introduce the multiferroic materials and magnetoelectric coupling phenomena. The motivation of this study is also included. In chapter 2, we give a brief introduction to the growth of high quality samples. Moreover, the crystal structures and orientations of all samples were examined by x-ray diffraction (XRD). The magnetic properties of all samples were inspected by a Quantum Design® superconducting quantum interference device (SQUID) system. The other focal point in chapter 2 is the system setup of the ultrafast femtosecond pump-probe and described in details. In chapter 3, we are going to discuss the fundamental principle of pump-probe technique. First, we present the fundamental physics in ultrashort pulse laser. Next, we discuss the principle of time-resolved pump-probe spectroscopy. Finally, we focus on the origin of the coherent spike signals induced by two laser beam interference. In chapter 4, we present all of the pump-probe experimental results. The pump induced dynamics of electrons, holes, and phonons are influenced by their interaction with each other. We demonstrate and explain that the ultrafast dynamics of electrons and lattice in hexagonal HoMnO_3 (*h*-HMO) single crystals. In the pump-probe experiments, we observed the dynamical behavior of electrons coupling with antiferromagnetic (AFM) ordering at Néel temperature (T_N) which is magnetoelectric coupling. Moreover, through the ultrafast lattice dynamics we directly observed the giant and anisotropic magnetoelastic coupling at T_N on *a-b* plane and along *c*-axis. In chapter 5, we summarize the significant results in this dissertation.

References

- [1] H. Schmid, *Ferroelectrics* **162**, 317 (1994).
- [2] M. Fiebig, *J. Phys. D* **38**, R123 (2005).
- [3] C. W. Nan, M. I. Bichurin, S. Dong, and D. Viehland, G. Srinivasan, *J. Appl. Phys.* **103**, 031101 (2008).
- [4] D. Khomskii, *Physics* **2**, 20 (2009).
- [5] W. Eerenstein, N. D. Mathur, and J. F. Scott, *Nature (London)* **442**, 759 (2006).
- [6] T. Lottermoser, T. Lonkai, U. Amann, D. Hohlwein, J. Ihringer, M. Fiebig, *Nature* **430**, 541 (2004).
- [7] B. Lorenz, Y. Q. Wang, and C. W. Chu, *Phys. Rev. B* **76**, 104405 (2007).
- [8] B. Lorenz, Y. Q. Wang, Y. Y. Sun, and C. W. Chu, *Phys. Rev. B* **70**, 212412 (2004).
- [9] T. Kimura, T. Goto, H. Shintani, K. Ishizaka, T. Arima, and Y. Tokura, *Nature*. **426**, 55 (2003).
- [10] M. Fiebig, T. Lottermoser, D. Frohlich, A.V. Goitsev, and R.V. Pisarev, *Nature* **419**, 818 (2002).
- [11] N. Hur, S. Park, P. A. Sharma, J. S. Ahn, S. Guha, and S.-W. Cheong, *Nature* **429**, 392 (2004).
- [12] P. Curie, *J. Physique* **3**, 393 (1894).
- [13] L. D. Landau and E. M. Lifshitz, *Electrodynamics of continuous media (Fizmatgiz, Moscow)* (1959).
- [14] I. E. Dzyaloshinskii, *Sov. Phys. JETP* **10**, 628 (1959).
- [15] D. N. Astrov, *Sov. Phys. JETP* **11**, 708 (1960).
- [16] B. I. Alshin and D. N. Astrov, *Sov. Phys. JETP* **17**, 809 (1963).
- [17] E. Ascher, H. Rieder, H. Schmid, and H. Stoessel, *J. Appl. Phys.* **37**, 1404 (1966).
- [18] C. Michel, J. M. Moreau, G. D. Achenbach, R. Gerson, and W. J. James, *Solid state*

- Comm. **7**, 701 (1969).
- [19] G. T. Rado, Phys. Rev. Lett. **13**, 335 (1964).
- [20] B. B. Krichevstov, V. V. Pavlov, and R. V. Pisarev, JETP Lett. **49**, 535 (1989).
- [21] N. A. Hill, Annu. Rev. Mater. Res. **32**, 1 (2002).
- [22] W. Prellier, M. P. Singh, and P. Murugavel, J. Phys.: Condens. Matter **17**, R803 (2005).
- [23] S. -W. Cheong and M. Mostovoy, Nature Mater. **6**, 13 (2007).
- [24] A. P. Levanyuk and D. G. Sannikov, Sov. Phys. Usp. **17**, 199 (1974).
- [25] T. Katsufuji, S. Mori, M. Masaki, Y. Moritomo, N. Yamamoto, and H. Takagi, Phys. Rev. B **64**, 104419 (2001).
- [26] B. B. Van Aken, T. T. M. Palstra, A. Filippetti, and N. A. Spaldin, Nature Mater. **3**, 164 (2004).
- [27] C. J. Fennie and K. M. Rabe, Phys. Rev. B **72**, 100103 (2005).
- [28] C. Kittel, Introduction to Solid State Physics, 8th. Edition (Wiley, 2005), p. 305.
- [29] T. Kimura, T. Goto, H. Shintani, K. Ishizaka, T. Arima, and Y. Tokura, Nature **426**, 55 (2003).
- [30] T. H. Lin, H. C. Shih, C. C. Hsieh, C. W. Luo, J.-Y. Lin, J. L. Her, H. D. Yang, C.-H. Hsu, K. H. Wu, T. M. Uen, and J. Y. Juang, J. Phys.: Condens. Matter **21**, 026013 (2009).
- [31] T. C. Han, J. G. Lin, C. T. Wu, M. W. Chu, and C. H. Chen, Jpn. J. Appl. Phys. **49**, 041501 (2010).
- [32] K. H. Wu, I. C. Gou, C. W. Luo, T. M. Uen, J.-Y. Lin, J. Y. Juang, C. K. Chen, J. M. Lee, and J. M. Chen, Thin Solid Films **518**, 2275 (2010).
- [33] J. M. Chen, T. L. Chou, J. M. Lee, S. A. Chen, T. S. Chan, T. H. Chen, K. T. Lu, W. T. Chuang, H.-S. Sheu, S. W. Chen, C. M. Lin, N. Hiraoka, H. Ishii, K. D. Tsuei, and T. J. Yang, Phys. Rev. B **79**, 165110 (2009).
- [34] T. H. Lin, C. C. Hsieh, H. C. Shih, C. W. Luo, T. M. Uen, K. H. Wu, J. Y. Juang, J.-Y. Lin,

- C.-H. Hsu, and S. J. Liu, *Appl. Phys. Lett.* **92**, 132503 (2008).
- [35] C. C. Hsieh, T. H. Lin, H. C. Shih, C.-H. Hsu, C. W. Luo, J.-Y. Lin, K. H. Wu, T. M. Uen, and J. Y. Juang, *J. Appl. Phys.* **104**, 103912 (2008).
- [36] T. H. Lin, C. C. Hsieh, C. W. Luo, J.-Y. Lin, C. P. Sun, H. D. Yang, C.-H. Hsu, Y. H. Chu, K. H. Wu, T. M. Uen, and J. Y. Juang, *J. Appl. Phys.* **106**, 103923 (2009).
- [37] M. N. Iliev, M. V. Abrashev, H. G. Lee, V. N. Popov, Y. Y. Sun, C. Thomsen, R. L. Meng, and C. W. Chu, *Phys. Rev. B* **57**, 2872 (1998).
- [38] J. S. Zhou and J. B. Goodenough, *Phys. Rev. Lett.* **96**, 247202 (2006).
- [39] W. C. Yi, C. S. Seo, S. I. Kwun, and J. G. Yoon, *Appl. Phys. Lett.* **77**, 1044 (2000).
- [40] H. N. Lee, Y. T. Kim, and S. H. Choh, *Appl. Phys. Lett.* **76**, 1066 (2000).
- [41] S. Imada, T. Kuraoka, E. Tokumitsu, and H. Ishiwara, *Jpn. J. Appl. Phys.* **40**, 666 (2001).
- [42] Y. T. Kim, I. S. Kim, S. I. Kim, D. C. Yoo, and J. Y. Lee, *J. Appl. Phys.* **94**, 4859 (2003)
- [43] T. Yoshimura, N. Fujimura, and T. Ito, *Appl. Phys. Lett.* **73**, 414 (1998).
- [44] B. G. Ueland, J. W. Lynn, M. Laver, Y. J. Choi, and S.-W. Cheong, *Phys. Rev. Lett.* **104**, 147204 (2010).
- [45] M. Fiebig, D. Fröhlich, K. Kohn, St. Leute, Th. Lottermoser, V. V. Pavlov, and R. V. Pisarev, *Phys. Rev. Lett.* **84**, 5620 (2000).
- [46] M. Fiebig, C. Degenhardt, and R. V. Pisarev, *Phys. Rev. B* **88**, 027203 (2001).
- [47] O. P. Vajk, M. Kenzelmann, J. W. Lynn, S. B. Kim, and S.-W. Cheong, *Phys. Rev. Lett.* **94**, 087601 (2005).
- [48] H. Lueken, *Angew. Chem. Int. Ed.* **47**, 8562 (2008).
- [49] Daniel Khomskii, *Physics* **2**, 20 (2009).
- [50] A. Muñoz, J. A. Alonso, M. J. Martínez-Lope, M. T. Casáis, J. L. Martínez, and M. T. Fernández-Díaz, *Phys. Rev. B* **62**, 9498 (2000).
- [51] T. Tohei, H. Moriwake, H. Murata, A. Kuwabara, R. Hashimoto, T. Yamamoto, and I.

- Tanaka, Phys. Rev. B **79**, 144125 (2009).
- [52] Th. Lonkai, D. G. Tomuta, U. Amann, J. Ihringer, R. W. A. Hendrikx, D. M. Többens, and J. A. Mydosh, Phys. Rev. B **69**, 134108 (2004).
- [53] A. Muñoz, J. A. Alonso, M. J. Martínez-Lope, M. T. Casáis, J. L. Martínez, and M. T. Fernández-Díaz, Chem. Mater. **13**, 1497 (2001).
- [54] M. Fiebig, C. Degenhardt, and R.V. Pisarev, J. Appl. Phys. **91**, 8867 (2002).
- [55] Th. Lonkai, D. G. Tomuta, and J.-U. Hoffmann, J. Appl. Phys. **93**, 8191 (2003).
- [56] Z. J. Huang, Y. Cao, Y. Y. Sun, Y. Y. Xue, and C. W. Chu, Phys. Rev. B **56**, 2623 (1997).
- [57] B. Lorenz, A. P. Litvinchuk, M. M. Gospodinov, and C. W. Chu, Phys. Rev. Lett. **92**, 087204 (2004).
- [58] B. Lorenz, F. Yen, M. M. Gospodinov, and C. W. Chu, Phys. Rev. B **71**, 014438 (2005).
- [59] F. Yen, C. R. dela Cruz, B. Lorenz, Y. Y. Sun, Y. Q. Wang, M. M. Gospodinov, and C. W. Chu, Phys. Rev. B **71**, 180407(R) (2005).
- [60] D. G. Tomuta, S. Ramakrishnan, G. J. Nieuwenhuys, and J. A. Mydosh, J. Phys.: Condens. Matter **13**, 4543 (2001).
- [61] C. dela Cruz, F. Yen, B. Lorenz, Y. Q. Wang, Y. Y. Sun, M. M. Gospodinov, and C. W. Chu, Phys. Rev. B **71**, 060407(R) (2005).
- [62] Seongsu Lee, A. Pirogov, Misun Kang, Kwang-Hyun Jang, M. Yonemura, T. Kamiyama, S.-W. Cheong, F. Gozzo, Namsoo Shin, H. Kimura, Y. Noda, and J.-G. Park, Nature **451**,809 (2008).
- [63] N. A. Spaldin, and M. Fiebig, Science **309**, 391 (2005).

Chapter 2

Experimental tools and procedures

Time-resolved spectroscopy is a very important and direct tool for investigating the problems of carrier dynamics. In this chapter, we will briefly discuss and describe the experimental systems and some other significant experiments. The basic properties of the *h*-HMO crystals will be shown first. Then, the optical measurement systems will be described in detailed.

2.1 Characterization and preparation of *h*-HMO single crystals

The fabrication of single crystals is very important for both fundamental researches and industrial purposes. Figure 2-1 shows the hexagonal HoMnO₃ single crystals used in this study. The pure polycrystalline hexagonal HoMnO₃ single crystals were synthesized by a solid-state reaction of stoichiometric amount of Ho₂O₃ (99.99 %) and MnO₂ (99.99 %). The single crystals of hexagonal HoMnO₃ have been grown via the high temperature flux method [1-3] and in a floating zone furnace. The samples were synthesized for 15 hours at 1290 °C, then annealed for 5 hours at 1150 °C in a platinum crucible and in an oxygen atmosphere.

After that, the temperature was decrease to room temperature with a rate of 1 °C/h. The flux was decanted and well-shaped hexagonal platelike crystals with typical size of $2 \times 3 \times 0.25$ mm³ were removed from the bottom of the crucible.



Figure 2-1: *The HoMnO₃ single crystals used in this study. The largest surface is around 3×3 mm² and the thickness of this crystal is about 0.5 mm*

2.1.1 Orientation and structure of HoMnO₃ single crystals

After growing the HoMnO₃ single crystals, the most important thing is to characterize their physical properties. Fig. 2-2 shows the X-ray diffraction (XRD) θ - 2θ pattern (Cu K α , $\lambda = 1.5406$ Å) for the *h*-HMO single crystals grew by the floating zone furnace method. The XRD data evidently confirm the formation of the pure hexagonal HoMnO₃ with the *c*-axis (space group: *P6₃cm*) oriented normal to the largest crystal surface. The crystal structure of HoMnO₃ has been shown in section 1.1 of chapter 1. The full width at half maximum (FWHM) ($\approx 0.25^\circ$) of X-ray data indicates the good crystalline quality and grain alignment of the *h*-HMO crystals. To further examine the in-plane texture of the crystals, we also measured the ϕ -scan around the *h*-HMO reflection. The ϕ -scans display an evenly behaved six-fold symmetry,

indicating that the in-plane grain alignment on the a - b plane well. The fitted lattice constant of HoMnO_3 single crystals for a - and c -axis were 6.142 Å and 11.408 Å, respectively [4-7].

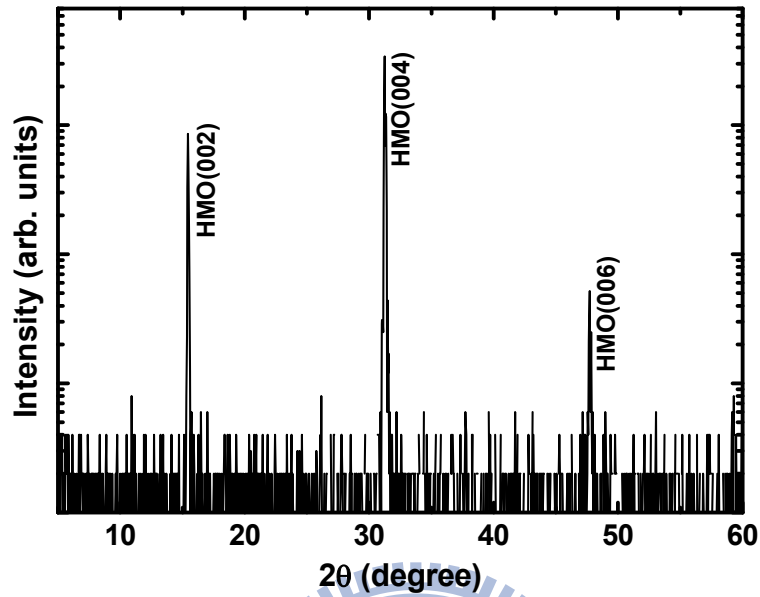


Figure 2-2: The XRD results of the h -HMO single crystals grew by the floating zone furnace method. The θ - 2θ scans (plotted in semi-logarithmic scale) reveal that HMO crystals indeed hexagonal with c -axis orientation.

The other useful parameters, e.g. lattice parameters, atomic positions, and discrepancy factors in Table. 2-1, from high-resolution neutron diffraction experiments were reported by A. Muñoz *et al.* [8].

atoms		x	y	z	B (Å ²)
Ho(1)	2a	0	0	0.2731(16)	0.18(5)
Ho(2)	4b	$1/3$	$2/3$	0.2306(12)	0.18(5)
Mn	6c	0.3224(32)	0	0	0.18(5)
O(1)	6c	0.3054(13)	0	0.1600(13)	0.52(5)
O(2)	6c	0.6433(12)	0	0.3326(13)	0.52(5)
O(3)	4b	0	0	0.4763(23)	0.63(6)
O(4)	2a	$1/3$	$2/3$	0.0170(15)	0.63(6)
unit cell		$a = 6.1413(1)$ Å	$c = 11.4122(3)$ Å	$V = 372.76(1)$ Å ³	
discrepancy factors		$R_p = 3.7\%$	$R_{wp} = 4.7\%$	$R_{Brag} = 4.4\%$	$\chi^2 = 1.1$

Table 2-1: The lattice constant, atomic positions, and discrepancy factors corresponding to the crystal structure of HoMnO_3 [8].

2.1.2 Temperature-dependent susceptibility measurements

The magnetic properties were measured in a Quantum Design® superconducting quantum interference device (SQUID) system. Fig. 2-3(a) and (b) show the characteristics of magnetization in the platelet samples examined by SQUID. The Mn-spin rotation transition ($T_{SR} \sim 33$ K) and the magnetic order of the Ho^{3+} ions ($T_{\text{Ho}} \sim 5$ K) could be clearly observed in the magnetization measurements (the arrows in Fig. 2.2(a) and the enlarge scale in Fig. 2-3(b)). However, the AFM transition of $h\text{-HoMnO}_3$ is difficult recognized in magnetization measurements due to the huge paramagnetic signal from rare-earth ion. These results consist with those reported by other researchers [9].

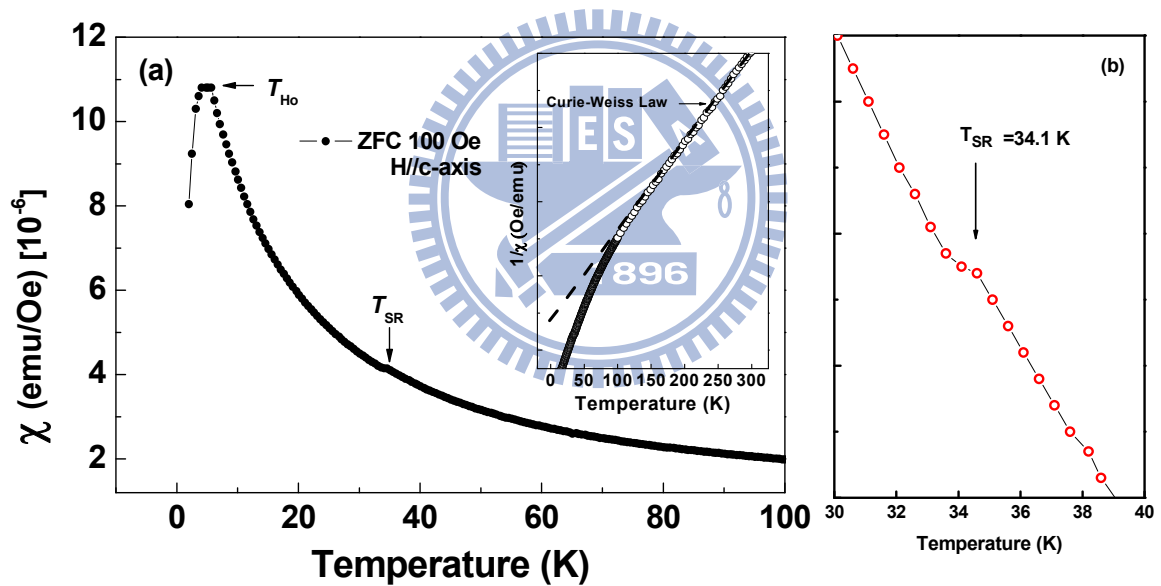


Figure 2-3: (a) The temperature-dependent susceptibility ($\chi(T)$) of $h\text{-HMO}$ with a magnetic field of 100 Oe applied along c -axis. The inset shows the inverse susceptibility. The dashed line: the Curie-Weiss high temperature extrapolation. (b) To enlarge the figure in order to show the behavior of spin rotation.

The AFM exchange coupling in a triangular lattice gives rise to spin frustration effects and, at T_N the Mn^{3+} moments order in a way so that neighboring Mn-moments form a 120° angle [10]. In addition, most rare-earth ions carry their own magnetic moment oriented along

the c -axis of the $P6_3cm$ structure. The rare-earth moment can interact with the Mn^{3+} spins and the dielectric polarization and thus increase the complexity of the phase diagram and the physical phenomena that can be observed. For example, the complex magnetic phase transition and different spin arrangements have been canvassed by the second harmonic generation or the neutron scattering measurements [8,11-12] which show two additional phase transitions below T_N indicating subtle changes in the magnetic order of the Mn^{3+} and Ho^{3+} ions at zero external magnetic field. At $T_{SR} \sim 33$ K, a sharp Mn-spin reorientation transition takes place at which all Mn-moments rotate in-plane with an angle of 90° and changes the magnetic symmetry from $P\bar{6}_3cm$ ($T > T_{SR}$) to $P6_3cm$ ($T < T_{SR}$) (illustrated in Fig. 2-4 [10]). At lower temperatures, $T_{Ho} \sim 5$ K, another change of the magnetic structure has been reported but the magnetic order in this phase is still a matter of discussion. The transitions at T_{SR} and T_{Ho} are accompanied by partial or complete magnetic ordering of the Ho^{3+} moments, but the detail of the Ho-spin order has not been resolved yet. All magnetic transitions are well below the FE Curie temperature of $T_C = 875$ K.

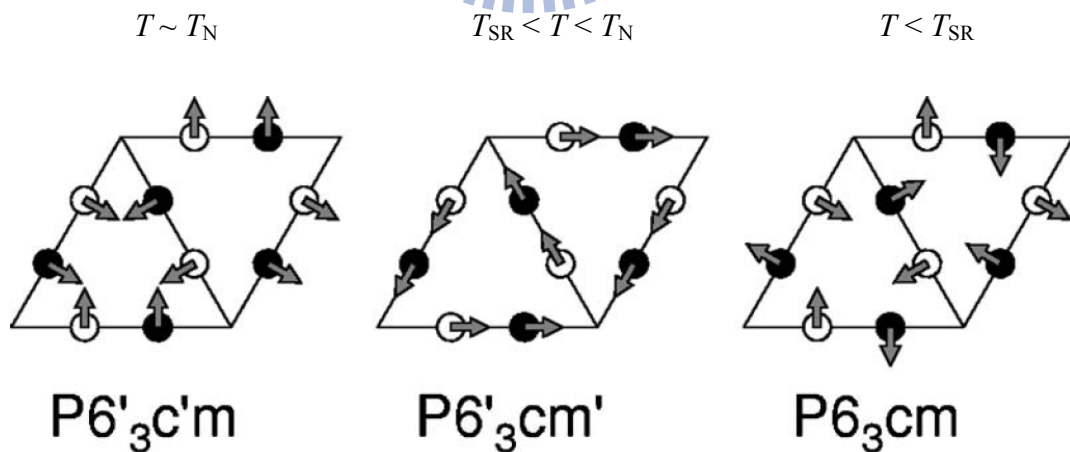


Figure 2-4: The three Mn^{3+} spin configuration in hexagonal $HoMnO_3$ [10]. The open circles indicate Mn ions at $z=0$, filled circles indicate Mn ions at $z=c/2$.

2.1.3 Transmittance spectrum

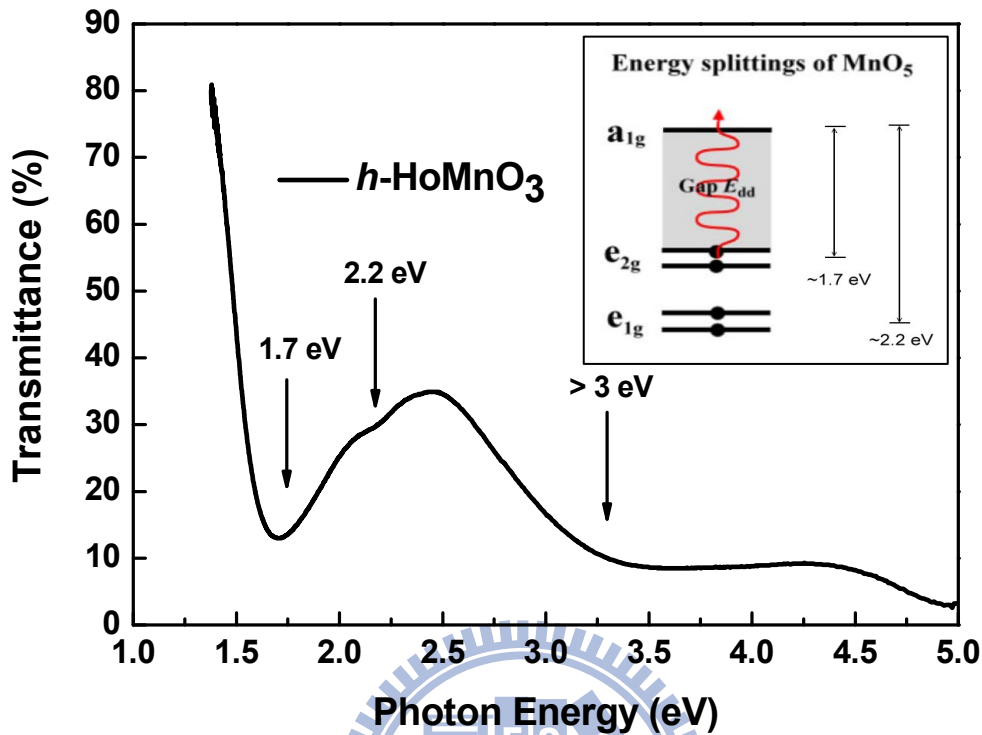


Figure 2-5: The transmittance spectrum of hexagonal HoMnO_3 single crystals. The arrows show the three features. The inset shows the local environment MnO_5 for photon energy above and below E_{dd} .

Fig. 2-5 shows the transmittance spectrum in the HoMnO_3 single crystals which was measured by a grating-type spectrophotometer (HITACHI high-technologies Corporation) in the photon energy range of 0.7-5.0 eV. According to the literatures [13-16], there are three common features in the absorption spectrum of hexagonal ReMnO_3 which performed by Fourier-transform infrared spectrometer. First, the optical excitation causes the absorption peak near ~ 1.7 eV at low temperature which is attributed to the charge transfer from e_{2g} orbitals (d_{xy} and $d_{x^2-y^2}$) to a_{1g} orbitals ($d_{3z^2-r^2}$). Second, the relatively weak peak near ~ 2.2 eV comes from the charge transfer from e_{1g} orbitals (d_{xz} and d_{yz}) to a_{1g} orbitals ($d_{3z^2-r^2}$) between the Mn 3d levels. Finally, a much stronger absorption peak at higher energy region above 3 eV caused by the continuous charge transfer from O 2p to Mn 3d states as shown in Fig. 2-5. In virtue of the transition metal Mn^{3+} ion sits at the center of a triangular bipyramid

of five O^{2-} ions at each corner, the d orbitals of the Mn^{3+} ion are split into three parts (e_{1g} , e_{2g} , a_{1g}) due to the ligand field effects which arises mainly from the strong electrostatic Coulomb repulsion of the negatively charged electrons in the oxygen orbitals (shown in Fig. 2-6) [17-20].

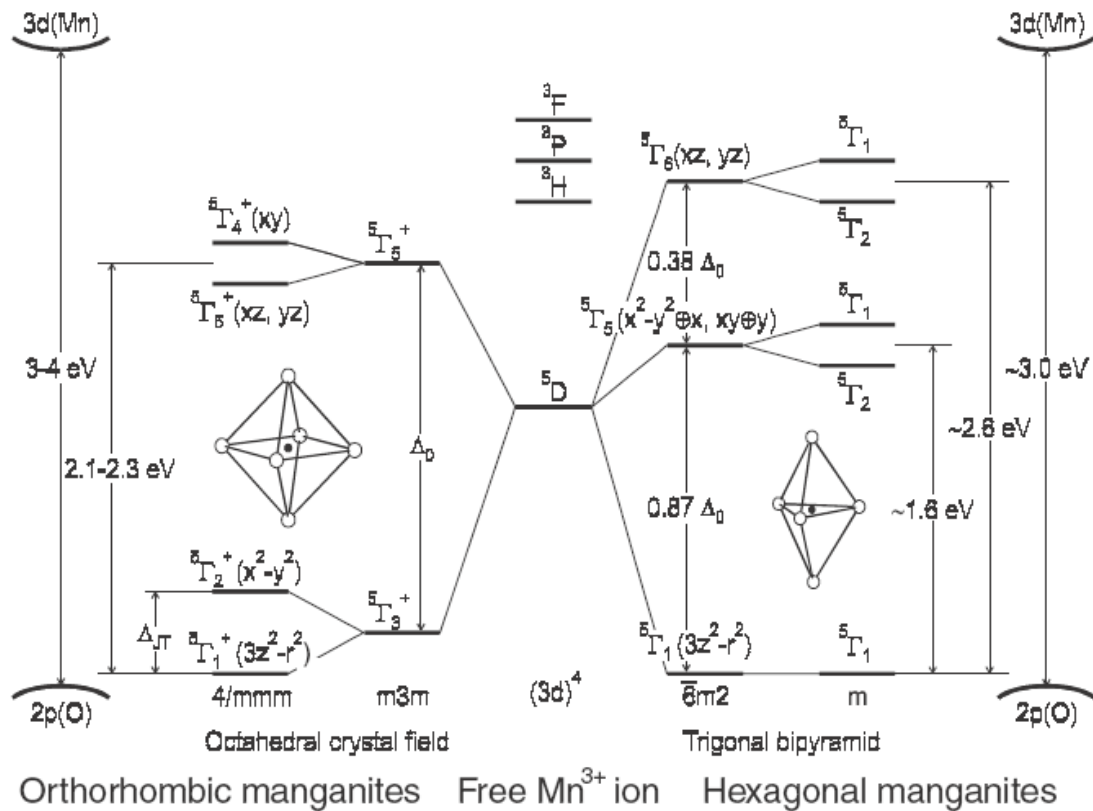


Figure 2-6: The electric structures of MnO_5 and MnO_6 [20].

The electric structures of h - $HoMnO_3$ can be simulated by the first-principles calculations since its structural parameters have been sufficiently studied. To deal with the effects of strong Coulomb interactions among $3d$ electrons, one can use the local density approximation (LDA) + U methods based on the density functional theory, as implemented in a linear combination of localized pseudo atomic orbital (LCPAO) code. Fig. 2-7 shows the density of states for hexagonal $YMnO_3$ calculated by Choi *et al.* [16].

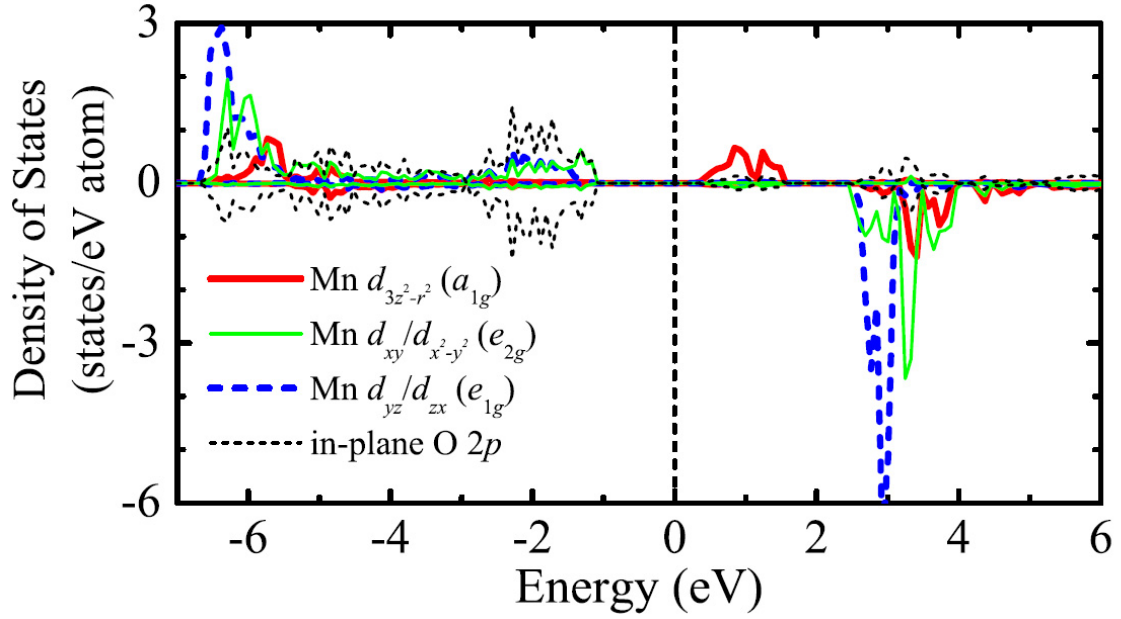


Figure 2-7: The orbital-resolved densities of states of Mn 3d orbitals and the in-plane O 2p orbital for $YMnO_3$ [16].

2.2 Femtosecond time-resolved systems

In this section, we are going to introduce the optical systems used in this study which were built by ourselves. This measuring system has three parts which can be operated individually. The first part (subsection 2.2.1) is a pump-probe system. The second part (subsection 2.2.2) is a terahertz time-domain spectroscopy system. The final part (subsection 2.2.3) is a whole system combining the first and second parts, so-called optical pump terahertz probe system. In the following subsections in this dissertation will exhibit various systems respectively. In this section we only discuss the optical apparatus among these systems. On the contrary, the principles of operation will be discussed in chapter 3.

2.2.1 The polarized femtosecond pump-probe system

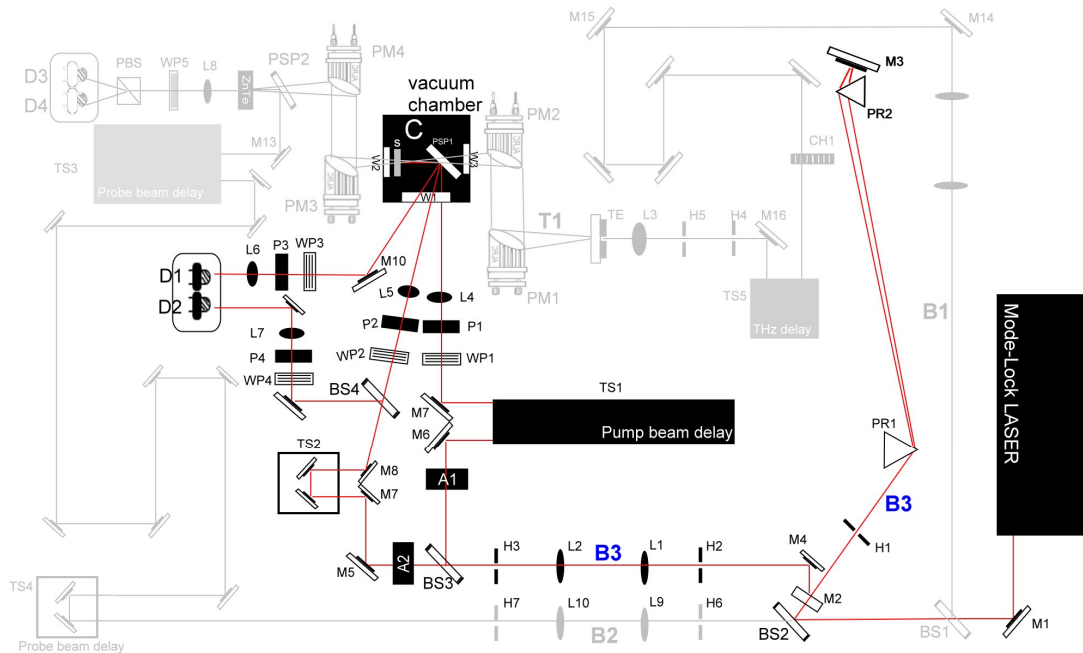


Figure 2-8: The experimental setup for near-IR pump-probe spectroscopy. Code : BS: beamsplitter, L: lens, A: acousto-optic modulator (AOM), M: mirror, WP: wave plate, P: polarizer, TS: time-delay stage, D: photodiode.

Figure 2-8 shows the details of the optical pump-probe system used in this study. The experiments were performed with a femtosecond Ti:sapphire laser pumped by an Nd:YAG laser with 532 nm. Fig. 2-9 shows the laser system which is a Ti:sapphire oscillator (Model: Mira-10) fabricated by “Coherent in USA”. The output laser is wavelength tunable from 815 nm to 740 nm via controlling the interval of the slit. The output spectrum can be measured by a spectrometer (Ocean optics, Model: USB4000-UV-VIS) as shown in Fig. 2-10. The spectral width of the output pulses was adjusted to ~ 25 nm (FWHM) for our measurements. Following, the output laser beam went through a beamsplitter (BS1) and was reflected 50 % of light as a pump beam (B1) used to generate the terahertz beam, whereas the remnant (B2) was transmitted and served as a probe which was used to probe the terahertz pulse. Moreover, the pump and probe beams used to do pump-probe experiments were taken from B2 and divided

into B3 via a beamsplitter (BS2). The laser beam B3 passed through a prism pair in order to compensate the dispersion due to the optical components in the system. Both pump and probe beams passed through two acousto-optic modulators (AOM, A1-A2) respectively. However, only one in the pump beam was driven by the RF driver and modulated the pump beam at 1 MHz. After travelling through a delay stage (TS1), a half-wave ($\lambda/2$) plate (WP1-WP2), and a polarizer (P1-P2), the pump beam was focused by a 200-mm lens on the surface of a sample with $\sim 200 \mu\text{m}$ in diameter. The $\lambda/2$ plate and polarizer allowed us to adjust the intensity and polarization (electric field, E) of pump beam (both needed for intensity control). A mechanical delay stage was used to vary the arrival time of pump pulses related to probe pulses at the position of samples. On the other hand, the probe beam only passed through the $\lambda/2$ plate and the polarizer after the AOM and focus on the surface of the sample with $150 \mu\text{m}$ in diameter by a 150-mm lens.

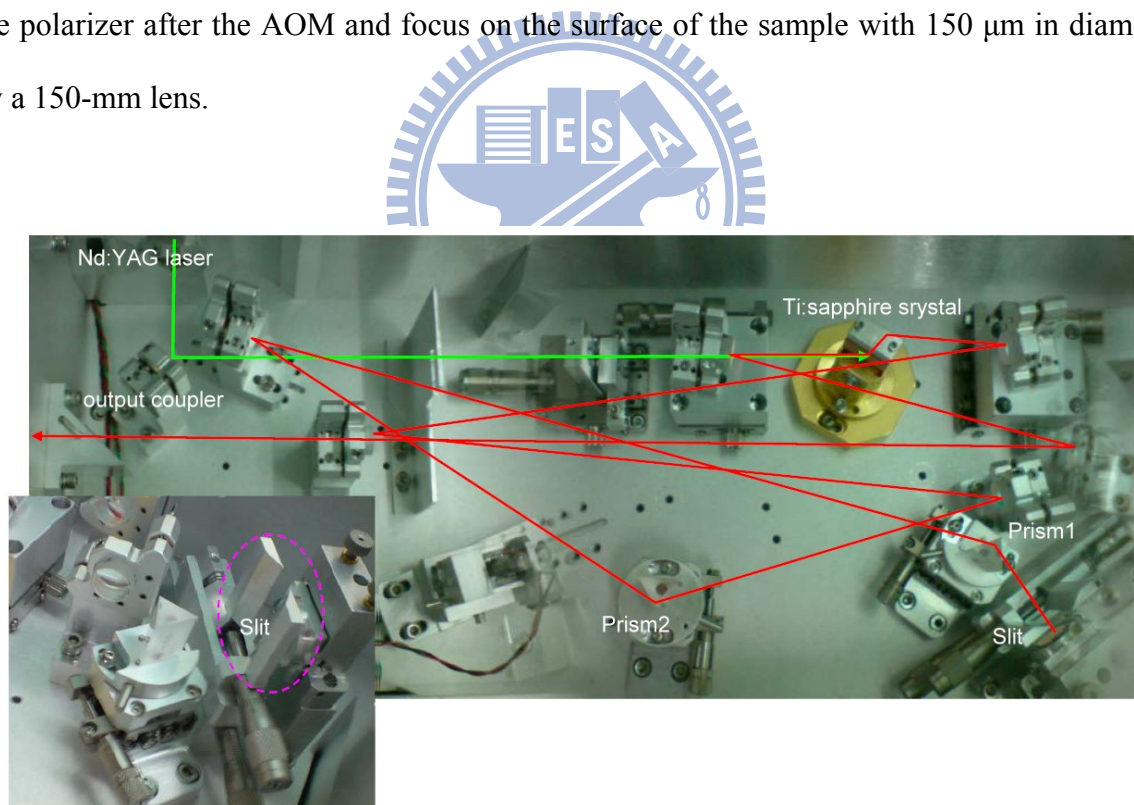


Figure 2-9: The Ti:sapphire laser cavity. The green line represents the pumping source. The red line represents the path of ultrashort pulses.

The powers of pump and probe beams were 50 mW and 2 mW, respectively. The best spatial overlap of pump and probe beams on the samples was realized by monitoring with a CCD

camera. The reflectivity changes of a probe beam were detected by using a photodiode detector and a lock-in amplifier [21-23].

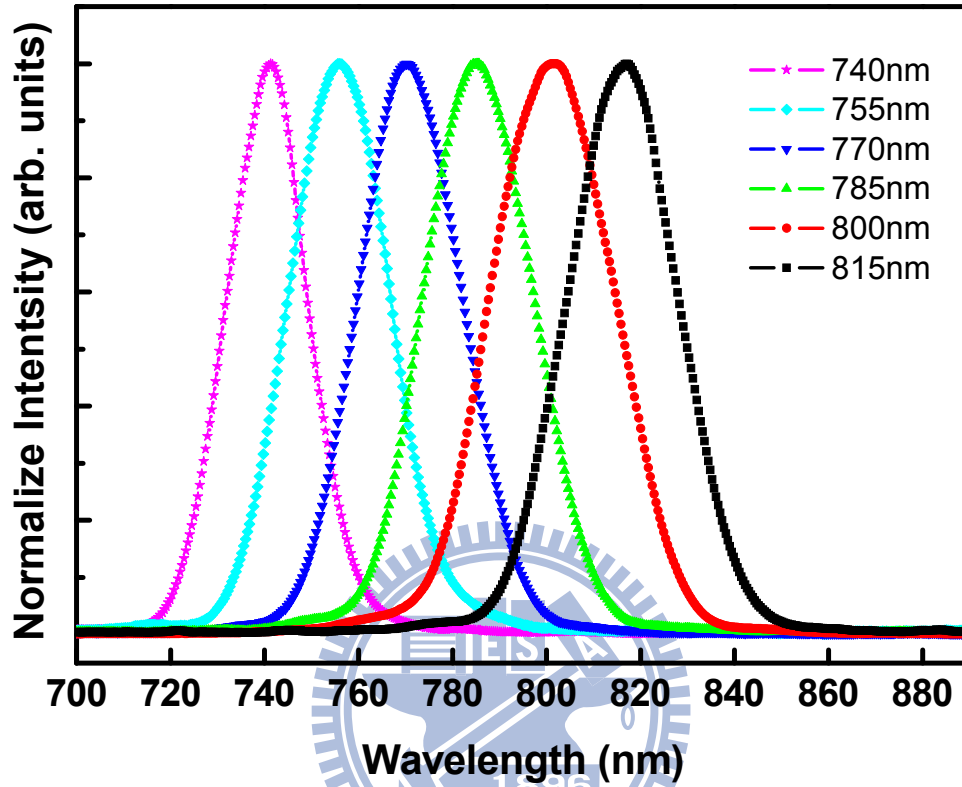


Figure 2-10: *The tunable wavelengths from 815 nm (1.52 eV) to 740 nm (1.68 eV) in the Ti:sapphire oscillator used in this study.*

2.2.2 The terahertz time-domain spectroscopy

In past 20 years, the femtosecond excitation on photoconducting switches, unbiased and biased semiconductor surface, and strain layer heterostructures have been used to generate pulsed THz electromagnetic waves [24-29]. The THz waves can be collimated and transmitted over reasonable distances, and can be detected by using optically-gated photoconductive antennas. By adjusting the delay between the THz signal and the gating pulse, the amplitude and phase of the THz signals can be obtained.

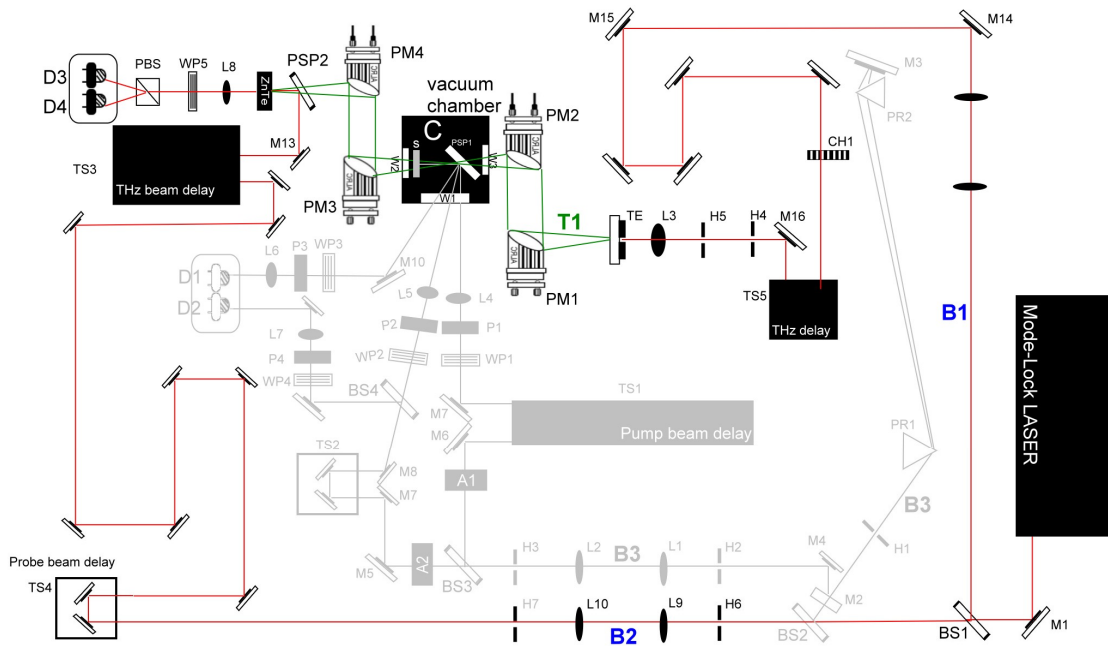


Figure 2-11: *The experimental setup for the terahertz time-domain spectroscopy. Code: BS: beamsplitter, L: lens, CH: chopper, M: mirror, TS: time-delay stage, TE: THz emitter, PM: parabolical mirror, WP: wave plate, PB: polarized beamsplitter, D: photodiode.*

Figure 2-11 shows the optical setup of the THz time-domain system. In this system, the light source divided into two parts via beamsplitter (BS1), the first one was used to generate THz radiation (B1) called THz pump beam, and another was used to be the gating pulse called THz probe beam (B2). The optical pulses (B1) were normally incident to the terahertz emitter (TE) which was manufactured by low-temperature growth GaAs or InP. The THz pump beam was modulated by a mechanical chopper (CH1) operated at 1.3 kHz. The electric field of a terahertz pulse was sampled by scanning the delay (TS4) between the pump and probe pulses. A semiconductor GaAs photoconductive emitter was triggered by femtosecond laser pulses and radiated the THz pulses. The emitted THz pulses was collimated by two pairs of off-axis parabolical mirrors (PM1-PM4) and focused onto a nonlinear ZnTe electrooptical crystal. A pellicle beamsplitter (PSP2) which is transparent for the terahertz beam was used to reflect

80% of the synchronized optical probe beam. The polarized THz wave and probe beam were collinearly aligned to a $\langle 110 \rangle$ -oriented ZnTe crystal. Then, we used a quarter-wave plate (WP5) to add a $\pi/2$ optical bias in the probe beam, which allows the system to operate in the linear range. A Wollaston polarizer beamsplitter (PBS) was used to convert the terahertz-field-induced phase retardation of the probe beam into an intensity modulation between the two orthogonal linear-polarized beams. The optical intensity modulation was detected by using two balanced photodiodes (D3, D4) and a lock-in amplifier (SR830).

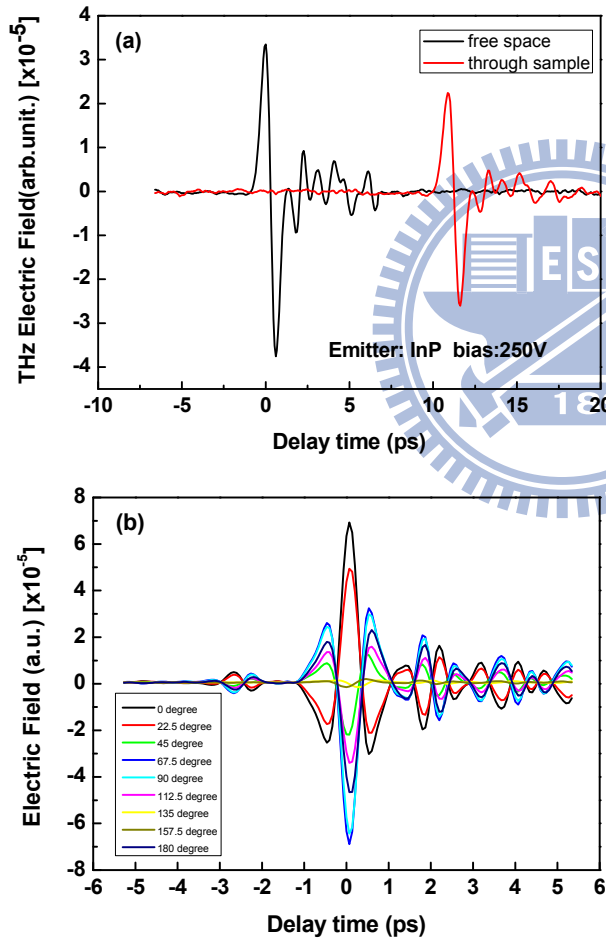


Figure 2-12: (a) The transient terahertz waveforms generation from the semiconductor InP photoconductive antenna. Black line represents the THz radiation through the free space. Red line shows the THz wave through the quartz window. (b) The terahertz emitter was changed from a photoconductive antenna to a ZnTe crystal. The terahertz wave was generated from nonlinear mechanism which is called the optical rectification.

2.2.3 The optical pump-terahertz probe system setup

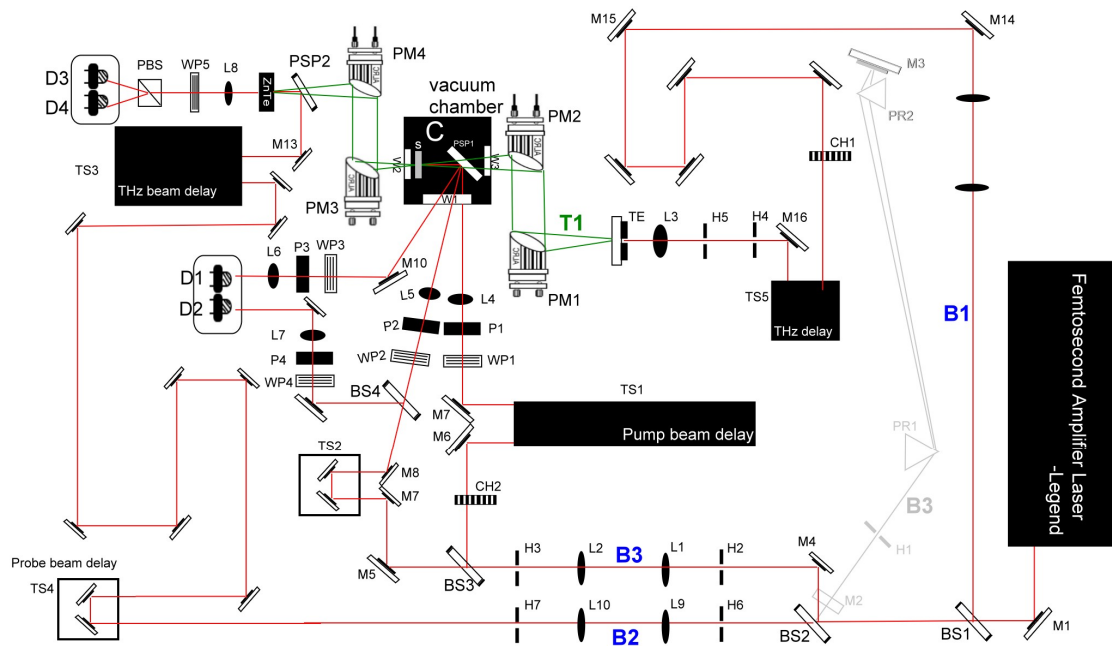


Figure 2-13: Schematic of optical pump-THz probe experiment.

The optical pump-THz probe system was performed by combined the optical pump-probe system and THz time domain system. In order to generate THz by nonlinear effect, we change the laser source from the Ti:sapphire oscillator to amplifier (Model: Coherent, Legend). The high peak power of Ti:sapphire femtosecond amplifier allows for the nonlinear optical conversion of the fundamental wavelength of 800 nm to the wavelengths of ultraviolet or infrared (THz). In fact, the combination of an optical pump with THz probe has been used to investigate the relaxation dynamics of photoexcited carriers in a lot of materials, such as superconductors [30], semiconductors [31-34], dielectrics [35], and liquids [36-37]. A diagram of the optical pump-THz probe experimental setup is shown in Fig. 2-13. The primary light source is a Ti:sapphire regenerative amplifier, which typically produces sub-100 fs (FWHM) and 800 nm pulses at a 5 kHz repetition rate. The pulses from amplifier laser pass through all kinds of optical components as mentioned in above subsections. It should be

emphasized some differences between pump-probe system and THz time domain system. One is the amplifier laser pulses without the dispersion compensation because the low frequency modulation by a mechanical chopper (CH2) instead of an AMO. Another one is the generation of THz radiation from an emitter (TE) of a ZnTe crystal instead of a semiconductor antenna in order to get higher power THz radiation.

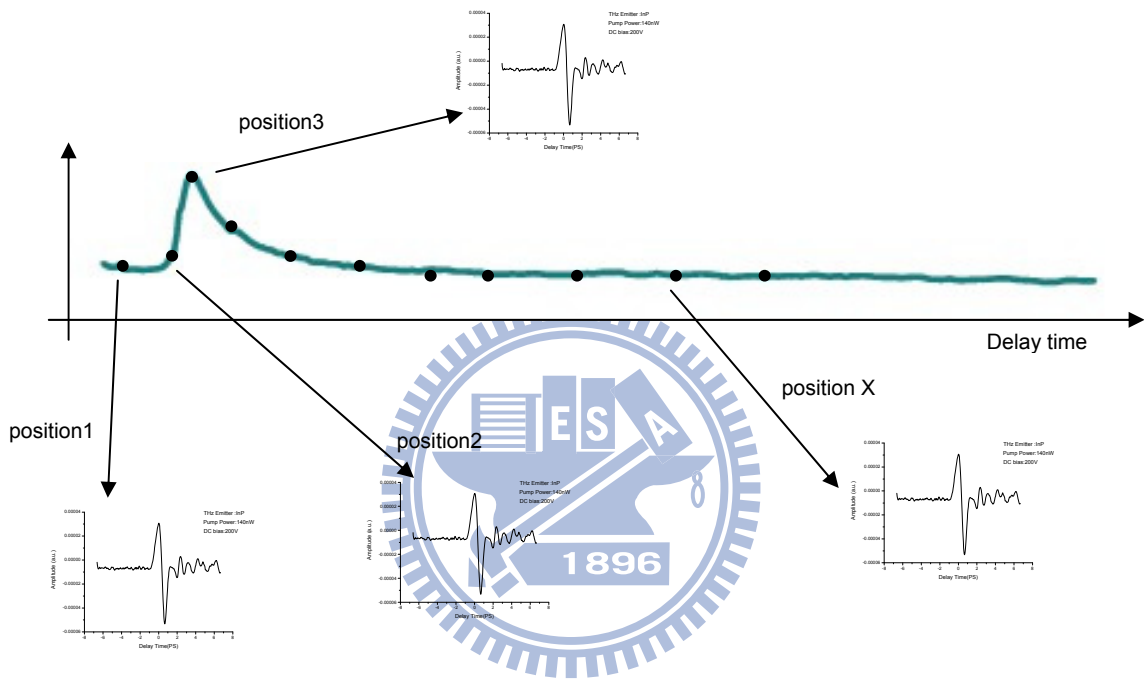


Figure 2-14: *The concepts of for the optical pump-THz probe measurements.*

The Fig. 2-14 shows the concepts of optical pump-THz probe measurements. The black circles represent the arrival time of a pump pulse at the sample surface. The curve shown in Fig. 2-14 represents the reflectivity changes induced by a pump pulse as increasing the delay time. We can measure the THz waveform with changing the delay time of a pump pulse. Thus, the variation of the dielectric function after pump excitation can be obtained. In general, we can obtain the transient information about the carrier dynamics induced by pump laser. The time-resolved transient dielectric function allows someone to know the behavior of electrons

or lattice in one material. Fig. 2-15 shows an example, the results of optical pump-THz probe experiments in semiconductor InP. The peak amplitude of THz pulses plotted as a function of delay time of pump pulses. The excitation of pump laser causes the changes of refractive index and thus causes the changes in THz transmittance [38-41].

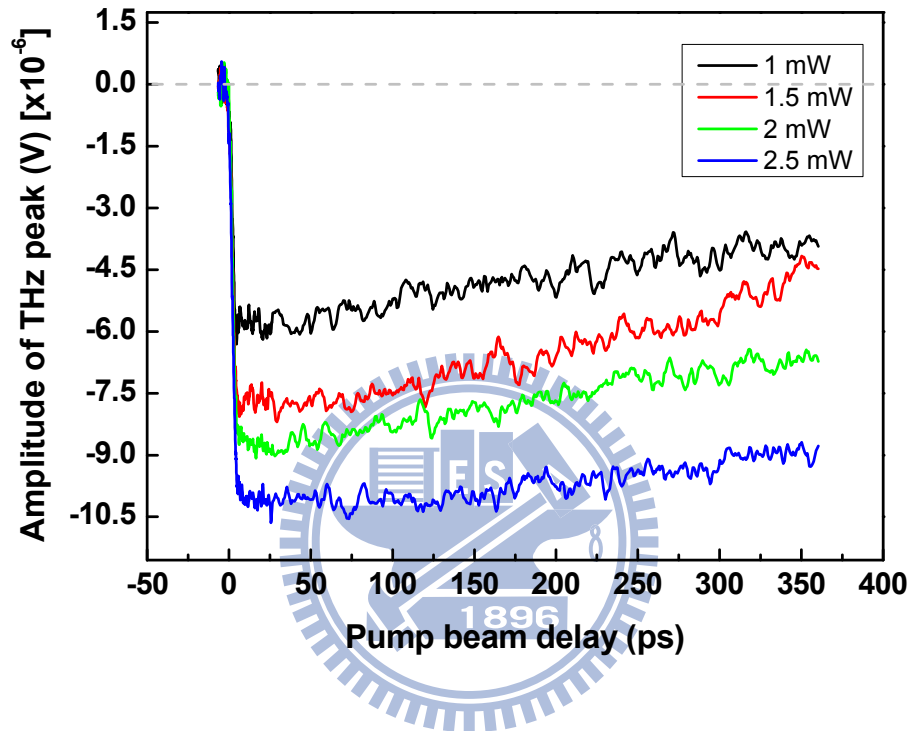


Figure 2-15: The peak amplitude of THz radiation as a function of the delay time of a optical pump pulse at various optical pump power.

Figure 2-16 shows the experimental setup. The experimental apparatus includes the optical cryostat for measuring temperature-dependent optical spectra.

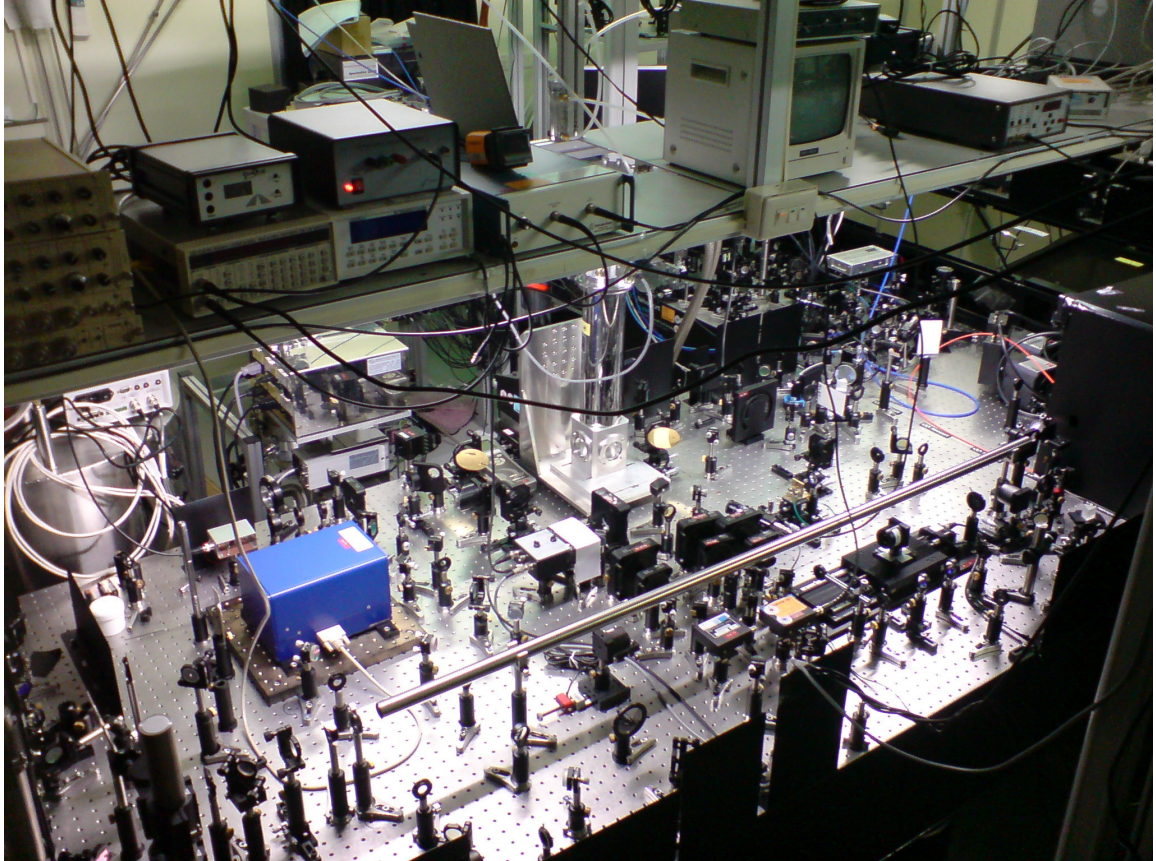


Figure 2-16: *The experimental apparatus including the optical cryostat for measuring temperature-dependent optical spectra.*

References

- [1] B. Lorenz, F. Yen, M. M. Gospodinov, and C. W. Chu, *Phys. Rev. B* **71**, 014438 (2005).
- [2] E. Galstyan, B. Lorenz, K. S. Martirosyan, F. Yen, Y. Y. Sun, M. M. Gospodinov, and C. W. Chu, *J. Phys.: Condens. Matter* **20**, 325241 (2008).
- [3] A. P. Litvinchuk, M. N. Iliev, V. N. Popov, and M. M. Gospodinov, *J. Phys.: Condens. Matter* **16**, 809 (2004).
- [4] P. Murugavel, J.-H. Lee, D. Lee, T. W. Noh, Younghun Jo, Myung-Hwa Jung, Yoon Seok Oh, and Kee Hoon Kim, *Appl. Phys. Lett.* **90**, 142902 (2007).
- [5] J.-W. Kim, K. Nenkov, L. Schultz, and K. Dörr, *J. Magn. Magn. Mater.* **321**, 1727 (2009).
- [6] J.-W. Kim, L. Schultz, K. Dörr, B. B. Van Aken, and M. Fiebig, *Appl. Phys. Lett.* **90**, 012502 (2007).
- [7] N. N. Loshkareva, A. S. Moskvina, and A. M. Balbashov, *Physics of the Solid State* **51**, 930 (2009).
- [8] A. Muñoz, J. A. Alonso, M. J. Martínez-Lope, M. T. Casáis, J. L. Martínez, and M. T. Fernández-Díaz, *Chem. Mater.* **13**, 1497 (2001).
- [9] B. Lorenz, A. P. Litvinchuk, M. M. Gospodinov, and C. W. Chu, *Phys. Rev. Lett.* **92**, 087204 (2004).
- [10] O. P. Vajk, M. Kenzelmann, J. W. Lynn, S. B. Kim, and S.-W. Cheong, *J. Appl. Phys.* **99**, 08E301 (2006).
- [11] M. Fiebig, D. Fröhlich, T. Lottermoser, and K. Kohn, *Appl. Phys. Lett.* **77**, 4401 (2000).
- [12] M. Fiebig, D. Fröhlich, T. Lottermoser, and M. Maat, *Phys. Rev. B* **66**, 144102 (2002).
- [13] A. B. Souchkov, J. R. Simpson, M. Quijada, H. Ishibashi, N. Hur, J. S. Ahn, S. W. Cheong, A. J. Millis, and H. D. Drew, *Phys. Rev. Lett.* **91**, 027203 (2003).
- [14] R. C. Rai, J. Cao, J. L. Musfeldt, S. B. Kim, S.-W. Cheong, and X. Wei, *Phys. Rev. B* **75**, 184414 (2007).

- [15] Woo Seok Choi, Soon Jae Moon, Sung Seok A. Seo, Daesu Lee, Jung Hyuk Lee, Pattukkannu Murugavel, Tae Won Noh, and Yun Sang Lee, Phys. Rev. B **78**, 054440 (2008).
- [16] Woo Seok Choi, Dong Geun Kim, Sung Seok A. Seo, Soon Jae Moon, Daesu Lee, Jung Hyuk Lee, Ho Sik Lee, Deok-Yong Cho, Yun Sang Lee, Pattukkannu Murugavel, Jaejun Yu, and Tae W. Noh, Phys. Rev. B **77**, 045137 (2008).
- [17] Deok-Yong Cho, S.-J. Oh, Dong Geun Kim, A. Tanaka, and J.-H. Park, Phys. Rev. B **79**, 035116 (2009).
- [18] H. C. Shih, T. H. Lin, C. W. Luo, K. H. Wu, J.-Y. Lin, J. Y. Juang, T. M. Uen, J. M. Lee, J. M. Chen, and T. Kobayashi, Phys. Rev. B **80**, 024427 (2009).
- [19] C.-Y. Ren, Phys. Rev. B **79**, 125113 (2009).
- [20] C. Degenhardt, M. Fiebig, D. Fröhlich, Th. Lottermoser, and R. V. Pisarev, Appl. Phys. B **73**, 139 (2001).
- [21] C. W. Luo, “Anisotropic Ultrafast Dynamics in $\text{YBa}_2\text{Cu}_3\text{O}_{7-\delta}$ Probed by Polarized Femtosecond Spectroscopy,” Doctoral thesis, National Chiao Tung University, Taiwan, (2003).
- [22] J.-C. Diels, and W. Rudolph, “Ultrashort Laser Pulse Phenomena”, Academic Press (1996).
- [23] J. Shah, M. Cardona, P. Fulde, K. V. Klitzing, and H. J. Queisser, “Ultrafast spectroscopy of semiconductors and semiconductor nanostructures”, second enlarged edition, Springer, (1996).
- [24] D. H. Auston and M. C. Nuss, IEEE J. QE-**24**, 184 (1988).
- [25] X.-C. Zhang, X. F. Ma, Y. Jin, T. -M. Lu, E. P. Boden, P. D. Phelps, K. R. Stewart, and C. P. Yakymyshen, Appl. Phys. Lett. **61**, 3080 (1993).
- [26] C. H. Fittinger and D. Grischkowsky, Appl. Phys. Lett. **54**, 490 (1989).

- [27] X.-C. Zhang, B. B. Hu, J. T. Darrow, and D. H. Auston, *Appl. Phys. Lett.* **56**, 1011 (1990).
- [28] B. B. Hu, J. T. Darrow, X.-C. Zhang, D. H. Auston, and P. R. Smith, *Appl. Phys. Lett.* **56**, 886 (1990).
- [29] X.-C. Zhang, B. B. Hu, S. H. Xin, and D. H. Auston, *Appl. Phys. Lett.* **57**, 753 (1990).
- [30] H. Wals, P. Seidel, and M. Tonouchi, *Physica C* **367**, 308 (2002).
- [31] H. K. Nienhuys, and Villy sundstrom, *Appl. Phys. Lett.* **87**, 012101 (2005).
- [32] J. Zielbauer, and M. Wegener, *Appl. Phys. Lett.* **68**, 1223 (1996).
- [33] G. Segschneider, F. Jacob, T. Löffler, H. G. Roskos, S. Tautz, P. Kiesel, and G. Dohler, *Phys. Rev. B* **65**, 125205 (2002).
- [34] K. P. H. Lui, and F. A. Hegmann, *J. Appl. Phys.* **93**, 9012 (2003).
- [35] J. Shan, F. Wang, E. Knoesel, M. Bonn, and T. F. Heinz, *Phys. Rev. Lett.* **90**, 247401 (2003).
- [36] E. Knoesel, M. Bonn, J. Shan, and T. F. Heinz, *Phys. Rev. Lett.* **86**, 340 (2001).
- [37] E. Knoesel, M. Bonn, J. Shan, and T. F. Heinz, *J. Chem. Phys.* **121**, 394 (2004).
- [38] H. F. Tiedje, H. K. Haugen, and J. S. Preston, *Optics Communication* **274**, 187 (2007).
- [39] D. G. Cooke, A. N. MacDonald, A. Hryciw, A. Meldrum, J. Wang, Q. Li, and F. A. Hegmann, *J. Mater. Sci.: Mater. Electron.* **18**, 447(2007).
- [40] J. E. Pedersen, V. G. Lyssenko, J. M. Hvam, P. Uhd Jepsen, S. R. Keiding, C. B. Sørensen, and P. E. Lindelof, *Appl. Phys. Lett.* **62**, 1265 (1993).
- [41] H. Wald, P. Seidel, and M. Tonouchi, *Physica C* **367**, 308 (2002).

Chapter 3

The femtosecond pump-probe spectroscopy

Time-resolved spectroscopy is a very important and direct tool for investigating the dynamics problems. Many physical phenomena were revealed via the ultrafast pump-probe method. In previous chapter 2, we have described the characteristics of samples and the measurement systems. In this chapter, we are going to introduce the fundamental principle of pump-probe technique. First, we discuss the characteristics of femtosecond pulse laser. Next, we discuss the principle of time-resolved pump-probe spectroscopy. Finally, we focus on the physical origins of the coherent spike signals induced by two laser beam interference.

3.1 The characteristic of femtosecond pulse laser

Up to now, there are many techniques for generating the short laser pulse, such as Q-switch [1-4], active mode-locking [5-10], passive mode-locking, the hybrid mode-locking [11-12], and the self-mode-locking [13-14]. The pulse duration generated by above methods varies from nanosecond to femtosecond. In this section, we will only talk about the characteristics of the femtosecond laser pulses which was generated via self-mode-locking

method.

3.1.1 The light pulses

The plane waves are the simplest propagation solutions which are solved via the Maxwell's equations:

$$E_y = \text{Re}(E_0 e^{i(\omega t - \vec{k} \cdot \vec{r})}) \quad , \quad |\vec{k}| = \frac{\omega}{c} = \frac{2\pi}{\lambda} \quad (3.1)$$

This particular solution (3.1) describes the propagation of a transverse electric field E_y along the propagation axis at any given point x . When the monochromatic plane wave at the origin ($x = 0$), a rewriting of Eq. (3.1) is as follows, (shown in Fig. 3.1 (a))

$$E_y = \text{Re}(E_0 e^{i\omega_0 t}) \quad (3.2)$$

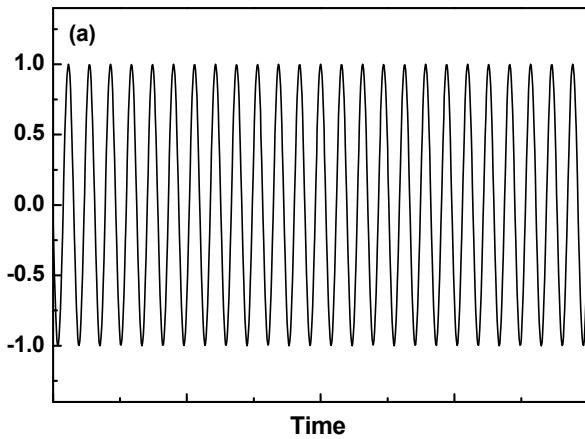
The time representation of the field is an unlimited cosine function. A light pulse can be constructed by multiplying Eq. (3.2) with a bell-shaped function. In general case, one can use a Gaussian function to produce a light pluse,

$$E_y = \text{Re}(E_0 e^{(-\Gamma t^2 + i\omega_0 t)}) \quad (3.3)$$

and its time evolution is shown in Fig. 3.2 (a). In Eq. (3.3), Γ is the shape factor of the Gaussian envelope; it is proportional to the inverse of the squared duration t_0 , i.e. $\Gamma \propto t_0^{-2}$.

There are three examples ($\Gamma = 0.5, 1.2, 4$) shown in Fig. 3.2 (a). Moreover, the spectral of a light pulse can be obtained by the Fourier transform of the time evolution function of a pulse.

Fig. 3-1(b) shows the result of a plane wave with the unique angular frequency ω_0 and its Fourier transform is a delta function $\delta(\omega_0)$. The Fourier transform of Gaussian pulse is also a Gaussian function (shown in Fig. 3-2 (b)). Thus, a light pulse must be constructed by many frequencies which are more than that of a plane wave. The numerical expression for the



F.F.T.

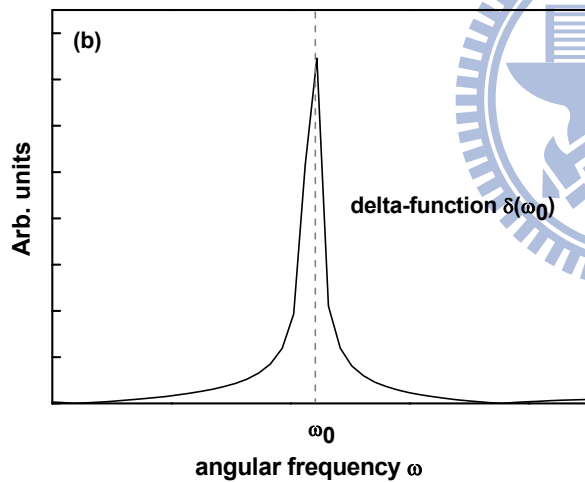
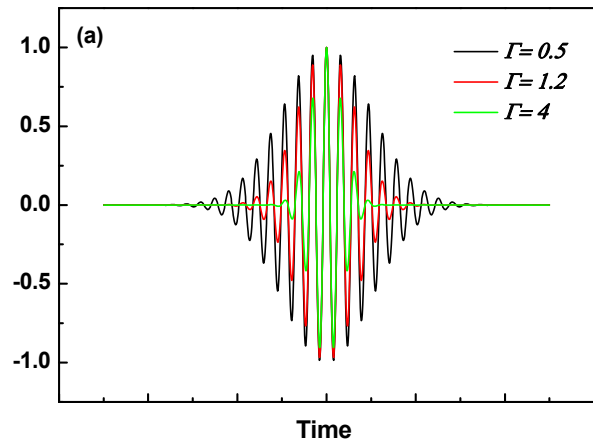


Figure 3-1: (a) Schematic time evolution of the electric field of a monochromatic plane wave. (b) The numerical Fourier transform of the cosine function. As the width of the cosine function grows larger and larger, the spectrum in frequency domain becomes a delta function with zero width.



F.F.T.

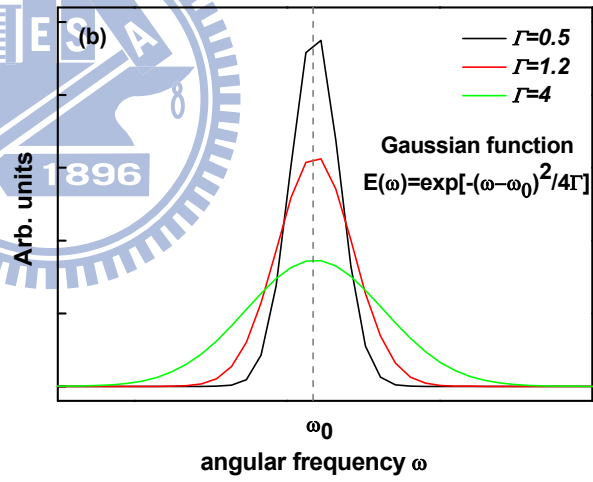


Figure 3-2: (a) Time evolution of the electric field with a Gaussian-shaped pulse. This pulse is constructed by multiplying a cosine function with a Gaussian envelope function. (b) The numerical Fourier transform of the Gaussian function. The spectrum in frequency domain is also a Gaussian function with a width which is proportional to Γ

spectrum is given in Fig. 3-2 (b) and the width of the spectrum is proportional to Γ . In other words, if the signal of Gaussian pulse in time domain is narrower, its Fourier transform spectrum is broader [15-16].

3.1.2 Method for the generation of ultrafast laser pulses

The self-mode-locking is the most popular method to generate the ultrashort laser pulses with duration as short as a few femtoseconds. The Kerr-lens mode-locking (KLM) is a method of mode-locking lasers via a nonlinear optical process known as the optical Kerr effect (self-mode-locked Ti:sapphire laser using the KLM shown in Fig. 3-3). The nonlinear properties of the amplifying medium are always very important for the locking process. The optical Kerr effect is a process which results from the nonlinear response of an optical medium to the electric field of an electromagnetic wave. The refractive index of the medium is dependent on the field strength.

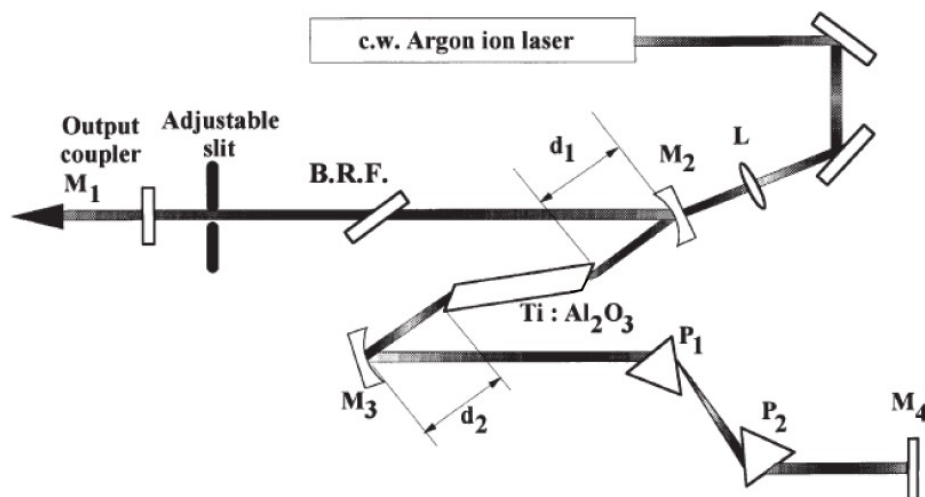


Figure 3-3: The typical cavity design of a self-mode-locked Ti:sapphire laser by using the Kerr lens mode-locking.

Because of the non-uniform power density distribution in a Gaussian beam (shown in Fig. 3-4), the refractive index changes across the beam profile; the refractive index experienced by the beam is greater in the centre of the beam. The fact that the amplifying medium is nonlinear implies that its refractive index is a function of the intensity: $n = n_0 + n_2 I$. The Gaussian wave therefore does not feel a homogeneous refractive index as it passes through the medium.

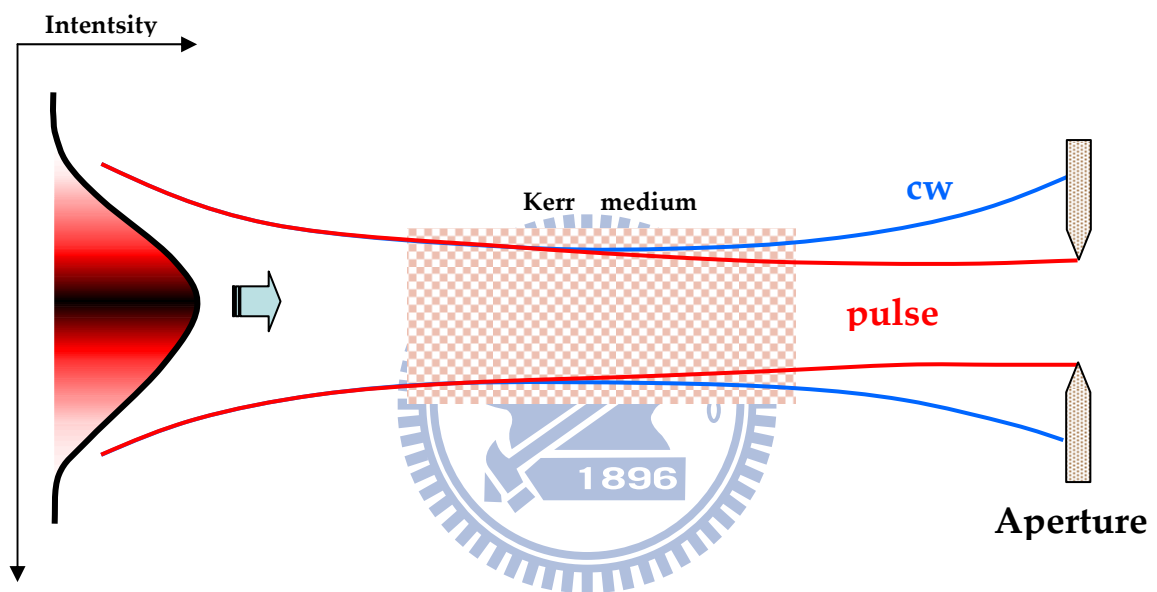


Figure 3-4: *The principle of hard aperture Kerr-lens mode-locking.*

Therefore, the amplifying medium behaves like a converging lens and focuses the beam just like a lens (Kerr lens). Following, the intensity-differentiated self-focusing associated with the natural cavity losses plays a part similar to that of the saturable absorber in the passive mode-locking method, indeed, self-mode-locking of the modes arises. A slit can be placed inside the cavity to help the self-locking process since it increases the difference between the losses undergone by the weak intensities and those undergone by the intensity maxima. Fig. 3-5 illustrates the evolution from a continuous regime to a mode-locked regime. Moreover, if one wants to start the pulsed process, one can insert a rapidly rotating optical slide

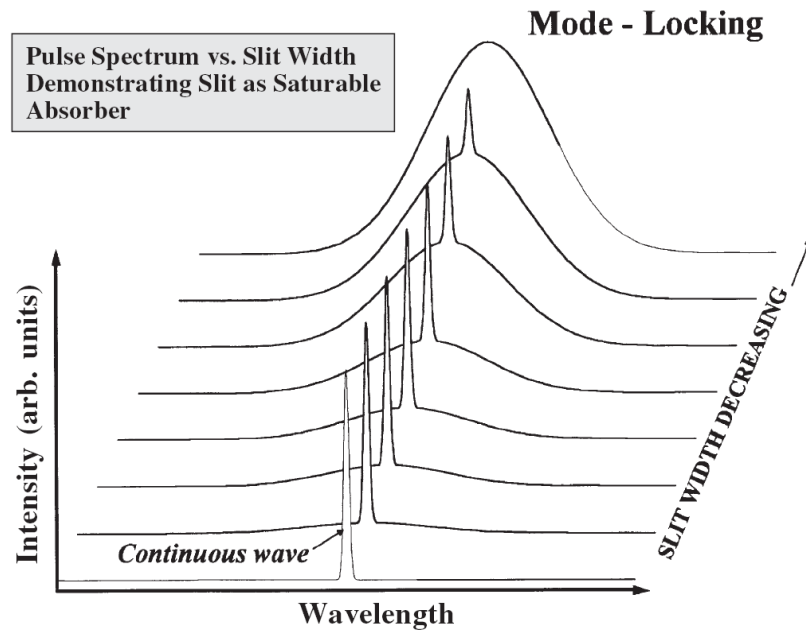


Figure 3-5: *The spectral distribution of laser output for different widths of the slit inserted in the cavity, which controls the mode-locking by the optical Kerr effect.*

to create a change in optical path, or one can simply give a quick jolt to one of the mirrors of the cavity to create an intensity pulse which triggers off the process. In a Kerr-lens mode-locked laser, the discrimination between a continuous regime and a pulsed regime is due to the self-focusing in the amplifying medium, and this discrimination becomes effective after a rapid transient change in the optical length of the cavity [15].

3.1.3 Measurement of the pulse temporal profile

The characterization of the temporal profile of the laser pulse is the basis of any laser optimization and, moreover, of any measurement in ultrashort-pulse laser techniques. In general, one can classify easily into two categories. The first one is the pure electronic method. Another is the all-optical method. The pure electronic devices only suit to the light pulses which are longer than a few hundreds of femtoseconds or picoseconds due to the limitation of

response time in instruments. As for femtosecond laser pulse, the measurement of the pulse temporal profile, in usual, needs to characterize the ultrashort pulses which is much shorter than 100 fs. Therefore, the technique we will describe here are indirect approaches, and one has not only to take into account the technique itself but also to use a model to retrieve pulse shapes from the experimental data.

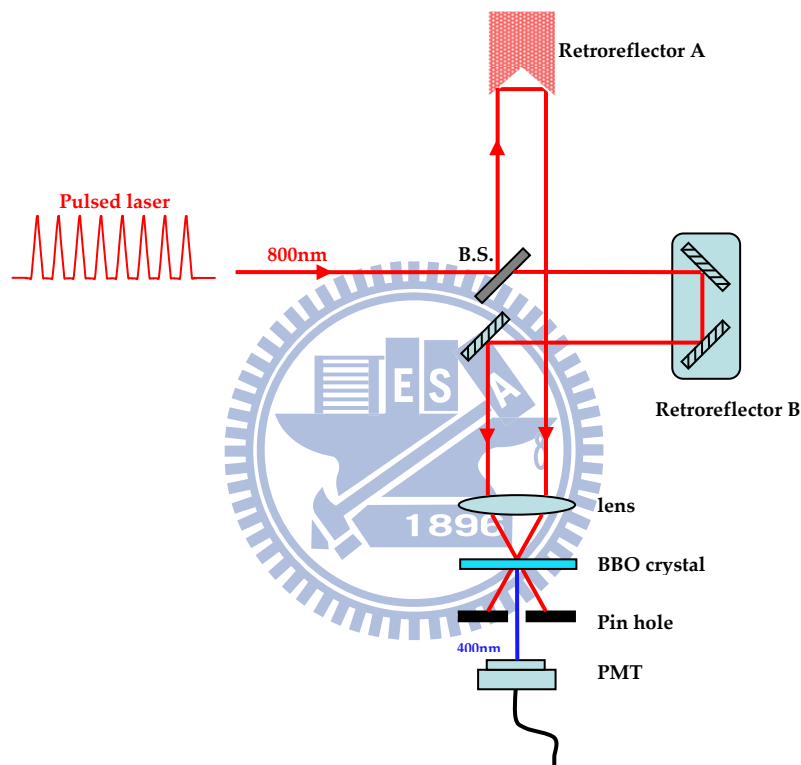


Figure 3-6: *The setup for measuring the pulse duration via the autocorrelation measurements.*

Figure 3-6 shows the experimental setup which is based on a modified Michelson interferometer. Laser pulses through 50/50 beamsplitter were divided into two parts, and then, two beams pass through two retroreflectors which are used to avoid coupling back to the laser source. The retroreflector B moves back and forth on a precise translation stage. In the non-collinear arrangement of Fig. 3-6, a reasonable peak power and a short focal length lens

require for the second-order process. Finally, we choose a nonlinear crystal (BBO) for the second harmonic generation and use a photomultiplier tube (PMT) to receive the second harmonic generation (S.H.G.) signals. Fig. 3-7 shows the result of the non-collinear autocorrelator. In our laser system, the full width at half maximum (FWHM) of the intensity autocorrelation trace is around 33 fs which was obtained by fitting the Gaussian function [15-16].

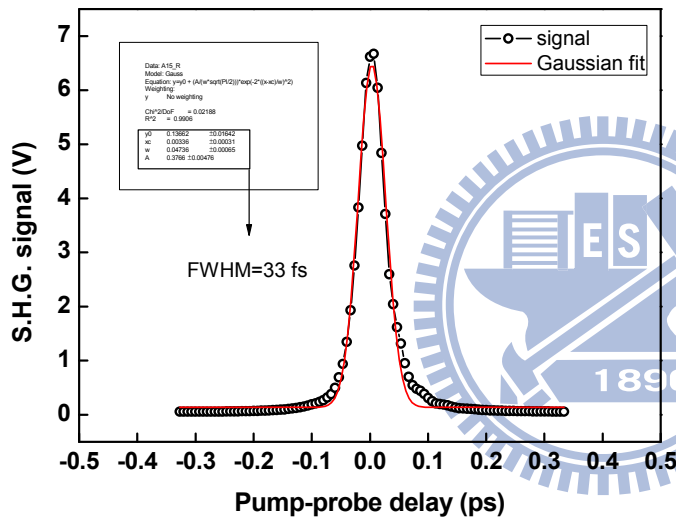


Figure 3-7: Intensity autocorrelation without background obtained by using the setup in Fig. 3-6. The pulse duration (FWHM), in our case, is around 33 fs obtained by fitting the Gaussian function.

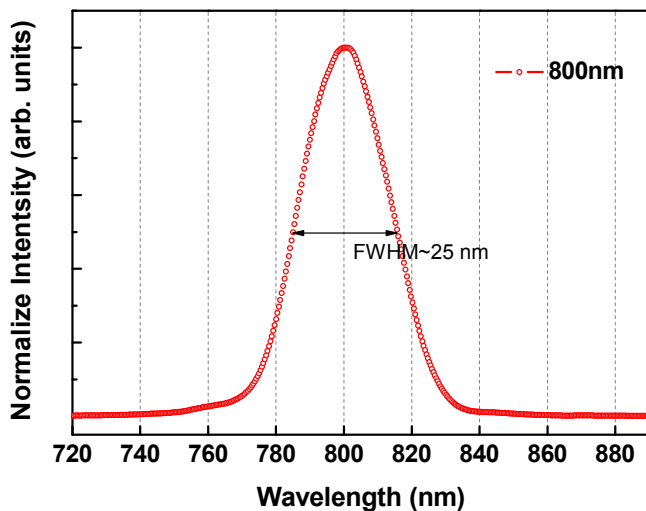


Figure 3-8: The spectrum of a laser pulse. The width of the spectrum (FWHM) is around 25 nm with center wavelength of 800 nm.

3.2 The fundamental principle of pump-probe experiments

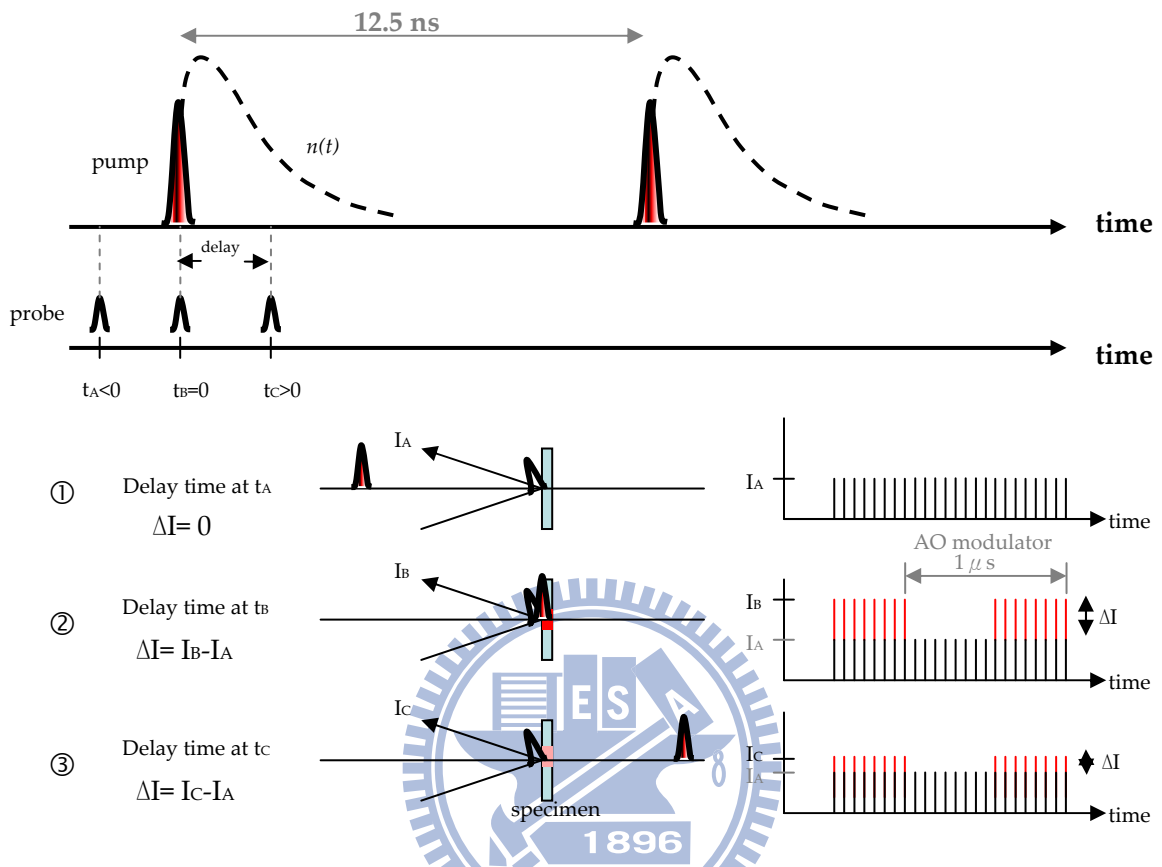


Figure 3-9: The fundamental principle of pump-probe experiments. The repetition rate of pulses is $\sim 80 \text{ MHz}$ (12.5 ns). The evolution of pump-probe processes was shown at delay time $t < 0$, $t = 0$, and $t > 0$, respectively.

In the typical pump-probe system, the probe is much weaker than the pump and the spot diameter of the probe beam at the sample is ideally considerably smaller than that of the pump beam, so that it probes a region with uniform photoexcited density. A schematic diagram of a generic setup for two-beam linear experiment is depicted in Fig. 2-8 of previous subsection 2.2.1. The principle of monitoring an ultrafast process via pump-probe experiment is illustrated in Fig. 3-9. At first, the lifetime or recovery time of the event measured by pump-probe must be less than the separating time between two pulses ($< 12.5 \text{ ns}$). In general, assuming that the $n(t)$ is the variety of reflective index which is triggered by pump pulses.

Then, the reflective intensity of probe pulses from sample will be modified by $n(t)$ during the probe pulses temporally overlapped with $n(t)$. The reflection of the probe beam was received by a balanced photo-receiver. However, usually, the variation of the reflective intensity of probe beam due to the excited-samples was very small (e.g. 10^{-6} - 10^{-8} V) and it was very difficult to detect by the photodiode directly under the noisy background such as laser noise, electric noise, and mechanical vibration. Usually the lock-in technique (also known as phase-sensitive detector) is a type of amplifier that can extract a signal with a known carrier wave [17-18]. So we must use an AOM to change the pump pulse train to be a detectable signal as a carrier wave (In order to eliminate the large noise in audio frequency, the small signal was modified at 1 MHz). Then, the probe pulse train was also modulated by the reflectivity change of the samples on a constant intensity of the probe pulse train which is a AC signal $\Delta I(t)$ with a DC signal $I_A(t)$. This signal was detected by the photodiode and sent to the lock-in amplifier, which was phase-locked to the AOM. The lock-in amplifier only extracted the AC signal $\Delta I(t)$, of which frequency was exactly equal to the modulation frequency and in-phase with the AOM. By varying the delay time (t) between pump and probe pulses, $\Delta I(t)$ would change as a function of delay time (shown in Fig. 3-9 with the cases of $t < 0$, $t = 0$, and $t > 0$). Therefore, the temporal evolution of the reflectivity change (ΔR) could be measured in the reflection-type pump-probe measurements [19].

$$\frac{\Delta R}{R} = \frac{R_{pump} - R_{without\ pump}}{R_{without\ pump}} = \frac{(I_r)_{pump} - (I_r)_{without\ pump}}{(I_r)_{without\ pump}} = \frac{\Delta I}{I_A} = \frac{\Delta I}{I_0} \quad (3.4)$$

Finally, the AC signal should be normalized by the DC component for whole curve to eliminate the zero point drift due to the long-term fluctuations of the laser output power. According to the relation shown in Eq. (3.4), thus, one could obtain the relative changes in

reflectivity $\frac{\Delta R}{R}$ by measuring the $\frac{\Delta I}{I_0}$ directly.

3.3 The coherent spike in reflection-type pump-probe

Femtosecond spectroscopy aims at characterizing the dynamics of elementary excitations in material systems. Therefore, this pump-probe technique is also of increasing interest in solid state physics, where it is used for studying metals, semiconductors, superconductors, and other materials. However, this technique gives rise to the coherent interference, i.e. the so-called coherent spike or coherent artifact, around zero delay time between pump and probe pulses. The coherent effects make data interpretation less straightforward than the incoherent picture would lead one to believe. In 1981, Vardeny and Tauc [20] first proposed that the coherent artifact mostly refers to a pump polarization coupling term appearing when pump and probe overlap, which was also confirmed by the spectral hole burning of Cruz *et al.* [21]. Then, Eichler *et al.* further explained it by diffraction from a transient grating induced by interference of the pump and probe beams [22]. They provided very important basic principles for the generation of the coherent artifact. Indeed, this coherent artifact could be found in most time-resolved spectroscopy (the transient reflectivity change $\Delta R/R$ or the transient transmissivity change $\Delta T/T$) [23-26] and disturbs the analysis of relaxation dynamics to determine the amplitude of signal near zero delay and relaxation time from the trace of $\Delta R/R$ or $\Delta T/T$. Therefore, how to unambiguously distinguish the true pump-probe signal of materials from the annoying coherent spike or obtain the coherent-spike-free pump-probe signal is indeed the key issue in the time-resolved femtosecond spectroscopy.

In order to investigate the coherent spike in the reflection-type pump-probe

measurements, we chose the popular semiconductor (100) InP as a test sample, which has been well studied in ultrafast dynamics [27]. The typical $\Delta R/R(t)$ of InP is shown in Fig. 3-10.

After the excitation of a pump pulse, the $\Delta R/R$ rapidly grows and then decays

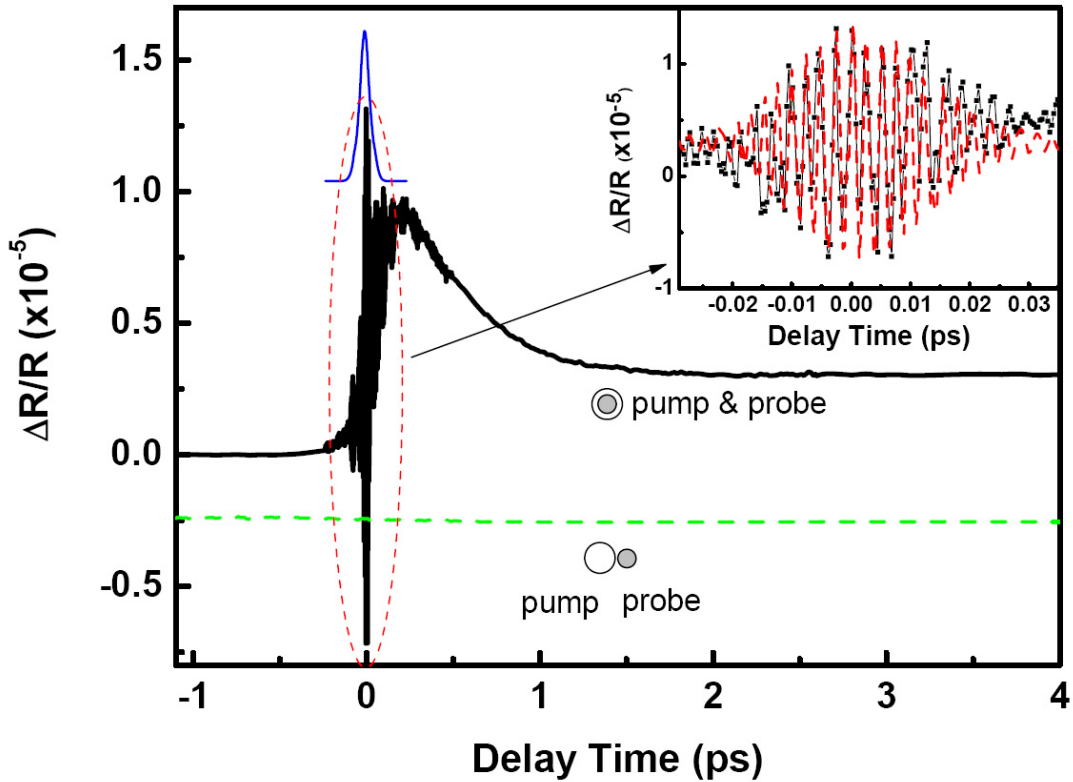


Figure 3-10: *The transient reflectivity change of InP. The thin line represents the second-order autocorrelation trace. The dashed line indicates that the transient reflectivity change under the separation of pump and probe spots on the surface of samples. The inset shows the coherent spike on an enlarged scale. The dashed line in the inset is the first-order interferometric autocorrelation trace. All of the polarization configurations are pump \perp (the polarization of pump pulses is perpendicular to the incident plan) and probe \parallel (the polarization of probe pulses is parallel to the incident plane). All of the measurements are performed at $\theta_{pump} = 1^\circ$, $\theta_{probe} = 7^\circ$, and the interval of delay time $\Delta t = 0.33$ fs.*

to a thermal equilibrium state. Besides, the most dramatic variation is the strong coherent interference (spike) around zero delay time marked by the dashed circle in Fig. 3-10. This coherent spike appears as the second-order (intensity) autocorrelation trace of pump and

probe beams. Namely, this can only be observed at the temporal overlapping region of pump and probe pulses. Through the precisely delay-time scanning with the resolution of 0.33 fs, a periodic oscillation could be clearly observed at zero delay time as shown in the inset of Fig. 3-10. Comparing with the result of the first-order interferometric autocorrelation curve (the dashed line in the inset of Fig. 3-10), which was directly measured at the position of the samples, the periodic oscillation are due to the interference between pump and probe pulses. However, under the standard pump-probe setup the detector only receives the probe pulses and no pump pulses. There are two possibilities of interfering pump pulses. One is due to scattering from the surface of the sample. The other is due to the diffraction from the transient grating in materials. The coherent spike disappears while the pump and probe spots are slightly separated in space as shown by the dashed line in Fig. 3-10. This implies that the coherent spike cannot be simply explained by the scattering due to the surface roughness.

Figure 3-11 sketches the generation of a transient grating in the reflection-type pump-probe experiments. Both pump and probe pulses with different propagation direction overlap on the surface of a sample. If the delay time between pump and probe pulses is around zero, they produce an interference pattern on the sample. The modulation of interference pattern causes a periodical change in the refractive index (phase grating) [22]. The transient grating vector is given by

$$\mathbf{k}_G = \mathbf{k}_{\text{pump}} - \mathbf{k}_{\text{probe}}, \quad (3.5)$$

where \mathbf{k}_{pump} and $\mathbf{k}_{\text{probe}}$ are the propagation vectors of pump and probe pulses, respectively. According to the grating equation:

$$d(\sin\theta_m - \sin\theta_{\text{pump}}) = m\lambda, \quad (3.6)$$

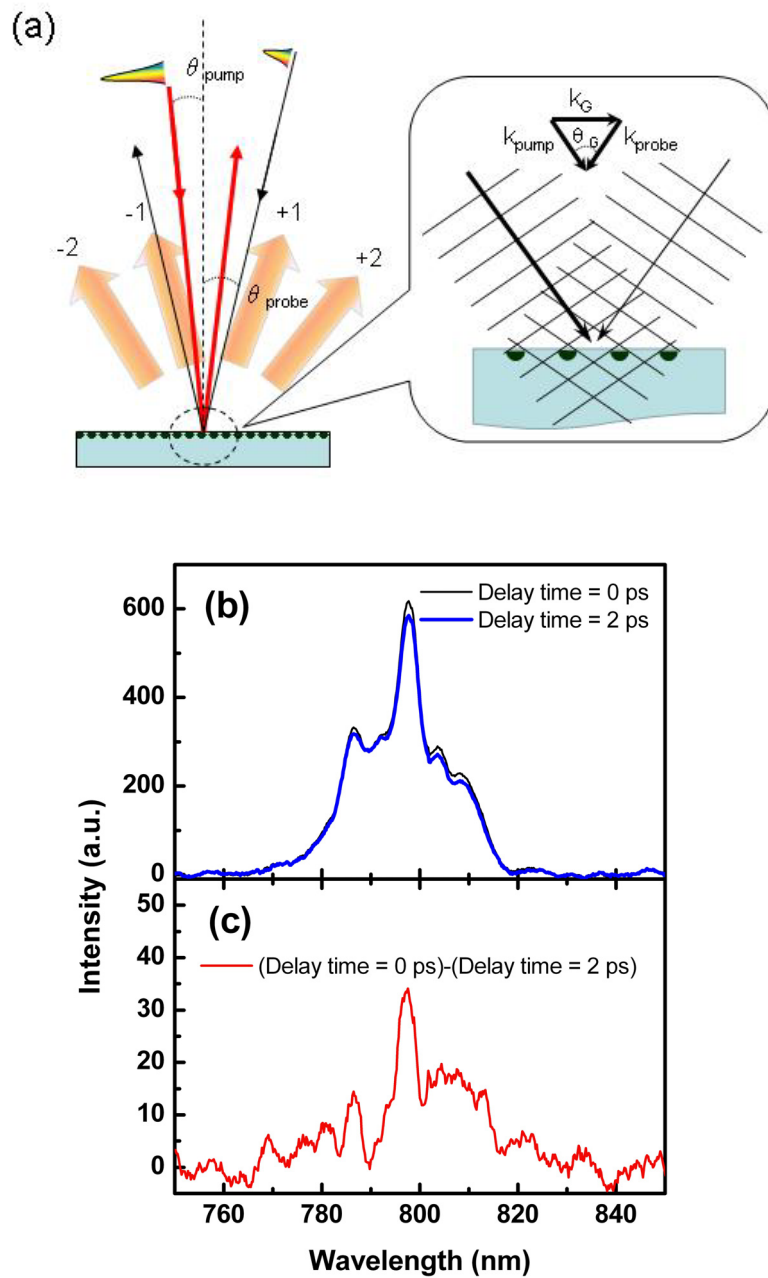


Figure 3-11: The (a) Schematics of a reflection-type pump-probe measurement and the generation of a transient grating in materials. The thick lines represent the pump beam. The thin lines represent the probe beam. The thick arrows represent the diffracted light at various orders ($m=0, +1, -1 \dots$). $\theta_G = \theta_{pump} + \theta_{probe}$ (b) The spectra measured at $\theta = 8^\circ$ (from the surface normal of samples). (c) The spectrum obtained by subtracting the spectrum with thick line from the spectrum with thin line in (b).

where $d = 2\pi / k_G$ is the period of the transient grating, θ_{pump} is the incident angle of a pump beam, m is the order of interference, and θ_m is the diffraction angle of the m -th order. The

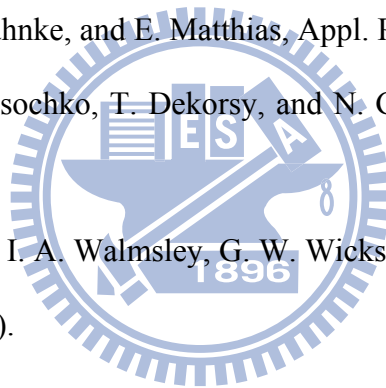
pump pulse could be diffracted by this transient grating as shown with the thick arrows in Fig. 3-11 (a). At $\theta = 8^\circ$ (from the surface normal of the sample) around $m = +1$, the spectra of the scattering light have been measured at the delay time = 0 ps and 2 ps. Fig. 3-11 (c) shows the difference between the thin line with delay time 0 ps and the thick line with delay time 2 ps in Fig. 3-11 (b). This additional spectrum around the diffractive angle with $m = +1$ indicates that the existence of the transient grating at zero delay time. Once the pump pulse is diffracted into the detector, the interference between pump pulse and probe pulse will be observed. For instance, the optical path of diffracted light with $m = -1$ is just collinear with the optical path of the probe pulses and then lead to the coherent interference around the zero delay time. This implies that the coherent spike is unambiguously caused by the diffracted light of pump pulses due to the transient grating of the samples, which is consistent with the theoretical results of Eichler *et al.* in transmission-type pump-probe experiments [22].

Generally, the coherent spike is not welcome in the pump-probe measurements. On the other hand, however, this coherent spike can give us the information for the characteristics of pulses we used. In the inset of Fig. 3-10, the oscillation of coherent spike is almost equal to the results of standard first-order autocorrelation measurements. This means that the characteristics of pulses, i.e. the coherent length or bandwidth can be directly estimated from the coherent spike.

References

- [1] J. Kleinbauer, R. Knappe, and R. Wallenstein, *Topics in Appl. Phys.* **96**, 9 (2004).
- [2] C. Wu, X. Wang, L. Cheng, and Y. Zhao, *Laser Physics* (Fudan University Press, Shanghai, China, 1989).
- [3] V. Arsenev, I. Matveev, and N. Ustinov, *Soviet Journal of Quantum Electronics* **7**, 1321 (1997).
- [4] A. Penzkofer, *Appl. Phys. B* **46**, 43 (1988).
- [5] E. Ippen, *Appl. Phys. B* **58**, 159 (1994).
- [6] P. French, *Rep. Prog. Phys.* **58**, 169 (1995).
- [7] G. P. A. Malcolm and A. I. Ferguson, *optical and Quantum Electronics* **24**, 705 (1992).
- [8] I. Tomov, R. Fedosejevs, and M. Richardson, *Soviet Journal of Quantum Electronics* **10**, 797 (1980).
- [9] L. E. Hargrove, R. L. Fork, and M. A. Pollack, *Appl. Phys. Lett.* **5**, 4 (1964).
- [10] S. E. Harris and B. J. McMurtry, *Appl. Phys. Lett.* **7**, 265 (1965).
- [11] H. A. Haus, *IEEE J. Quant. Electr.* **QE11**, 736 (1975).
- [12] J. P. Ryan, L. S. Goldberg, D. J. Bradley, *Opt. Commun.* **27**, 127 (1978).
- [13] D. E. Spence, P. N. Kean, and W. Sibbett, *Opt. Lett.* **16**, 42(1991).
- [14] U. Keller, W. H. Knose, G. W. 'tHooft, H. Roskos, T. R. Woodward, J. E. Cunningham, D. L. Sivco, and A. Y. Cho, *Adv. Sol. State Lasers* **10**, 115 (1991).
- [15] Claude Rullière, “Femtosecond Laser Pulses-principles and Experiments”, 2nd edition, Springer (2005).
- [16] J.-C. Diels and W. Rudolph, “Ultrashort Laser Pulse Phenomena”, Academic Press (1996).
- [17] P. Horowitz and W. Hill, “The art of electronics”, 2nd edition, Cambridge, New York (1989).

- [18] X. Wang, Rev. Sci. Instrum. **64**, 1999 (1990).
- [19] C. W. Luo, “Anisotropic Ultrafast Dynamics in $\text{YBa}_2\text{Cu}_3\text{O}_{7-\delta}$ Probed by Polarized Femtosecond Spectroscopy,” Doctoral thesis, National Chiao Tung University, Taiwan, (2003).
- [20] Z. Vardeny and J. Tauc, Opt. Commun. **39**, 396–400 (1981).
- [21] C. H. B. Cruz, J. P. Gordon, P. C. Becker, R. L. Fork, and C. V. Shank, IEEE J. Quantum Electron. **24**, 261–266 (1988).
- [22] H. J. Eichler, D. Langhans, and F. Massmann, Opt. Commun. **50**, 117–122 (1984).
- [23] C.-R. Wang, T. Luo, and Q.-B. Lu, Phys. Chem. Chem. Phys. **10**, 4463-4470 (2008).
- [24] C. Chudoba, E. T. J. Nibbering, and T. Elsaesser, Phys. Rev. Lett. **81**, 3010-3013 (1998).
- [25] U. Conrad, J. Gdde, V. Jhnke, and E. Matthias, Appl. Phys. B **68**, 511–517 (1999).
- [26] M. V. Lebedev, O. V. Misochko, T. Dekorsy, and N. Georgiev, J. Exp. Theoret. Phys. **100**, 272–282 (2005).
- [27] Y. Kostoulas, L. J. Waxer, I. A. Walmsley, G. W. Wicks, and P. M. Fauchet, Appl. Phys. Lett. **66**, 1821-1823 (1995).



Chapter 4

The ultrafast dynamics on *h*-HMO single crystals

In previous chapters, we introduce the properties of samples, the experimental setup, and the characteristics of ultrafast optics, respectively. Most of the discussion in this chapter will be centered around the results of the pump-probe experiments. In the first section of this chapter, we present the important results of experiments in details. The pump induced the dynamics of electrons, holes, and phonons are influenced by their interaction with each other. In section 4.2-4.4, we demonstrate and explain that the ultrafast electrons and lattice dynamics on hexagonal HoMnO_3 (*h*-HMO) single crystals. By the pump-probe experiments, we show the dynamical behavior of electrons at Néel temperature (T_N) which coupled with the antiferromagnetic (AFM) ordering. Moreover, through the ultrafast lattice dynamics we directly observed the giant and anisotropic magnetoelastic coupling at T_N on *a-b* plane and along *c*-axis. The time-resolved pump-probe method realized the complete observation of the strong correlation among electron, lattice, and spin degrees of freedom in multiferroic *h*-HMO single crystals.

4.1 The results of $\Delta R/R$ at various wavelengths and temperatures

In order to explain the physical phenomena which observe in our experimental data. In this section 4.1, we will give an account for the essential information about the transient reflectivity change $\Delta R/R$, the classification of important interactions, and the mathematical treatments in the $\Delta R/R$ curves.

4.1.1 The transient reflectivity changes $\Delta R/R$

According to the discussion in section 2.1, one knows that the temperature plays a crucial role to influence the electronic structure of *h*-HMO single crystals. Therefore, we should explore the temperature-dependent properties of samples. Moreover, it is necessary to observe the antiferromagnetic effect by using variable photon energies in our pump-probe experiments. The reasons will discuss in the following subsection. Figure 4-1(a)-(f) show the temperature-dependent $\Delta R/R$ at various wavelengths which exhibit the strong wavelength- and temperature-dependent. The temperature-dependent $\Delta R/R$ measured at various wavelengths (a) $\lambda = 740$ nm (b) $\lambda = 755$ nm (c) $\lambda = 770$ nm (d) $\lambda = 785$ nm (e) $\lambda = 800$ nm (f) $\lambda = 815$ nm, respectively. In addition, the pump-probe conditions must be controlled carefully, i.e. the laser power density of pump and probe beams will lead to the linear or nonlinear responses in the illuminated area. Fig. 4-2 (a) shows the power-dependent reflectivity change ($\Delta R/R$) at room temperature. The inset of Fig. 4-2 (a) shows the linear dependence at various pumping fluence which indicates that our experiments were performed in weak perturbation regime. Fig. 4-3(a)-(b) show the similar results with wavelength at 740 nm and room temperature.

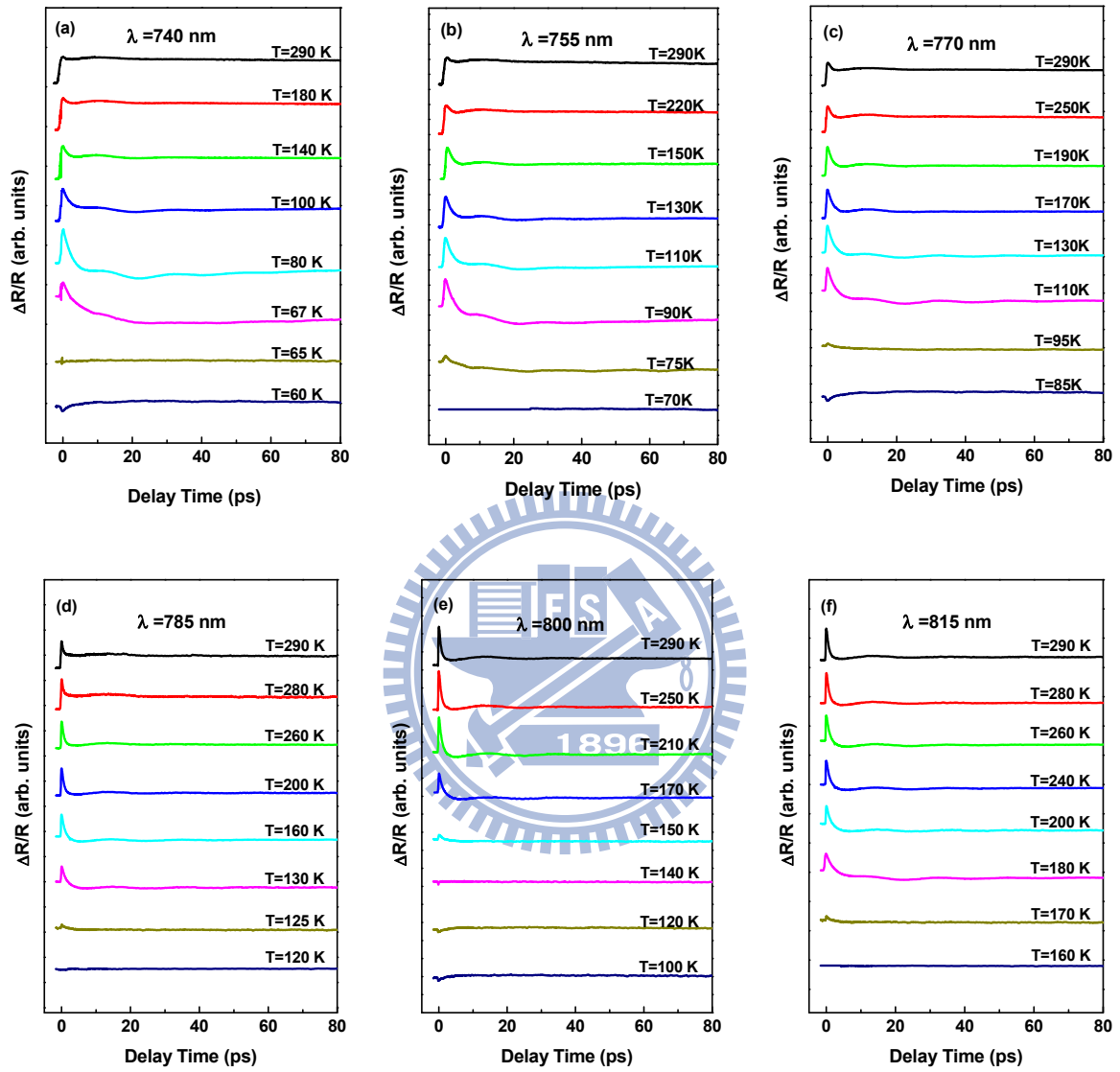


Figure 4-1: The temperature-dependent $\Delta R/R$ measured at various wavelengths (a) $\lambda = 740$ nm, (b) $\lambda = 755$ nm, (c) $\lambda = 770$ nm, (d) $\lambda = 785$ nm, (e) $\lambda = 800$ nm, (f) $\lambda = 815$ nm, respectively. The $\Delta R/R$ curves shown here are only the temperatures with important features.

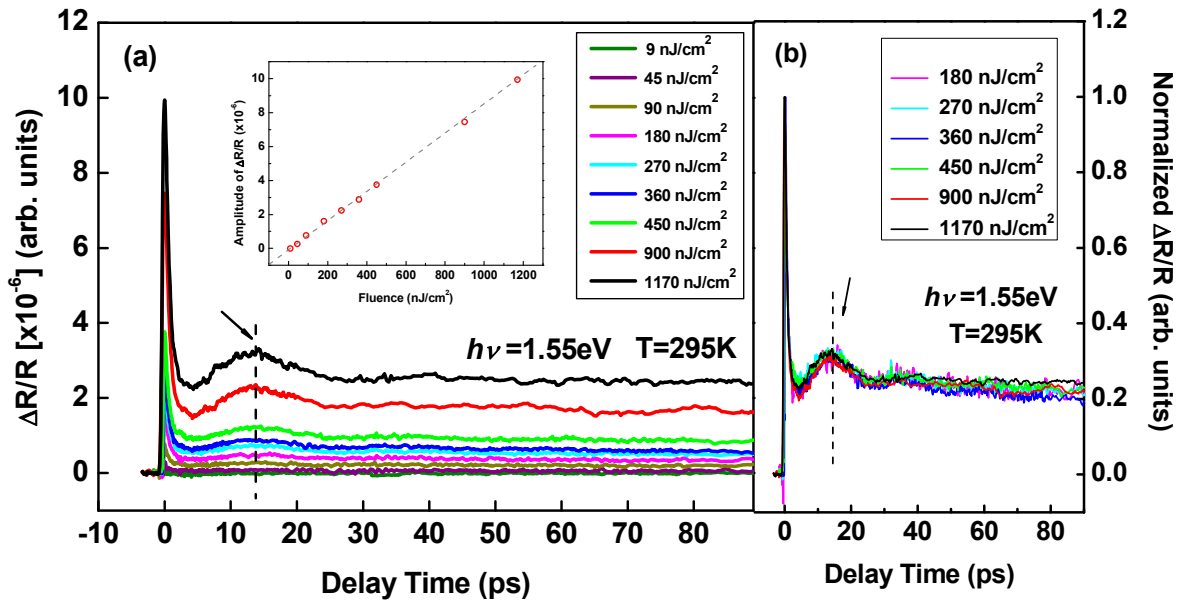


Figure 4-2: (a) The fluence-dependent reflectivity changes ($\Delta R/R$) at 800 nm. The inset shows the linear behavior. (b) The normalized $\Delta R/R$ in (a) to show the same relaxation behavior.

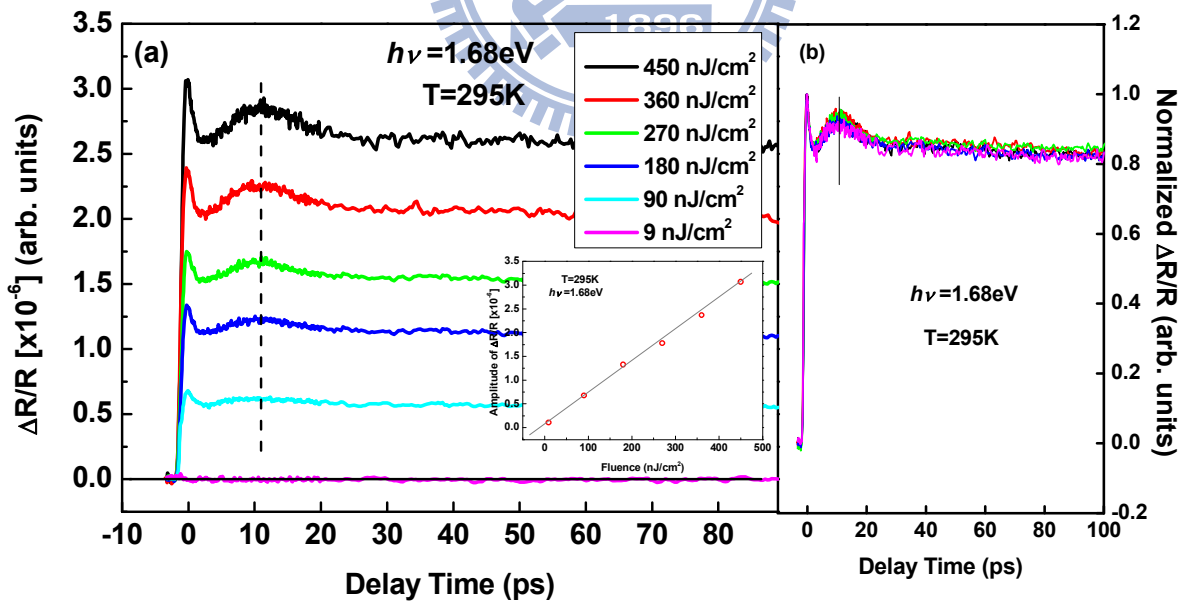


Figure 4-3: (a) The fluence-dependent reflectivity changes ($\Delta R/R$) at 800 nm. The inset shows the linear behavior. (b) The normalized $\Delta R/R$ in (a) to show the same relaxation behavior.

4.1.2 Classify the ultrafast behaviors in $\Delta R/R$ curves

Utilizing the ultrashort pulses to study the quasiparticles dynamics is an excellent method due to the femtosecond time-resolution. In general case, the pump-probe processes can be easily distinguished into two classes that is the excitation process by an ultrashort pump pulse and the processes of quasiparticles scattering (relaxation) in materials after pump excitation. Furthermore, after the excitation of optical pulses, it undergoes several stages of relaxation before it returns back the thermodynamic equilibrium. Usually, the relaxation processes is material-dependent. In our case, the carrier relaxation can be distinguished into two regimes: (I) Hot-carrier regime, (II) Isothermal regime [1-2].

(I) Hot-carrier regime: After the excitation of a material with an ultrashort laser pulse, the carrier-carrier (electron-electron) scattering is primarily responsible for redistributing the energy within the carrier system, and leads to a thermal distribution function of carriers, i.e. a distribution that can be characterized by the temperature T_e . The temperature can be, and usually is, higher than the lattice temperature T_l . Typically, the electron-electron thermalize among themselves in several hundreds of femtoseconds. After the carrier-carrier thermalization, the thermalized electrons start to transfer its energy to the lattice subsystem. This electron-phonon interaction may lead to a large population of non-equilibrium phonons. Usually, the electron-phonon interaction reaches a new equilibrium in several picoseconds to several hundreds of picoseconds.

(II) Isothermal regime: At the end of hot-carrier regime, all of the carriers, e.g. electrons and phonons, are in equilibrium which can be described by the same temperature. However, there are still excess electrons and holes compared to the thermodynamic equilibrium. These excess

electron-hole pairs (or excitons) recombine either radiatively or non-radiatively and return to the thermodynamic equilibrium.

In the case of h -HMO, the pump-probe signal can be distinguished into two processes that is the hot-excitation and the isothermal regime. However, the density of free carrier in h -HMO single crystals induced by pump is very small compared with other materials such as metal or semiconductor. Thus, the pump induced changes can be regarded as the weak perturbation. For this reason, the probability of electron-electron scattering is much smaller than the probability of electron-phonon scattering.

$$P_{-,-} = \langle n_- \rangle \langle n_- \rangle \ll P_{-,+} = \langle n_- \rangle \langle n_+ \rangle \quad (4.1)$$

In Eq. (4.1), the $P_{-,-}$ represents the probability of collision between electrons, $P_{-,+}$ represents the probability of collision between electron and phonon, $\langle n_- \rangle$ describes the concentration of pump induced free electrons, $\langle n_+ \rangle$ describes the occupancy of concentration of phonons in the environment with certain temperature which is given by Plank distribution function:

$$\langle n_+ \rangle = \frac{1}{\exp(\hbar\omega / k_B T) - 1} \quad (4.2)$$

In the condition of $\langle n_- \rangle \ll \langle n_+ \rangle$, the Eq. (4.1) shows that the probability of collision of electron-electron is much smaller than the probability of collision of electron-phonon. According to our experimental observation in $\Delta R/R$ curves, thus, we can immediately construct that there are three simple physical mechanisms occurred during the pump-probe processes. These three stages with the snapped shot of time are shown in Fig. 4-4. The first stage is described as a pump light-induced change (excitation) of the electron population in the bands. The second and third stages show that the relaxation processes of quasiparticles via the electron-phonon interaction and recombination of electron-hole pairs, respectively.

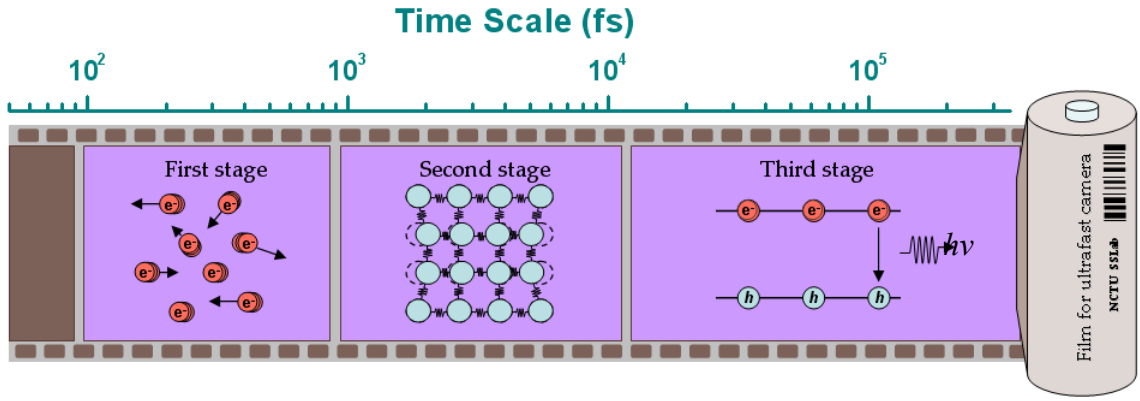


Figure 4-4: The snapped shot of *ultrafast dynamical processes in materials*. The complex correlation among charge, spin, and lattice degrees of freedom can be recognized in different characteristic time scales by the so-called *ultrafast camera*.

4.1.3 The mathematical fittings in $\Delta R/R$ curves

In this subsection, we show the mathematical method to extract the information from the relaxation part in the transient reflectivity changes (delay time $t > 0$). The fittings used here followed the physical pictures in above subsection. In principle, there are four primary features, i.e. the initial rising (excitation) component, the “negative” component, the oscillating component, and the component of recombination of electron-hole pairs which are shown in Fig 4-5 (different components are marked by arrows). The temperature-dependent and wavelength-dependent $\Delta R/R$ curves were fitted by the following equation:

$$\frac{\Delta R}{R}(t, t > 0) = A_e \exp(-t/\tau_e) + A_p (1 - \exp(-t/\tau_{p,r})) \exp(-(t - \tau_{p,0})/\tau_{p,d}) + A_n (1 - \exp(-t/\tau_{n,r})) \exp(-(t - \tau_{n,0})/\tau_{n,d}) + A_o \exp(-t/\tau_o) \cos(\omega t - \phi), \quad (4.3)$$

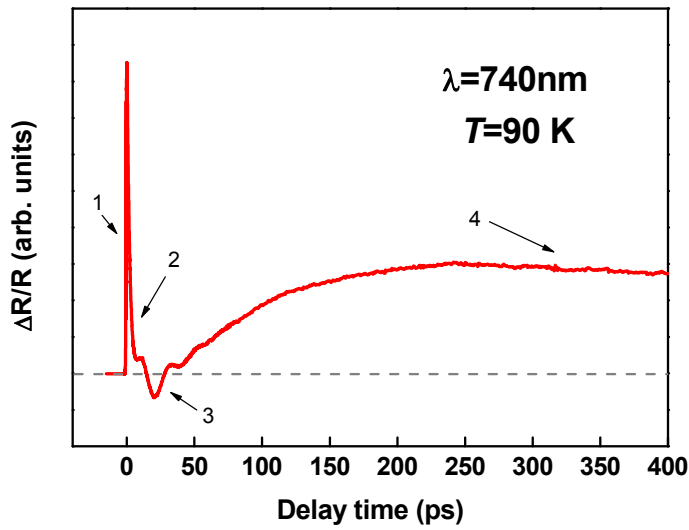


Figure 4-5: *There are four primary features in the transient reflectivity changes.*
 1. *The carrier excitation by ultrashort pulse.*
 2. *The electron-phonon interaction process induced negative component.*
 3. *The electron-phonon interaction process induced the strain pulse propagation.*
 4. *The final stage was explained by the recombination of electron-hole pairs.*

In Eq. (4.3), the first term at right-hand side of the equal mark represents the number of high-energy electrons (after pump excitation can view as quasi-particles). The second term represents the number of high-energy phonons. The third term describes the “negative” component. The final term represents the oscillation component. Fig. 4-6(a)-(c) show the mathematical fitting at the choice temperatures and wavelengths.

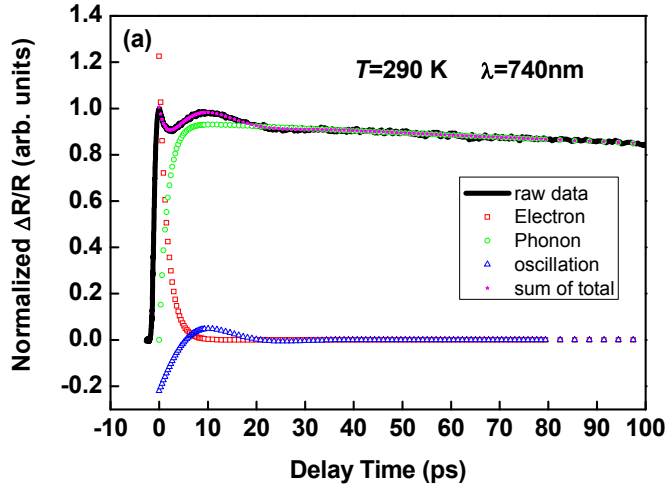


Table		T=290 K		λ =740 nm	
A_e	1.22556 (a.u.)	τ_0	7.232 (ps)		
τ_e	1.70044 (ps)	ω	0.20544 ($2\pi/s$)		
A_p	0.91896 (a.u.)	ϕ	3.58771 (a.u.)		
$\tau_{p,0}$	24.39243 (ps)	A_n	—		
$\tau_{p,d}$	940.17478 (ps)	$\tau_{n,r}$	—		
A_0	0.24328 (a.u.)	$\tau_{n,0}$	—		
		$\tau_{n,d}$	—		

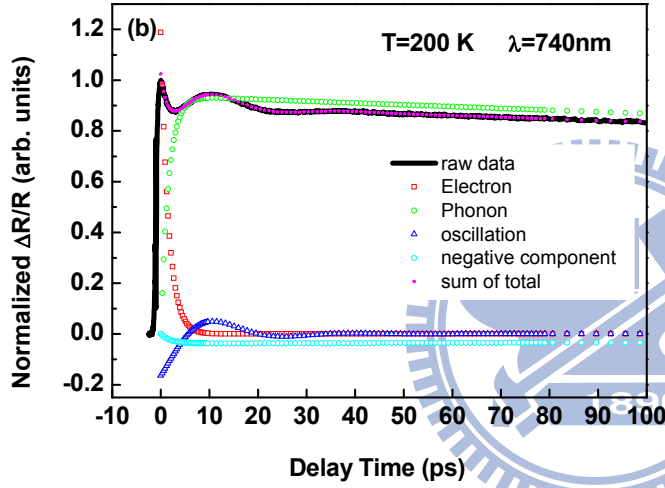


Table		T=200 K		λ =740 nm	
A_e	1.18805 (a.u.)	τ_0	9.32109 (ps)		
τ_e	1.59988 (ps)	ω	0.21774 ($2\pi/s$)		
A_p	0.92054 (a.u.)	ϕ	3.48375 (a.u.)		
$\tau_{p,0}$	24.95999 (ps)	A_n	0.03602 (a.u.)		
$\tau_{p,d}$	1279 (ps)	$\tau_{n,r}$	2.0052 (ps)		
A_0	0.17365 (a.u.)	$\tau_{n,0}$	40 (ps)		
		$\tau_{n,d}$	1000 (ps)		

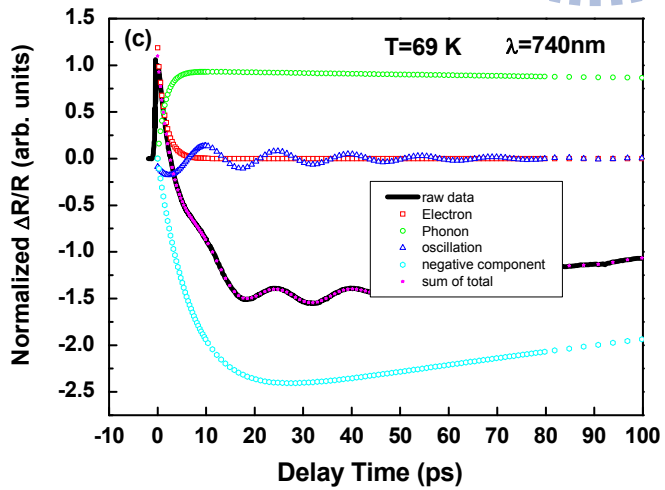


Table		T=69 K		λ =740 nm	
A_e	1.18805 (a.u.)	τ_0	32.771 (ps)		
τ_e	1.59988 (ps)	ω	0.42422 ($2\pi/s$)		
A_p	0.92054 (a.u.)	ϕ	2.0453 (a.u.)		
$\tau_{p,0}$	24.95999 (ps)	A_n	2.3641 (a.u.)		
$\tau_{p,d}$	1200 (ps)	$\tau_{n,r}$	7.33063 (ps)		
A_0	0.19365 (a.u.)	$\tau_{n,0}$	40 (ps)		
		$\tau_{n,d}$	300 (ps)		

Figure 4-6: The choice $\Delta R/R$ curves at (a) 290 K, (b) 200 K, and (c) 69 K include its fitting components. When the temperature is below 200 K, a negative component should be included to well fit the raw data with the lower value at several tens picosecond.

4.2 The temperature-dependent amplitude of $\Delta R/R$

In this section, we discuss the excitation component (rising part of $\Delta R/R$) by using the wavelength-tunable method (photon energies closed to the band gap E_{dd}) to reveal the emergence of long-range antiferromagnetic (AFM) order associated with an abnormally large blueshift of Mn^{3+} $3d$ bands at T_N . The temperature-dependent amplitude of $\Delta R/R$ shows in subsection 4.2.1 and 4.2.2, respectively.

4.2.1 The amplitude of $\Delta R/R$ between 20-300 K

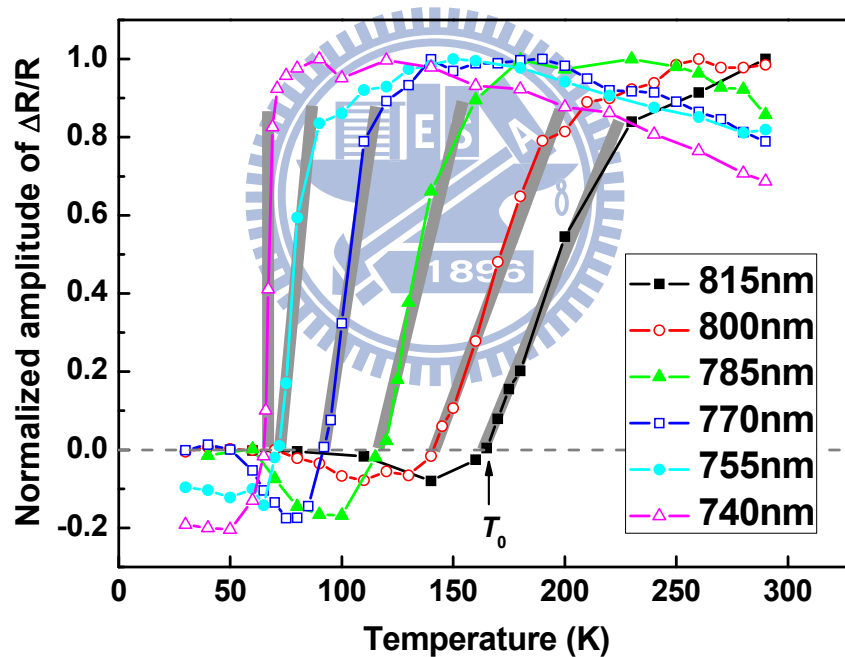


Figure 4-7: The normalized amplitude of $\Delta R/R$ as a function of temperature at various wavelengths (λ) taken from Fig. 4-1 at zero delay time. The gray thick lines are a guide to the eye emphasizing the behavior of slope.

Figure 4-1 shows the typical temperature-dependent $\Delta R/R$ for the h -HMO crystals obtained at different photon energies in subsection 4.1.1. Now we focus on the amplitude of the rising component. For the case of $\lambda = 800$ nm in Fig. 4-1 (e), the amplitude of the

excitation component of $\Delta R/R$ appears to remain constant at high temperatures until it starts to drop noticeably around $T = 170$ K. At $T \sim 150$ K the amplitude of the excitation component has diminished almost completely and with $T < 140$ K it even becomes “negative”, albeit only barely recognizable.

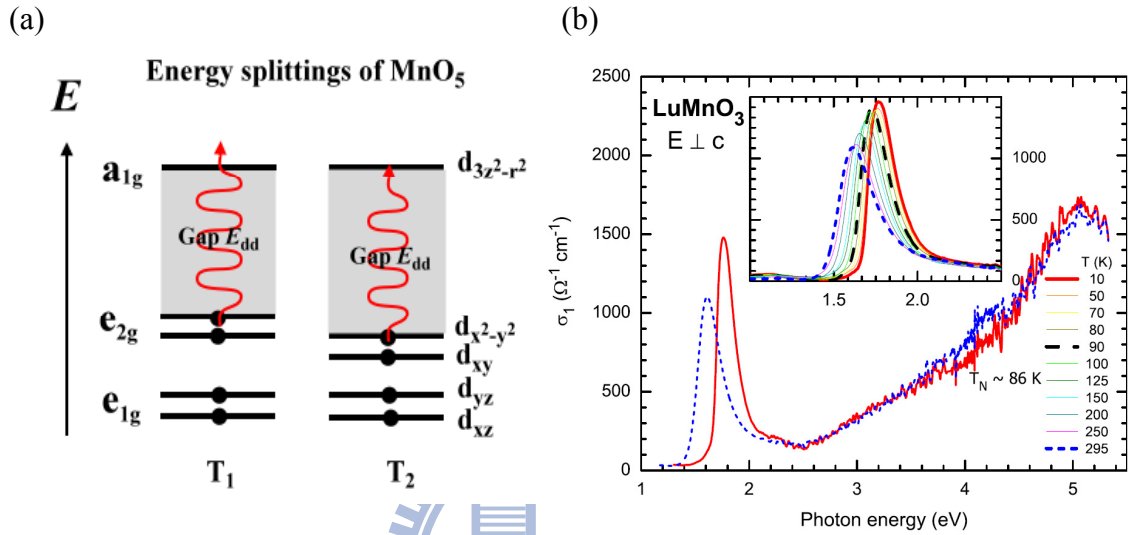


Figure 4-8: (a) The band structure of the local environment MnO₅ for photon energy above and below E_{dd} ($T_1 > T_2$). (b) The electronic conductivity of LuMnO₃ at 300 K and 10 K [3].

In order to further discuss the physical meaning of the excitation component (non-thermal process) of $\Delta R/R$, the amplitude of $\Delta R/R$ as a function of temperature was measured with various pumping wavelengths (photon energies). Fig. 4-7 shows that, for each photon energy used, the amplitude of $\Delta R/R$ remains essentially unchanged at higher temperature region. It then drops precipitously to cross zero amplitude at some characteristic temperature T_0 and becomes negative. For instance, in the case of $\lambda = 815$ nm, the amplitude of $\Delta R/R$ starts to drop steeply below 220 K and across zero at $T_0 \sim 160$ K. Since the photon energy is in the range of $d-d$ transition for the h - $ReMnO_3$ (absorption peak ~ 1.6 eV at room temperature [3], show in Fig 4-8(b)), the absence of the excitation component is thus a clear indication of inadequate photon energy to trigger the $d-d$ transition (as depicted schematically

in Fig. 4-8 (a). For the electronic structure of *h*-HMO, please see the discussion in previous subsection 2.1.3). The electrons residing on the e_{2g} orbital (d_{xy} and $d_{x^2-y^2}$) can transfer to the unoccupied a_{1g} orbital ($d_{3z^2-r^2}$) by absorbing pumping photons with energy exceeding E_{dd} . Conversely, this on-site Mn^{3+} $d-d$ transition will be blocked completely when the energy gap E_{dd} becomes larger than the energy of pumping photons, leading to the precipitous diminishing in the amplitude of $\Delta R/R$. The fact that T_0 gradually shifts to lower temperatures with the increasing the photon energy, thus, indicates that E_{dd} is having a blue-shift with decreasing temperature (Fig. 4-9(a)). This is, in fact, consistent with that observed in other *h*- $ReMnO_3$ materials by FTIR or optical spectroscopic measurements [3-6].

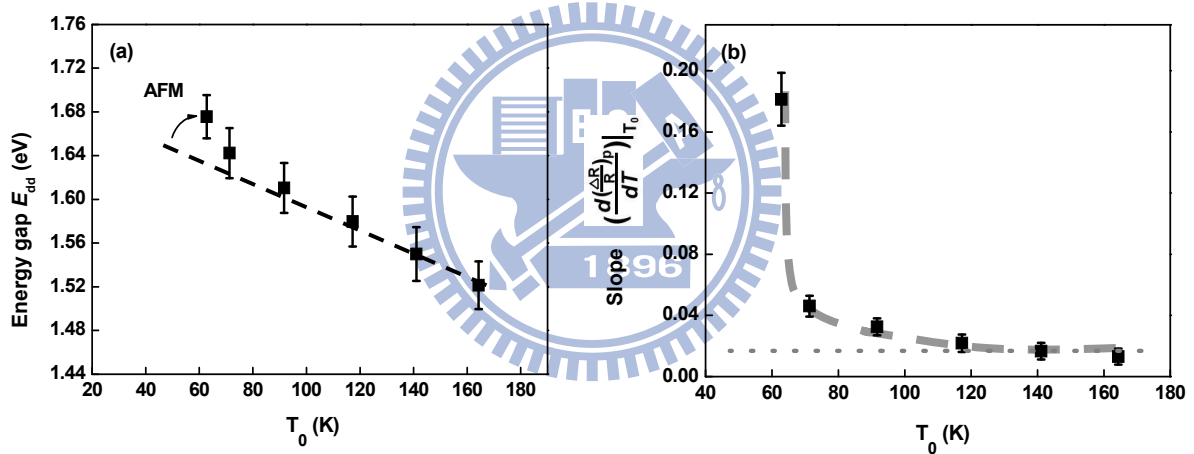


Figure 4-9: (a) The energy gap E_{dd} as a function of T_0 . E_{dd} is estimated from the wavelengths in Fig 4-7 and the error bars are the bandwidth of laser spectrum at various center wavelengths. The dashed line is a guide to the eye emphasizing the linear behavior at high-temperature range. (b) The slope of the temperature-dependent normalized amplitude of $\Delta R/R$ in Fig. 4-7 (the gray thick lines) as a function of T_0 at various wavelengths. (Dashed line is a guide to the eye emphasizing the behavior of slope.)

Intuitively, the blue-shift of E_{dd} might be attributed to thermal contraction of the lattice and, hence, the enhanced crystal field effect on splitting the respective d orbitals. Nevertheless, recent investigations have indicated that the blue-shift of E_{dd} might be correlated with mechanisms other than simply due to the crystal field effect associated with the symmetry

distortion of the local environment of MnO_5 bi-pyramids [7-8]. Souchkov *et al.* [3], based on fitting their absorption spectroscopy results and estimation of superexchange energy of $h\text{-LuMnO}_3$, argued that the unit cell volume change (only $\sim 0.3\%$) caused by lowering the temperature from 300 K to 2 K is certainly inadequate to fully account for the relatively large change (0.2 eV or about 10% change) observed in E_{dd} . Consequently, they suggested that the blue-shift in E_{dd} might be due to the emerging superexchange interaction between neighboring Mn ions, which, in turn, gives rise to a lowering of the e_{2g} levels in the AFM state while leaving the relatively isolated a_{1g} orbital intact. They further proposed that even the short-range AFM correlations existing in the frustrated magnetic systems like $h\text{-ReMnO}_3$ will result in noticeable shift in the resonance energy. These assertions are, however, rather indirect and evidences that directly correlate the blue-shift and magnetic ordering are in order. Within the context of this superexchange-induced effect, one expects the blue-shift in E_{dd} might turn on at temperatures much higher than the usually conceived T_N (~ 76 K) even when the system is only in the dynamical short-range ordering state. It is interesting to note that, if we regard the photon energy as E_{dd} and plot it as a function of T_0 at which the excitation signal vanishes (as shown in Fig. 4-9(a)), a seemingly linear behavior (dashed line in Fig. 4-9(a)) is evident, indicative of a gradual increase in the extent of AFM ordering. Moreover, the behavior starts to deviate from being linear around T_N (~ 76 K), suggesting an extra enhancement in the blue-shift of E_{dd} due to the prevailing of global long-range AFM ordering. In order to further explore the possible connections between the magnetic ordering state and the excitation component of $\Delta R/R$, the slope of $\Delta R/R$ taken at temperatures slightly above T_0 ($\left. \frac{d(\Delta R/R)_p}{dT} \right|_{T_0}$, indicated by the gray thick lines in Fig. 4-7) as a function of the pumping photon energy is displayed in Fig. 4-9(b). If we attribute the blue-shift of energy gap E_{dd} to being due to the short-range AFM ordering emerging at temperatures far above T_N , the results shown in Fig. 4-9(b) can thus be regarded as indications of how the AFM correlation evolves

with the temperature as it approaches T_N . The fact that $(\frac{d(\Delta R/R)_p}{dT})$ increases gradually with reducing temperatures and rises sharply around T_N , thus, follows closely with the emergence of short-range to long-range-ordered AFM with decreasing temperature in this frustrated magnetic system.

Up till now, this phenomenon of extra-large blueshift at T_N only had been explained easily with the appearance of AFM ordering (charge-spin coupling). But no one can precisely explain why the change of the energy gap around 3 % is much larger than the change of lattice constant at T_N . There are no direct evidences from the theoretical and experimental data can proof. Very recently, the powerful and crucial evidence has already appeared which is the recent paper reported by Lee *et al* [9-10]. According to their high-resolution neutron diffraction experiments, they found that the hexagonal manganites undergo an isostructural transition at T_N , simultaneously producing giant atomic displacement for every atom in the unit cell. The giant atomic displacement at T_N is interpreted by magnetoelastic effect. When the magnetic spin order formed AFM, the strong in-plane Mn-Mn interactions cause a reduction in the Mn-O and Mn-Mn distances [11-12]. The results show that the relative shift of Mn position in the unit cell is almost 3.3 % and the displacement of Mn atoms induced by AFM correlation play a very important role in hexagonal manganites. Therefore, from our observation it is reasonable that the environment change of crystal fields of Mn ions causes the $3d$ bands have an unexpected large blueshift at T_N .

According to the above-mentioned physical properties, we believe the $d-d$ excitation and extra-blueshift behavior at T_N could be called ME coupling effect to instead of the charge-spin coupling. This is because that the electron transition between various bands belongs to the electric polarization in classical model. Although the pump-probe experiments operates at

optical frequency range unlike the dielectric constant and electric dipole moment measurement at kilohertz to megahertz range, both of them reveal the ME coupling effect in h -HoMnO₃ materials.

4.2.2 The amplitude of $\Delta R/R$ in high temperature range

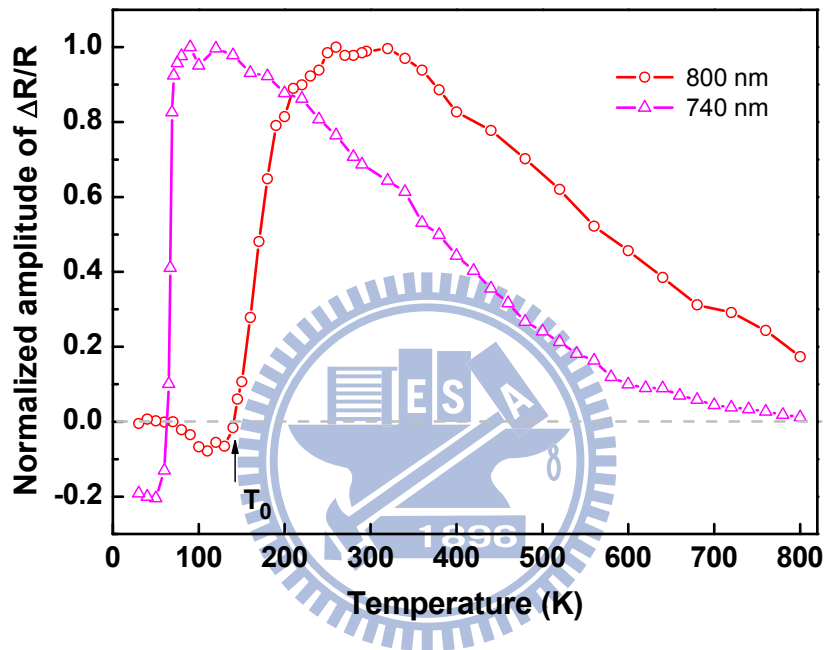


Figure 4-10: The amplitude of $\Delta R/R$ in high temperature range with $\lambda = 740$ nm and 800 nm.

Figure 4-10 shows the results of pump-probe measurements above the room temperature. From 300 K to 800 K, the amplitude of $\Delta R/R$ becomes smaller and smaller with increasing temperatures. This means that the energy gap E_{dd} still blueshift from 800 K to room temperature. Thus, the results of amplitude of $\Delta R/R$ show a wide variety of the energy gap E_{dd} . Fig. 4-11 shows the gap shift by measuring the Fourier transform infrared spectrometer (FTIR spectrometer). The peak position shifts ~ 0.15 eV from room temperature to 10 K, which represents that the conduction band a_{1g} could shift so large value. Thus, we propose that the

amplitude of $\Delta R/R$ data with changing temperatures from 800 K to 50 K could trace out the shape of density of states (DOS).

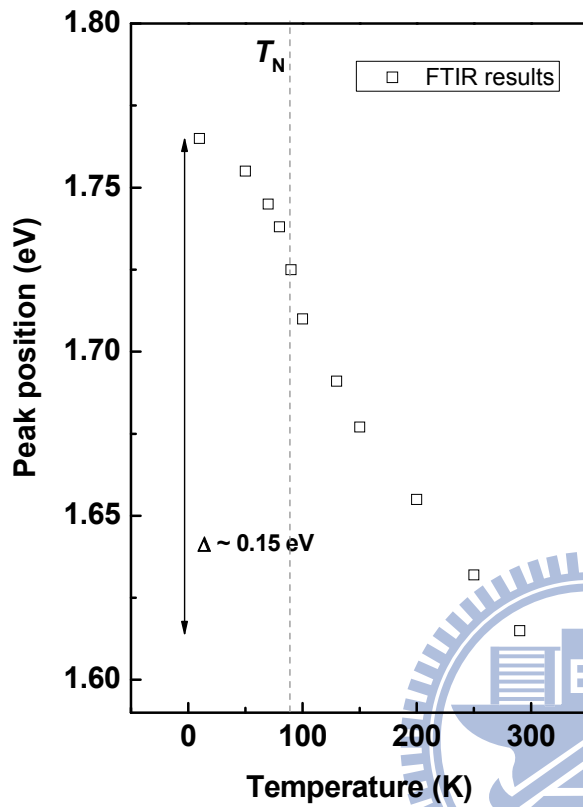


Figure 4-11: The temperature-dependent position of the 1.7 eV peak. Those data was taken from Ref. [3].

4.3 The anisotropic magnetoelastic coupling in *h*-HMO

In above section 4.2, we presented the magnetoelectric coupling in *h*-HMO via the amplitude of $\Delta R/R$. In this section, we will present another important observation in *h*-HMO multiferroic materials that is magnetoelastic behavior through the thermal relaxation process. We used femtosecond pump-probe method to study the relaxation dynamics after ultrashort laser pulse excitation and observed the occurrence of magnetoelastic coupling effect at T_N on *a-b* plane and along *c*-axis, respectively.

4.3.1 Laser-induced thermoelastic generation

For the standard pump-probe experiments (please see the previous discussions in subsection 4.1.2), it can be easily distinguished into two classes that is the nonthermal process during the excitation of pump and the thermal process after pumping [13]. The first process (nonthermal) is described as a pump -induced change in the population of electrons in the bands. This nonthermal process occurs while the pump quanta absorption and lasts the electronic cloud out of equilibrium. Subsequently, the thermal processes are that the electronic subsystem starts to transfer its energy in order to return to the initially equilibrium state. Typically, the three temperature model is widely accepted to describe the energy transfer processes in the strong correlated systems [14-15]. The energy is redistributed to the lattice or spin subsystems, but it still depends on its own properties of material systems. For the pump-probe mechanism, the energy transfers from the hot electrons to the lattice subsystem , called thermoelastic stress generation process, which is a very important process for the electrons and lattice reaching a new thermal equilibrium. The thermoelastic generation from the increase of lattice temperature produces an expansion of stress via ultrashort laser heating

[16-18]. Usually, the characteristic time of the thermoelastic generation process is around a few picosecond. Under some conditions, the lattice stress may induce the coherent lattice motion (coherent optical or acoustic phonon). Namely, these coherent phonons are excited by the thermal expansion due to the absorption of laser radiation [19-20]. Fig. 4-12 shows the basic physical picture which describes the thermal processes induced the lattice deformation or displacement of atoms in certain crystals.

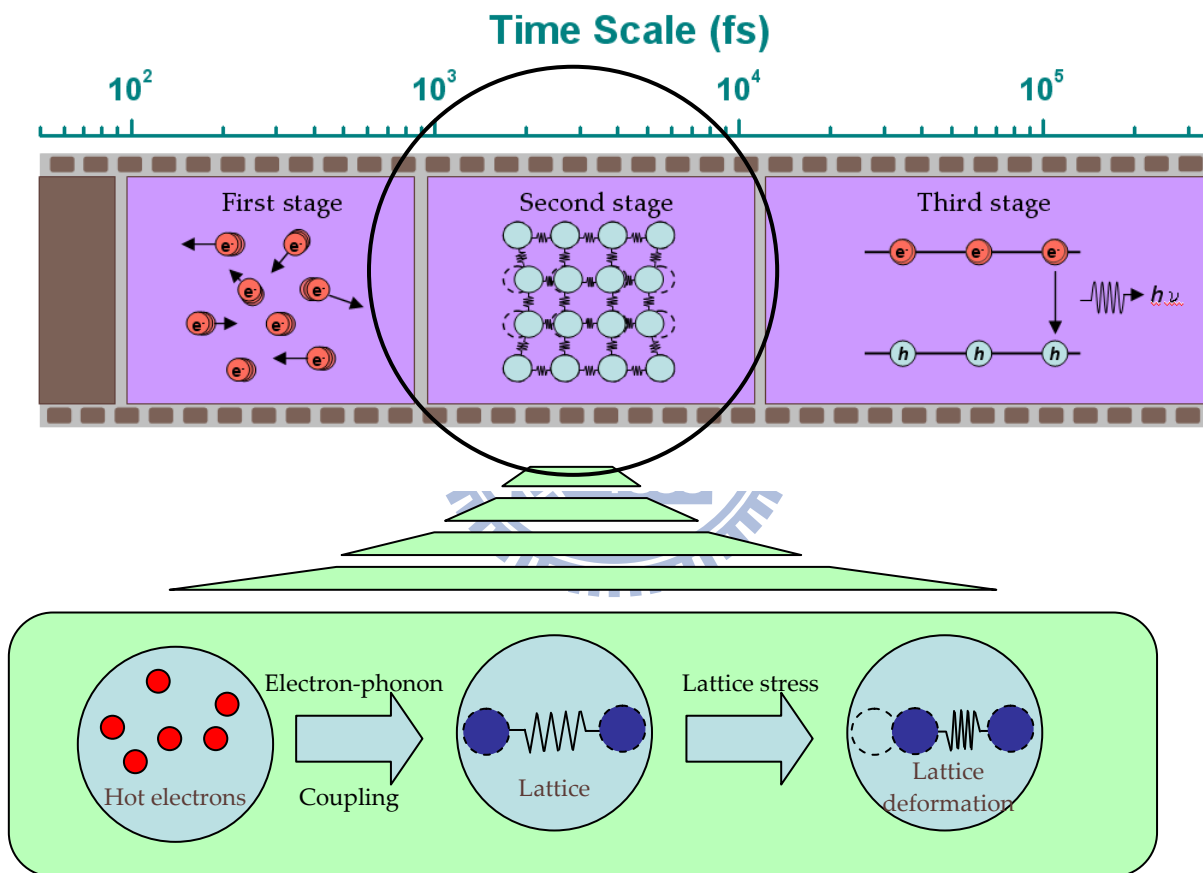


Figure 4-12: The fundamental concept of the thermoelastic generation via laser irradiate. The laser induced the expansion of lattice or the displacement of atoms in crystals.

In the case of laser-induced lattice dynamics, we can observed the anisotropic thermoelastic effect via two different relaxation components in $\Delta R/R$ on a - b plane and along

c -axis, respectively. The first component is “negative” component which describes the thermal stress on a - b plane. Another component is the oscillation caused by a strain pulse along c -axis. These two components have been mathematically described in subsection 4.1.3 via Eq. (4.3). Moreover, in the following subsection 4.3.2 we will further construct the physical pictures for the laser-induced anisotropic strain along two directions in h -HoMnO₃ materials as shown in Fig. 4-13.

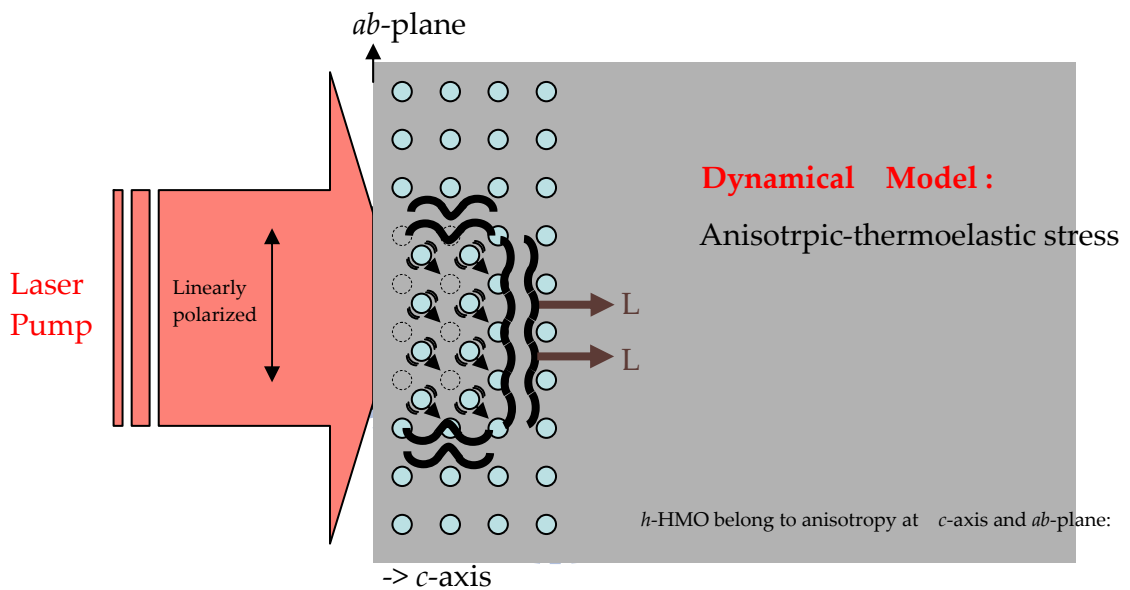


Figure 4-13: *The linear-polarized ultrashort laser pulses shine on samples and induce the anisotropic-thermoelastic stress on a - b plane and along c -axis. The light-blue circles represent the position of atoms.*

4.3.2 Laser-induced lattice dynamics on a - b plane

In our pump-probe results, there are two components assigned to the anisotropic thermoelastic stress. In this subsection, we focused on the “negative” component in details.

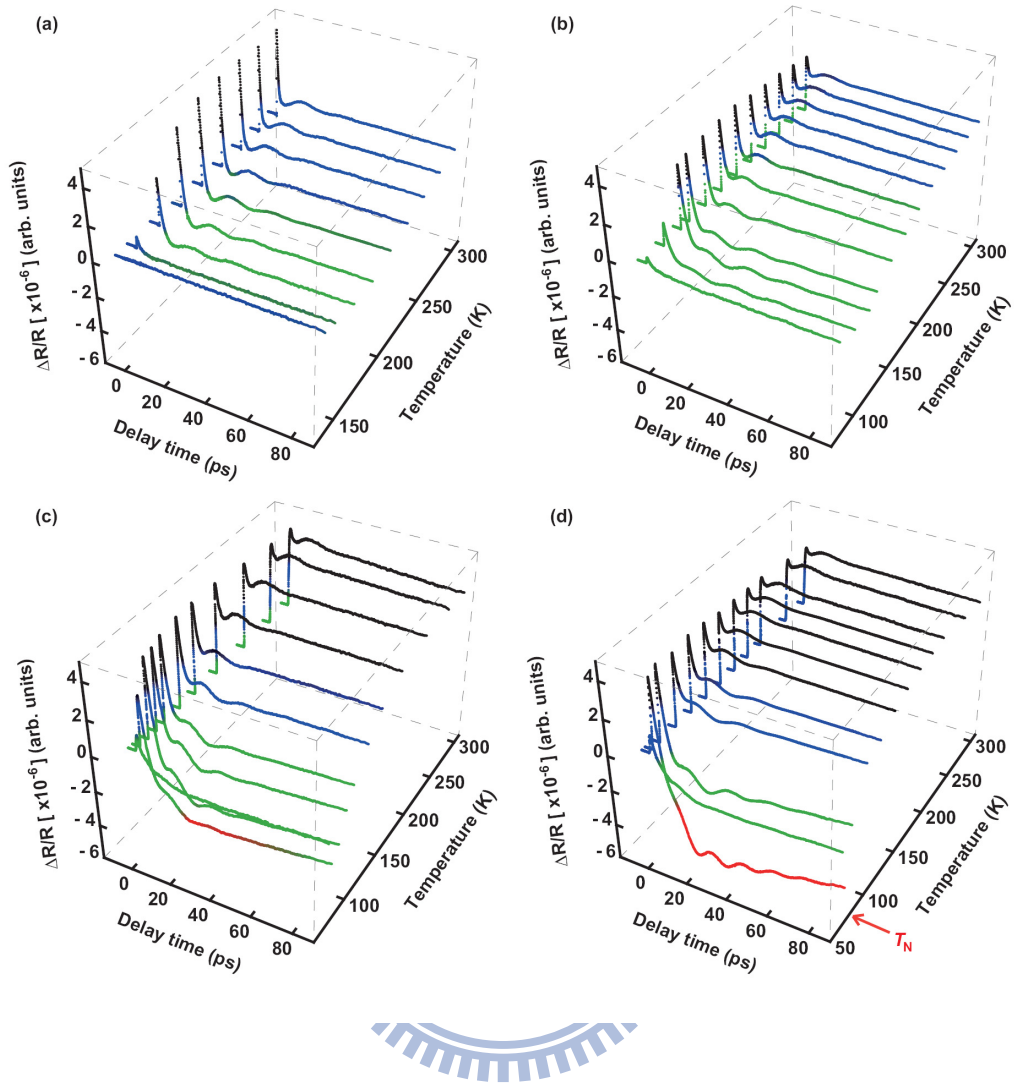


Figure 4-14: The photo-induced $\Delta R/R$ plotted as a function of temperature at various wavelengths: (a) $\lambda = 800 \text{ nm}$, (b) $\lambda = 770 \text{ nm}$, (c) $\lambda = 755 \text{ nm}$, (d) $\lambda = 740 \text{ nm}$. The plentiful hues represent the amplitude changes of $\Delta R/R$ in order to emphasize the particular behavior at T_N .

What is the “negative” component? This term is, for the first time, discovered by the pump-probe experiments. In the Fig. 4-14(d), the relaxation part ($t > 0$) is almost the same from room temperature to 200 K. Below 200 K, the relaxation component significantly decreases and then even overshoot to the initial value of the $\Delta R/R$ before the zero delay time at very low temperature (near T_N). This characteristic has been emphasized by draw the plentiful hues in the $\Delta R/R$ signals show in Fig. 4-14(d). Below 200 K, we argue that the lower

value comes from the emergence of an opposite component and named as “negative” component. Interestingly, the negative component grows tardily far away T_N and grows greatly close to T_N . We have an idea that the negative component should come from the thermoelastic effect due to energy transfer via electron-phonon relaxation process which causes the expansion of lattice. It is reasonable that the negative component from zero delay time to the lowest point (point of reversal) spend on a few picosecond (see the arrow shown in Fig. 4-15(a)). Fig 4-15(b) shows the evidences that from zero delay time to the lowest point in all wavelengths spend on a few picosecond belongs to electron-phonon relaxation process.

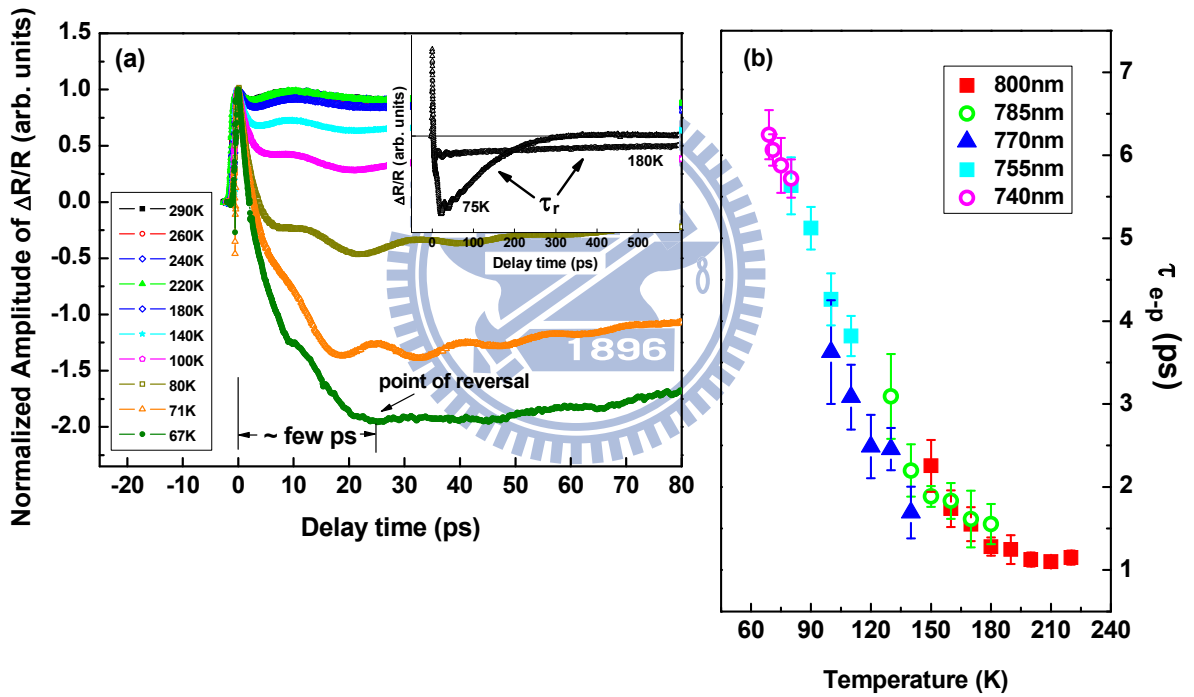


Figure 4-15: (a) The normalized amplitude of $\Delta R/R$ curves at $\lambda = 740$ nm. The inset shows the reordering time τ_r of the disordered magnetization. (b) The temperature-dependent τ_{e-p} for various wavelengths.

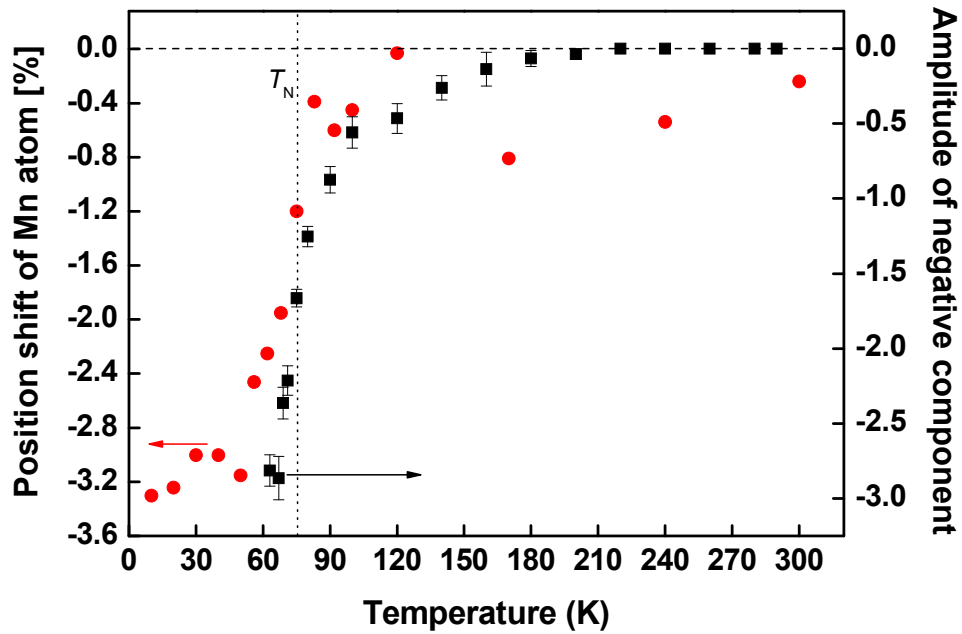


Figure 4-16: *The amplitude of negative component plotted as a function of temperature strongly indicates that the appearance of the negative component coupling with AFM ordering at T_N . Below 200 K, it clearly show the short-range AFM effect. (The red-circle data were taken from Ref. [9], note that the T_N of $YMnO_3$ and $HoMnO_3$ were 70 K and 76 K, respectively)*

Thus, this process can be regarded suitably as the expansion of lattice or the position shift of atoms by laser pumping. Fig. 4-16 shows the amplitude of negative component (black-square) at various temperatures which taken from the fitting results (parameter A_n in Eq. (4.3)). Fig. 4-16 also shows the position shift of Mn atoms (red-circle) from Lee's paper [9]. Comparatively speaking, it clearly indicates that the emergence of the largest negative component is related to the magnetoelastic due to the large position shift of Mn atoms at T_N (Fig. 4-17 shows the position shift of Mn atoms). When the electron-phonon relaxation process occur at T_N , the rise of lattice temperature will disturb the AFM ordering (spin-lattice coupling) cause the position of Mn atoms move return to the position of higher temperature. In other words, when the h -HMO undergo a large local distortion of lattice at T_N , we utilize

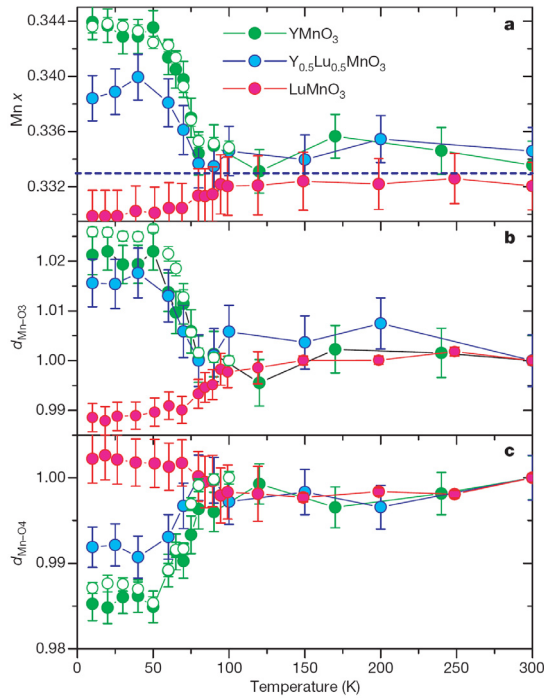


Figure 4-17: *The temperature dependence of the Mn x position and the Mn-O bond distances obtained from high-resolution neutron and synchrotron powder diffraction experiments [9].*

the pump pulses to induce a reverse deformation of lattice and observe the negative component of $\Delta R/R$ via the electron-phonon process. By the way, the 3d bands of Mn ions will change by laser pumping, i.e. redshift of 3d bands. It is worth emphasizing that, by the optical technique, the AFM short-range ordering of Mn ions which is represented via the small negative component above T_N can be observed clearly between 200 K and T_N [21].

Figure 4-15 (b) shows the temperature dependence of τ_{e-p} collected from the studies with various photon energies. It is evident that τ_{e-p} increases significantly from 1 ps at 220 K to 6 ps at 70 K, indicating the prominent role played by the state of magnetic ordering. Furthermore, the monotonic and seemingly universal behavior again indicates that it needs longer time to disturb the spin system when the magnetic ordering is more robust at lower temperatures due to the prevailing of the long-range AFM ordering. The magnetic ordering disturbed by spin-lattice coupling (increase T_s) has to be somehow reordered, i.e., the cooling of spin system. In this case, one expects that, due to the competition between the AFM superexchange interaction and thermal energy, the disturbed magnetic ordering should spend shorter time to reorder at lower temperatures. Indeed, as shown in the inset of Fig. 4-15(a), we

can identify that the characteristic reordering time τ_r is about 120 and 610 ps for $T=75$ K and $T=180$ K, respectively.

Why does the pump induced reverse local distortion of lattice reveal in our $\Delta R/R$ signals through opposite sign? We interpret and propose that the opposite sign comes from the pump-induced variation of density of states (DOS) which explored by probe pulses. Fig. 4-18(a) and (b) show that the pump-induced redshift of $3d$ bands will generate more unoccupied states (the Fig. 4-18 gives an example: temperature at 150 K). The Fig. 4-18(a) represents the band structure of Mn atom just after the ultrashort pulse excitation (delay time nearly closed to zero). Also, the Fig. 4-18(b) shows the redshift of band structure of Mn atom induced by pump laser (the shift of energy band spends on around a few picosecond). Therefore, the probe pulses can explore more empty states of $3d$ bands (the pink-arrow shown in Fig. 4-18) and cause the reflectivity change ($\Delta R/R$) with a negative sign as shown in Fig. 4-18(c)-(d). Consequently, we conclude that the appearance of the largest negative component is due to the largest changes of DOS at T_N .

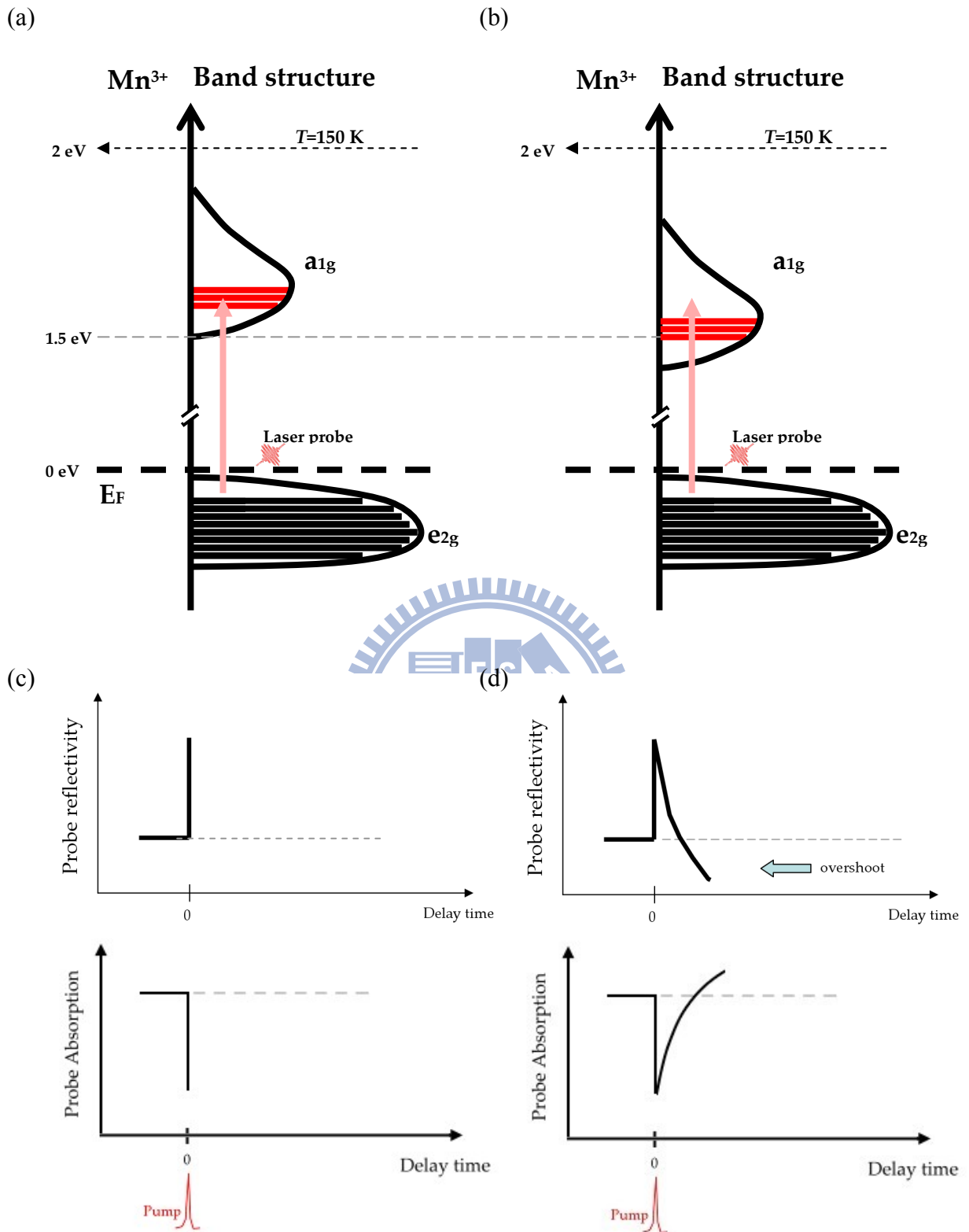


Figure 4-18: (a) The energy band of Mn^{3+} ions at $T=150\text{ K}$, the red-line represents the occupied states by excited electrons. Pink-arrow represents that the probe pulse explore the position of energy. (b) The pump induces the redshift of 3d bands. (c)-(d) show that the probe reflectivity at different delay time.

4.3.3 Laser-induced strain pulse propagation along c -axis

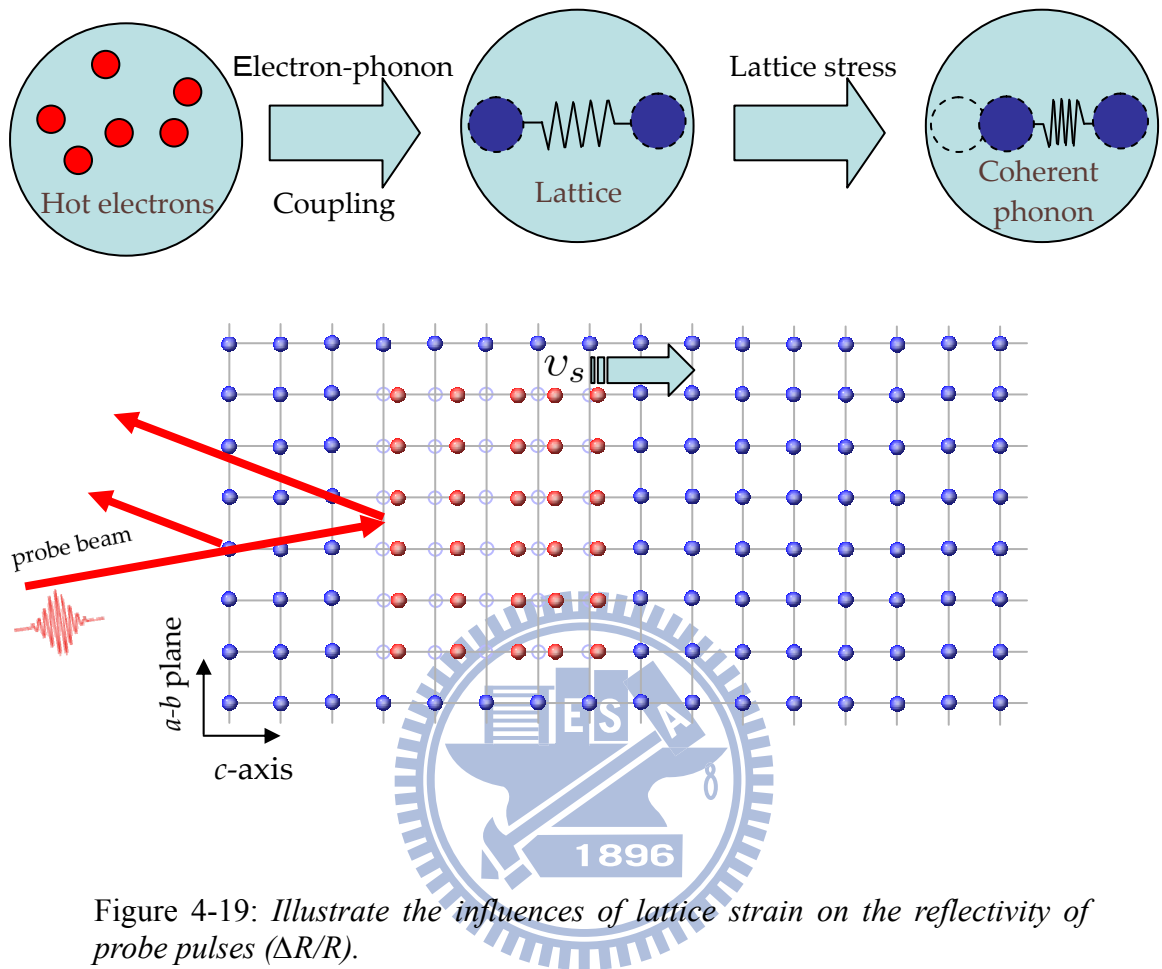


Figure 4-19: Illustrate the influences of lattice strain on the reflectivity of probe pulses ($\Delta R/R$).

In this subsection, another pump-induced thermoelastic stress along c -axis is the oscillation component in the $\Delta R/R$ curves (description by the final term of Eq. (4.3)). The damped oscillations in the $\Delta R/R$ curves, originally identified by Thomsen *et al.* [16-17], have been ascribed to the interference between the probe beams reflected from the crystal surface and the rear interface of the propagating strain pulse which is generated by the electronic stress, lattice stress, and coherent acoustic phonon (CAP). Fig. 4-19 shows the physical picture which demonstrates how the lattice strain influences the $\Delta R/R$ of the probe pulses. In the case of h -HoMnO₃, the generation of CAP along c -axis can be regarded as

one-dimensional problem. These nonthermal and thermal contributions lead to the general expression of stress tensor: $\sigma_{ij} = \sigma_e + \sigma_p$, where the σ_e corresponds to electronic stress and σ_p corresponds to thermoelastic stress. The thermoelastic stress in an isotropic medium can lead to the expression of stress tensor: $\sigma_p = -3K\beta\Delta T_l$, where K is the bulk elastic modulus, ΔT_l is the lattice temperature rise, β is the linear thermal-expansion coefficient. From Thomsen's model, the reflectivity dependence in the presence of a generalized disturbance of the dielectric function can be obtained by solving the Maxwell and Fresnel equations as:

$$R = |r_0 + \Delta r|^2, \quad (4.4)$$

where

$$r_0 = \frac{n_i \cos \theta_i - n_t \cos \theta_t}{n_i \cos \theta_i + n_t \cos \theta_t} = \frac{1 - n - i\kappa}{1 + n + i\kappa} \quad (4.5)$$

is the reflection coefficient at the sample surface and represents that part of the electric field of probe beam reflected from the free surface (n_i is the refractive index of air), while

$$\Delta r = \frac{2i\omega}{c(1+n+i\kappa)^2} \int_0^\infty dz' e^{2i(n+i\kappa)k_0 z'} \Delta \varepsilon(z, t) \quad (4.6)$$

Corresponds to the probe electric field reflected from the CAP transient [18]. In Eq. (4.5) and (4.6), n and κ are the real and imaginary parts of the refractive index, respectively; ω is the angular frequency of the probe light, c is the speed of light, and k_0 is the wave vector of the probe beam in vacuum; and $\Delta \varepsilon(z, t)$ is the change in dielectric function, which, under assumption that the disturbance is caused only by the propagation of CAPs, can be expressed as

$$\Delta \varepsilon(z, t) = 2(n + i\kappa) \left(\frac{dn}{d\eta_{zz}} + i \frac{d\kappa}{d\eta_{zz}} \right) \eta_{zz}(z, t), \quad (4.7)$$

Finally, κ is related to the probe-beam absorption coefficient α_{probe} or, equivalently, the penetration depth ζ_{probe} through $\kappa = \alpha_{probe} \lambda / (4\pi) = \lambda / (4\pi \zeta_{probe})$, where λ is the probe-beam wavelength.

Thus, we need to rewrite Eq. (4.4) in the form.

$$\frac{\Delta R}{R} = \frac{|r_0 + \Delta r|^2 - |r_0|^2}{|r_0|^2} \quad (4.8)$$

Combining these results and simplifying, it is easy to find that the change in reflectivity correct to the first order in the strain is

$$\Delta R = \int_0^\infty f(z) \eta_{zz}(z, t) dz \quad (4.9)$$

Where

$$f(z) = f_0 \left[\frac{\partial n}{\partial \eta_{zz}} \sin\left(\frac{4\pi n z}{\lambda} - \phi\right) + \frac{\partial \kappa}{\partial \eta_{zz}} \cos\left(\frac{4\pi n z}{\lambda} - \phi\right) \right] e^{-z/\xi} \quad (4.10)$$

The function $f(z)$ called “sensitivity function” to determine how the strain at different depths below the surface of the sample contributes to the change in the reflectivity [16, 18-19].

Finally, the closed-form formula for $\Delta R/R$ can be expressed as a simple damped cosine function:

$$\frac{\Delta R(t)}{R} \propto \cos\left(\frac{4\pi n v_s t}{\lambda} - \phi\right) e^{-v_s t / \xi_{probe}}, \quad (4.11)$$

Where λ is the wavelength of the probe beam, n is the refractive index of samples, and v_s is the speed of sound propagated in the medium, ξ_{probe} is the penetration depth of probe pulses. Finally, the damped oscillation frequency obeys the simplified equation: $\omega = \frac{4\pi n v_s}{\lambda}$.

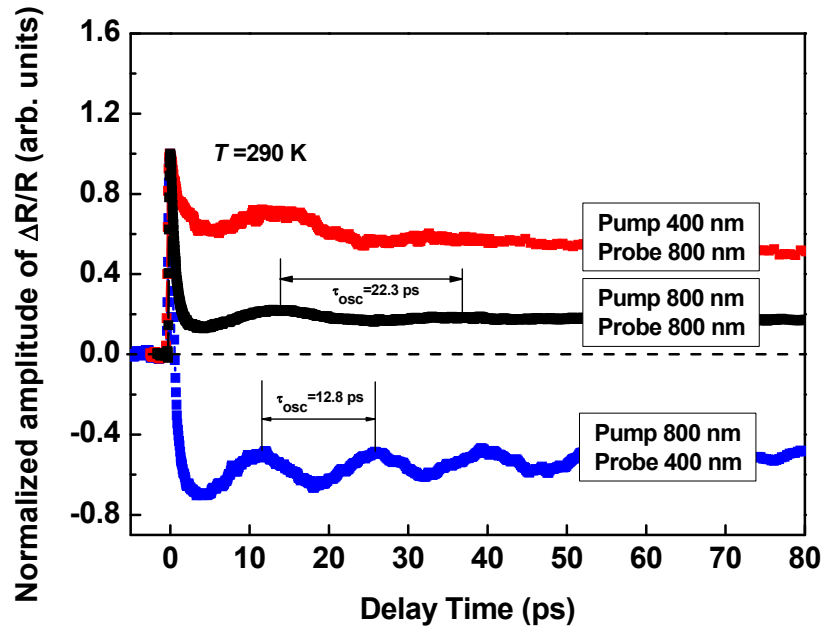


Figure 4-20: The photo-induced $\Delta R/R$ at various pump and probed wavelengths. This figure shows that these curves are evidences of proposed strain pulse model. The oscillation period is proportional to probe wavelengths.

Figure 4-20 clearly shows the oscillations in $\Delta R/R$ ($\tau_{osc} = \frac{2\pi}{\omega}$, ω was obtained from the fitting of Eq. (4.3)) at various pump and probe wavelengths which consist with the strong wavelength (λ)-dependent report of Lim *et al* (Fig. 1(b) in ref. [23]). Moreover, the τ_{osc} are seemingly strong temperature-dependent and indicate that the CAP mode hardens as temperature decreasing. When the temperature is closed to T_N , the τ_{osc} appears abnormally (see the arrow in Fig. 4-22). This unusual change of the τ_{osc} at T_N is clearly shown in Fig. 4-21. This strongly indicates that the AFM ordering correlate to the propagation of thermal stress along c -axis. This is reasonable because many literatures report the extraordinary behavior in some important parameters related to thermal strain along c -axis at T_N , e.g. heat capacity [25-26]. Lee's report [9] also suggests that the rare-earth and oxygen atoms undergo

a displacement along c -axis at T_N . Consequently, the emergence of magnetoelastic effect at T_N causes the extraordinary strain propagation along c -axis has been observed in our studies.

Another interesting thing is that the coupling between ferroelectric and elastic ordering in h -HMO single crystals has been clearly revealed in the temperature-dependent τ_{osc} of the oscillation component in $\Delta R/R$. Besides, the oscillation period is strong wavelength-dependent at high temperature region which is also observed in Lim's *et al.* results. While decreasing the temperatures, however, the oscillation period becomes wavelength-independent. It seems that all of the oscillation periods for various wavelengths converge on same value due to the appearance of AFM ordering. Furthermore, the damping time (τ_o in Eq. (4.3)) of oscillation in $\Delta R/R$ gradually rises with decreasing temperatures below 200 K and exceeds 100 ps around T_N as shown in Fig. 4-21. This strongly indicates that the propagation of a strain pulse with the modulation of dielectric constant (or ferroelectric polarization) along c -axis has been indeed affected by the appearance of AFM ordering around T_N . By the neutron diffraction experiments, Lee *et al.* [9] also observed the extra displacement of the rare-earth and oxygen atoms along c -axis at T_N . Thus, they further claimed that the magnetoelastic effect is the primary origin of the magneto-electric coupling in this intriguing class of materials, which has been clearly demonstrated from the negative and oscillation components of $\Delta R/R$ in h -HMO. That is the ferroelectric ordering can be probed through the electro-elastic coupling disclosed in the oscillation component of $\Delta R/R$. Also, the magneto(AFM)-electric coupling has been apparently observed in the anomalously temperature-dependent oscillation period and the amplitude of the negative component in $\Delta R/R$ which are attributed to the magnetoelastic effect.

Very recently, Jang's *et al.* report [27] demonstrates that the pump-probe spectroscopy in

similar hexagonal LuMnO₃ materials. They claimed that the oscillation frequency harden at temperature > 160 K, and then change to weakly softening < 160 K. Moreover, they also claimed the disappearance of phonon modes at T_N is due to the AFM spin ordering. Actually, their pump-probe results are consistent with our previously discuss in previous section 4.2. But, we must emphasize that their data did not show the extra-large blueshift of 3d bands in amplitude of $\Delta R/R$ curves (Fig. 2(b) in ref. [27]), because the photon energy was not enough to excite carriers at T_N . In other words, the disappearance of the amplitude of $\Delta R/R$ in their case just fortuitously takes place at T_N . Actually, they did not have sufficient evidences to prove the extraordinary behavior at T_N . Therefore, we have performed the pump-probe experiments at various photon energies which are larger than those they used and important for studying the strong magnetic ordering. Similarly, the oscillation frequencies in Jang's *et al.* results are consists with our results in high temperature range. On the contrary, when temperature is below 160 K, both of Jang *et al.* and we observed that the oscillation period diminishes gradually and the abnormality appears at T_N .

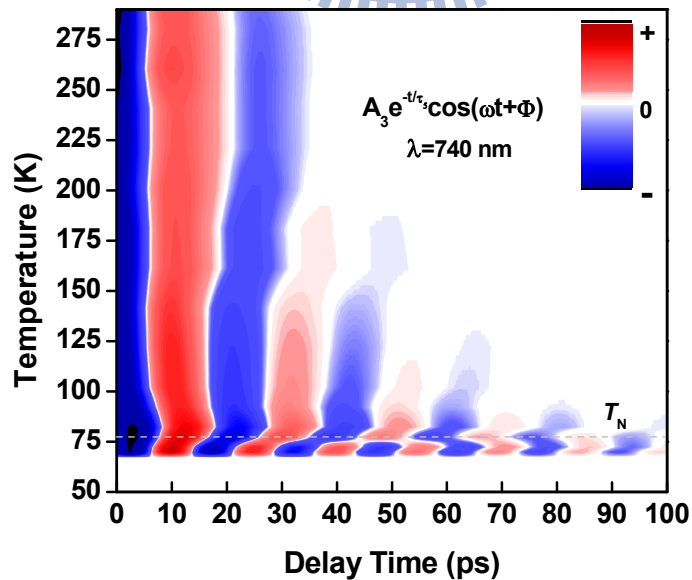
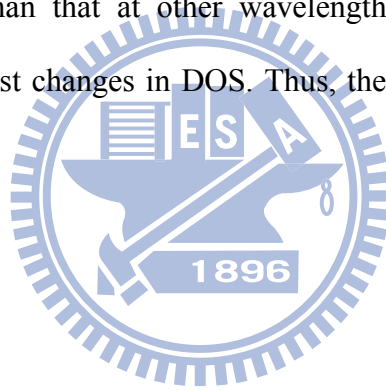


Figure 4-21: The evolution of oscillation component in $\Delta R/R$ at various temperatures. The dash-line shows the abnormal behavior at T_N .

Figure 4-23 shows the temperature-dependent dephasing time (τ_d) at various wavelengths. The τ_d is dominated by the finite penetration depth of the probe wavelength. Moreover, the extinction coefficient k plays an important role for the penetration depth. For various wavelengths, all of τ_d grow gradually when the amplitude of $\Delta R/R$ approaches zero which is marked by the dashed lines in Fig. 4-23. The anomalous increase of τ_d may be due to the photon energy is close to the edge of energy gap E_{dd} . In other words, the penetration depth increases and the absorption of probe photon for $3d$ bands decreases (the blueshift of $3d$ bands and the DOS reduce at lower temperature) as decreasing the temperatures. The changed amount of the dephasing time (Δ_{740}) at $\lambda_{probe} = 740$ nm from room temperature to low temperature is much larger than that at other wavelengths. The emergence of magnetic ordering at T_N causes the largest changes in DOS. Thus, the penetration depth will have the largest change.



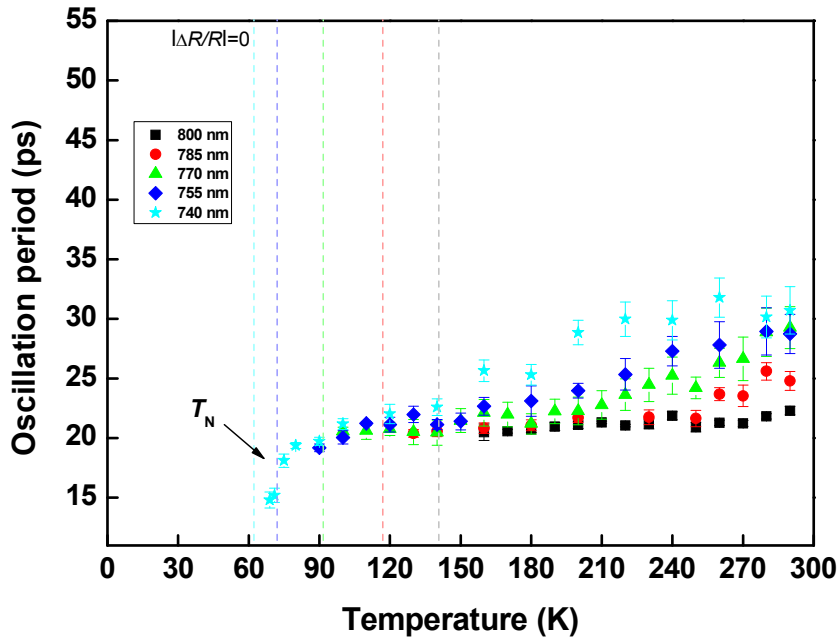


Figure 4-22: The fitting results of oscillation at various wavelengths. The dashed lines represent the amplitude of $\Delta R/R$ equal to zero.

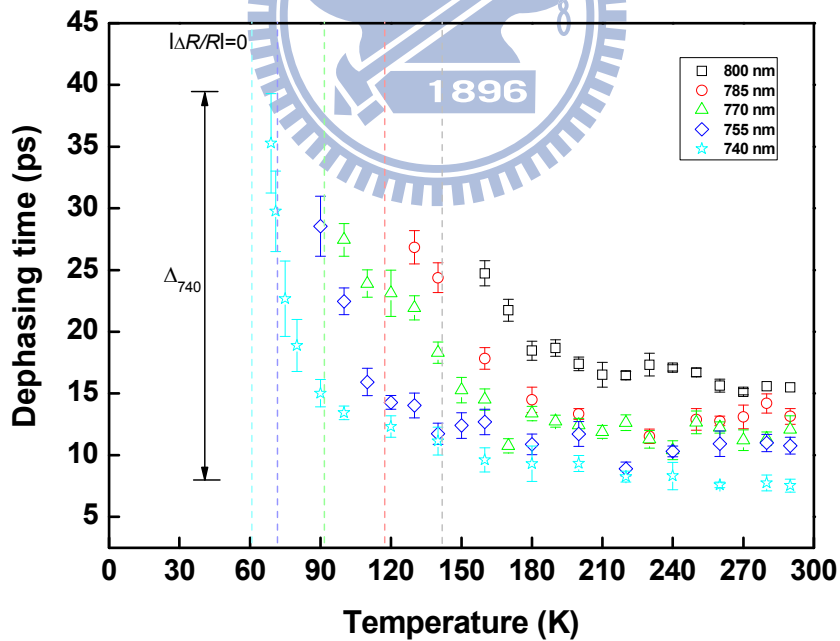


Figure 4-23: The fitting results of dephasing time at various wavelengths. The dashed lines represent the amplitude of $\Delta R/R$ equal to zero.

References

- [1] J. Shah, M. Cardona, P. Fulde, K. V. Klitzing, and H. J. Queisser, “Ultrafast spectroscopy of semiconductors and semiconductor nanostructures”, second enlarged edition, Springer, (1996)
- [2] T. Ogasawara, K. Ohgushi, Y. Tomioka, K. S. Takahashi, H. Okamoto, M. Kawasaki, and Y. Tokura, *Phys. Rev. Lett.* **94**, 087202 (2005).
- [3] A. B. Souchkov, J. R. Simpson, M. Quijada, H. Ishibashi, N. Hur, J. S. Ahn, S. W. Cheong, A. J. Millis, and H. D. Drew, *Phys. Rev. Lett.* **91**, 027203 (2003).
- [4] W. S. Choi, S. J. Moon, S. S.A. Seo, D. Lee, J. H. Lee, P. Murugavel, T. W. Noh, and Y. S. Lee, *Phys. Rev. B* **78**, 054440 (2008).
- [5] W. S. Choi, D. G. Kim, S. S. A. Seo, S. J. Moon, D. Lee, J.H. Lee, H. S. Lee, D.-Y. Cho, Y. S. Lee, P. Murugavel, J. Yu, and T. W. Noh, *Phys. Rev. B* **77**, 045137 (2008).
- [6] R. C. Rai, J. Cao, J. L. Musfeldt, S. B. Kim, S.-W. Cheong, and X. Wei, *Phys. Rev. B* **75**, 184414 (2007).
- [7] D.-Y. Cho, S.-J. Oh, D.G. Kim, A. Tanaka, and J.-H. Park, *Phys. Rev. B* **79**, 035116 (2009).
- [8] C.-Y. Ren, *Phys. Rev. B* **79**, 125113 (2009).
- [9] Seongsu Lee, A. Pirogov, Misun Kang, Kwang-Hyun Jang, M. Yonemura, T. Kamiyama, S.-W. Cheong, F. Gozzo, Namsoo Shin, H. Kimura, Y. Noda, and J.-G. Park, *Nature* **451**,809 (2008).
- [10] Seongsu Lee, A. Pirogov, Jung Hoon Han, J.-G. Park, A. Hoshikawa, and T. Kamiyama, *Phys. Rev. B* **71**, 180413(R) (2005).
- [11] T. A. Tyson, T. Wu, K. H. Ahn, S.-B. Kim, and S.-W. Cheong, *Phys. Rev. B* **81**, 054101 (2010).
- [12] X. Fabrèges, S. Petit, I. Mirebeau, S. Pailhès, L. Pinsard, A. Forget, M. T.

- Fernandez-Diaz, and F. Porcher, Phys. Rev. Lett. **103**, 067204 (2009).
- [13] P. Ruello, S. Zhang, P. Laffez, B. Perrin, and V. Gusev, Phys. Rev. B **79**, 094303 (2009).
- [14] E. Beaurepaire, J.-C. Merle, A. Daunois, and J.-Y. Bigot, Phys. Rev. Lett. **76**, 4250 (1996).
- [15] G. M. Müller, J. Walowski, M. Djordjevic, G.-X. Miao, A. Gupta, A. V. Ramos, K. Gehrke, V. Moshnyaga, K. Samwer, J. Schmalhorst, A. Thomas, A. Hütten, G. Reiss, J. S. Moodera, and M. Münzenberg, Nature Mater. **8**, 56 (2008).
- [16] C. Thomsen, J. Strait, Z. Vardeny, H. J. Maris, J. Tauc, and J. J. Hauser, Phys. Rev. Lett. **53**, 989 (1984).
- [17] C. Thomsen, H. T. Grahn, H. J. Maris, and J. Tauc, Phys. Rev. B **34**, 4129 (1986).
- [18] S. Wu, P. Geiser, J. Jun, J. Karpinski, and Roman Sobolewski, Phys. Rev. B **76**, 085210 (2007).
- [19] T. Pezeril, P. Ruello, S. Gougeon, N. Chigarev, D. Mounier, J.-M. Breteau, P. Picart, and V. Gusev, Phys. Rev. B **75**, 174307 (2007).
- [20] H. Park, X. Wang, S. Nie, R. Clinite, and J. Cao, Phys. Rev. B **72**, 100301(R) (2005).
- [21] Junjie Li, Rick Clinite, Xuan Wang, and Jianming Cao, Phys. Rev. B **80**, 014304 (2009).
- [22] H. J. Lee, J. Workman, J. S. Wark, R. D. Averitt, A. J. Taylor, J. Roberts, Q. McCulloch, D. E. Hof, N. Hur, S.-W. Cheong, and D. J. Funk, Phys. Rev. B **77**, 132301 (2008).
- [23] Th. Lonkai, D. G. Tomuta, J.-U. Hoffmann, R. Schneider, D. Hohlwein, and J. Ihringer, J. Appl. Phys. **93**, 8191 (2003).
- [24] D. Lim, R. D. Averitt, J. Demsar, A. J. Taylor, N. Hur and S. W. Cheong, Appl. Phys. Lett. **83**, 4800 (2003).
- [25] P. A. Sharma, J. S. Ahn, N. Hur, S. Park, Sung Baek Kim, Seongsu Lee, J.-G. Park, S. Guha, and S.-W. Cheong, Phys. Rev. Lett. **93**, 177202 (2004).
- [26] T. Katsufuji, S. Mori, M. Masaki, Y. Moritomo, N. Yamamoto, and H. Takagi, Phys. Rev.

B **64**, 104419 (2001).

[27] K.-J. Jang, Jongseok Lim, Jaewook Ahn, Ji-Hee Kim, Ki-Ju Yee, Jai Seok Ahn, and Sang-Wook Cheong, *New J. Phys.* **12**, 023017 (2010).



Chapter 5

Summary

The hexagonal rare-earth manganites $ReMnO_3$ ($Re = Sc, Y, Ho-Lu$) exhibit a ferroelectric (FE) order at high Curie temperature (T_C) between 590 and 1000 K and a long-range antiferromagnetic (AFM) order of manganese spins at low Néel temperature (T_N) < 100 K (for h -HoMnO₃, $T_N = 76$ K, is determined by the strong in-plane AFM superexchange interaction which leads the noncollinear spin arrangement). In low temperature range, the interplay and coexistence for different types of long-range orders, such as ferroelectric, (anti)ferromagnetic, and (anti)ferroelastic, have attracted a lot of researchers because of their fundamental physics and their potential for applications. The extraordinary strong magnetic correlation between neighbor Mn^{3+} ions in the geometrical frustration h - $ReMnO_3$ systems leads the appearance of AFM ordering at such low temperature and seems to dominate or exhibit the rich physical phenomena. For instance, the ferroelectric-magnetic order coupling, the strong spin-lattice coupling via giant magnetoelastic effect, and the spin-charge coupling effect have been discovered by various novel works. Therefore, the intricate physical properties of multiferroic manganites seem interrelated through the strong correlation between charge, lattice, orbital, and spin degrees of freedom in these systems. The optical spectroscopy is an excellent tool in identifying the electronic structure over a wide

energy range, which provides indispensable information to improve our understanding of the microscopic mechanism of multiple coupling in multiferroic materials. In this point of view, the ultrafast optical spectroscopy can provide insight into the essential microscopic dynamics and, in particular, the coupling between multiple degrees of freedom which determine the underlying functional response of complex materials.

We used femtosecond pump-probe method to explore and construct the dynamical information after ultrashort laser pulse excitation. We observed the occurrence of magnetoelastic coupling effect at T_N through the nonthermal processes and thermal relaxation processes. The appearance of AFM order of Mn^{3+} ions at T_N induces very large displacement of atoms which causes the extra-large blueshift of Mn^{3+} $3d$ bands. Thus, we can observe the AFM order by the nonthermal processes and the abnormal thermal stress on a - b plane and along c -axis which were, respectively, related to the negative component and oscillation component in $\Delta R/R$ signals. The investigation of their dynamical properties and elementary excitations are very important, because one can understand the interactions between different degrees of freedom in different time scales through the carrier excitation (disturb the electric system). The time-resolved optical reflectivity changes at photon energy about 1.6 eV is therefore directly related to the dynamics of charge carriers (d - d transition) which are the most relevant for the physics of multiferroic manganites. According to our studies with wavelength-tunable time-resolved femtosecond spectroscopy, the typical temperature-dependent $\Delta R/R$ for h - $HoMnO_3$ crystals show three primary features immediately identified in the signal curves, i.e. the initial rising (excitation) component, the relaxation component, and the oscillating component. For the first (carrier excitation) component, we found that the emergence of long-range and short-range magnetic ordering are unambiguously revealed in association with an abnormal blue-shift of Mn^{3+} $3d$ level around

the Néel temperature and the slope change of the temperature-dependent amplitude of $\Delta R/R$ near transition, respectively. These interesting phenomena are the evidences for the spin-charge coupling. For the second (relaxation) component, we found that the relaxation processes also associates with the magnetic ordering. The apparent negative $\Delta R/R$ has been explained by the magnetic demagnetization process via the disturbance of magnetic ordering. The maximum demagnetization effect also appears at the Néel temperature. For the third (oscillating) component, finally, we found that the pulses induces the lattice strain effect, so-called coherent acoustic phonon, and causes the modification of the $\Delta R/R$ curves. Consequently, the oscillation period exhibits anomalies at the Néel transition temperature. These results are the signature of the coupling between lattice and spin via magnetoelastic effect.



Biographical Notes

Personal Data :

Name : 石訓全 (Hsun-Chuan Shih)

Sex : Male

Date of birth : October 06, 1981

E-mail : hcshih.ep93g@nctu.edu.tw

Education :

September 2000 ~ June 2004 National Chia Yi University, Chiayi, Taiwan

Bachelor's degree, Applied physics

September 2004 ~ June 2006 National Chiao Tung University, Hsinchu, Taiwan

Master's degree, Electrophysics

September 2006 ~ June 2010 National Chiao Tung University, Hsinchu, Taiwan

PH. D., Electrophysics

Publication List :

[Refereed Journals]

- [1] H. C. Shih, L. Y. Chen, C. W. Luo, K. H. Wu, J.-Y. Lin, J. Y. Juang, T. M. Uen, J. M. Lee, J. M. Chen, and T. Kobayashi, "Simultaneous revelation of magnetic-electric-elastic coupling in hexagonal HoMnO₃ by ultrafast thermoelastic dynamics" Submitted (2010).

- [2] L. Y. Chen, J. C. Yang, **H. C. Shih**, C. W. Liang, T.-Y. Wu, S. K. Chou, C. W. Luo, K. H. Wu, Y. H. Chu, and T. Kobayashi, "Ultrafast dynamics of BiFeO₃ thin films studied by dual-color femtosecond spectroscopy," J. Supercond. Nov. Magn. **in press** (2010).
- [3] J. W. Chou, K. C. Lin, Y. T. Tang, F. K. Hsueh, Y. J. Lee, C. W. Luo, Y. N. Chen, C. T. Yuan, **H. C. Shih**, W. C. Fan, M. C. Lin, W. C. Chou and D. S. Chuu, "Fluorescence signals of quantum dots influenced by spatially controlled array structures," Nanotechnology **20**, 415201 (2009).
- [4] **H. C. Shih**, T. H. Lin, C. W. Luo, K. H. Wu, J.-Y. Lin, J. Y. Juang, T. M. Uen, J. M. Lee, J. M. Chen, and T. Kobayashi, "Magnetization dynamics and the Mn³⁺ *d-d* excitation of hexagonal HoMnO₃ single crystals using wavelength-tunable time-resolved femtosecond spectroscopy," Phys. Rev. B **80**, 024427 (2009).
- * selected in Virtual Journal of Ultrafast Science, volume 8, Issue 8, August (2009)
- [5] C. W. Luo, Y. T. Wang, F. W. Chen, **H. C. Shih**, and T. Kobayashi, "Eliminate Coherence spike in reflection-type pump-probe Measurements," Opt. Express **17**, 11321 (2009).
- * selected in Virtual Journal of Ultrafast Science, volume 8, Issue 8, August (2009)
- [6] J. W. Chou, K. C. Lin, Y. J. Lee, C. T. Yuan, F. K. Hsueh, **H. C. Shih**, W. C. Fan, C. W. Luo, M. C. Lin, W. C. Chou and D. S. Chuu, "Observation of localized surface plasmons in spatially controlled array structures," Nanotechnology **20**, 305202 (2009).
- [7] K. H. Wu, T. Y. Hsu, **H. C. Shih**, Y. J. Chen, C. W. Luo, T. M. Uen, J.-Y. Lin, J. Y. Juang, and T. Kobayashi, "Ultrafast optical probes of polaron dynamics in La_{0.7}Ca_{0.3}MnO₃ thin films," J. Appl. Phys. **105**, 043901 (2009).
- [8] T. H. Lin, **H. C. Shih**, C. C. Hsieh, C. W. Luo, J.-Y. Lin, J. L. Her, H. D. Yang, C.-H. Hsu, K. H. Wu, T. M. Uen, and J. Y. Juang, "Strain-induced effects on antiferromagnetic ordering and magnetocapacitance in orthorhombic HoMnO₃ thin films," J. Phys.: Condens.

Matter **21**, 026013 (2009).

- [9] C. C. Hsieh, T. H. Lin, **H. C. Shih**, C.-H. Hsu, C. W. Luo, J.-Y. Lin, K. H. Wu, T. M. Uen, and J. Y. Juang, “Magnetic ordering anisotropy in epitaxial orthorhombic multiferroic YMnO₃ films,” J. Appl. Phys. **104**, 103912 (2008).
- [10] C. W. Luo, C. C. Lee, C. H. Li, **H. C. Shih**, Y.-J. Chen, C. C. Hsieh, C. H. Su, W. Y. Tzeng, K. H. Wu, J. Y. Juang, T. M. Uen, S. P. Chen, J.-Y. Lin, and T. Kobayashi, “Ordered YBCO sub-micron array structures induced by pulsed femtosecond laser irradiation,” Opt. Express **16**, 20610-20616 (2008).
- [11] T. H. Lin, C. C. Hsieh, **H. C. Shih**, C. W. Luo, T. M. Uen, K. H. Wu, J. Y. Juang, J.-Y. Lin, C.-H. Hsu, and S. J. Liu, “Anomalous magnetic ordering in *b*-axis-oriented orthorhombic HoMnO₃ thin films,” Appl. Phys. Lett. **92**, 132503 (2008).

[Conference Papers]

- [1] C. W. Luo, **H. C. Shih**, K. H. Wu, J.-Y. Lin, J. Y. Juang, T. M. Uen, T. Kobayashi, J. M. Lee, and J. M. Chen, “Coherent acoustic phonons in hexagonal HoMnO₃ probe by femtosecond spectroscopy,” J. Phys.: Conf. Ser. **200**, 012107 (2010).
- [2] **H. C. Shih**, T. H. Lin, C. C. Hsieh, J. M. Lee, C. W. Luo, J.-Y. Lin, T. M. Uen, J. Y. Juang, K. H. Wu and J. M. Chen, “Ultrafast dynamics of the Mn *d-d* transition on hexagonal HoMnO₃,” J. Phys.: Conf. Ser. **150**, 042180 (2009).
- [3] T. H. Lin, C. C. Hsieh, **H. C. Shih**, C. W. Luo, T. M. Uen, K. H. Wu, J.-Y. Lin, C.-H. Hsu and J. Y. Juang, “Effects of compressive epitaxial strain in the *b*-axis on the magnetization response of orthorhombic HoMnO₃ thin films,” J. Phys.: Conf. Ser. **150**, 042114 (2009).

- [4] C. C. Hsieh, T. H. Lin, **H. C. Shih**, J.-Y. Lin, C.-H. Hsu, C. W. Luo, K. H. Wu, T. M. Uen and J. Y. Juang, “Electronic structure and magnetic anisotropies in orthorhombic multiferroic YMnO_3 thin films,” J. Phys.: Conf. Ser. **150**, 042062 (2009).

